Scuola Dottorale di Ingegneria

Sezione di Ingegneria dell'Elettronica Biomedica,

dell'Elettromagnetismo e delle Telecomunicazioni

XXV CICLO DEL CORSO DI DOTTORATO

Metamaterials and plasmonics for novel components

at microwave and optical frequencies

(Metamateriali e materiali plasmonici per la progettazione

di componenti innovativi a microonde e frequenze ottiche)

Dottorando: Ing. Davide Ramaccia

Docente-Guida: Prof. Alessandro Toscano

To the most exciting, fast growing,
and fully challenging area.
METAMATERIALS.

Acknowledgements

This research project was carried out at the Department of Applied Electronics (DEA), "RomaTre" University, Rome, Italy, from January 2010 to December 2012.

Firstly, I owe my sincere gratitude to my supervisor Professor Alessandro Toscano, Head of the Electromagnetic Diagnostic Laboratory, for his support and guide during my research in metamaterial field. Moreover, I express my special appreciation to him for giving me autonomy and responsibilities.

I wish to express my warmest thanks to Professor Filiberto Bilotti for valuable ideas and introduction to scientific work. His enthusiasm and trust in me sustained my research project through difficulties. He deserves all my heartfelt gratitude and deepest thanks for his formative and congenial support in posing and solving advanced electromagnetic problems, and the fortunate liberty to collaborate with many people and institutions.

I cordially express my thankfulness to Professor Giorgio Guattari, Head of Department of Applied Electronics, for the excellent conditions, and pleasant working environment at the Department.

Also, I render thanks to Dr. Alessio Monti and Dr. Mirko Barbuto, research mates at the Applied Electromagnetic Laboratory, for the wonderful days spent in the laboratory between pure research work and enjoyments.

Finally, I want to reserve a special word of gratitude to my parents, girlfriend Roberta and friends for their love, enthusiastic encouragements, and a huge variety of other reasons.

Contents

Esteso Sommario

(Italiano)

Introduzione

Negli ultimi cento anni, l'elettromagnetismo è stata ampiamente impiegato per comprendere a fondo l'interazione con la materia a qualsiasi scala, dalla cosmologica fino ai fenomeni su scala atomica. La teoria elettromagnetica classica è anche alla base di molte applicazioni pratiche che influenzano fortemente la vita di tutti i giorni. Sembra quindi molto difficile aggiungere qualcosa di concettualmente nuovo a tali teorie e tecnologie ben consolidate. Tuttavia, circa dieci anni fa, un nuovo concetto apparso nell'universo della teoria elettromagnetica classica: metamateriale.

Che cosa è un "metamateriale"? Si tratta di un materiale artificiale opportunamente ingegnerizzato la cui risposta elettromagnetica non è facilmente reperibile in natura. Per esempio, i metamateriali possono presentare valori negativi della permettività elettrica della permeabilità magnetica, o entrambi, in un certo intervallo di frequenza delle microonde. La risposta non convenzionale di questi metamateriali è ottenuta attraverso inclusioni metalliche elettricamente piccole o disomogeneità dielettriche in un mezzo dielettrico ospite. Le proprietà esotiche di metamateriali possono essere previste utilizzando approcci quasi-statici e considerando l'interazione tra le diverse inclusioni disposte in un reticolo tridimensionale. Anche se l'interazione tra onde elettromagnetiche e la materia è un tema di ricerca della Fisica, le relative applicazioni sono ampiamente studiati nell' Ingegneria Elettrica ed Elettronica. Pertanto, i metamateriali hanno contribuito a colmare il divario tra queste due comunità e ora i fisici e gli ingegneri lavorano insieme su questo tema. L'attuale interesse dei metamateriali è dovuto alla loro capacità di presentare le proprietà elettromagnetiche inedite utili in diversi campi applicativi. Utilizzando i metamateriali, infatti, è possibile modificare quasi a volontà le proprietà delle onde elettromagnetiche.

Aumentando la frequenza del campo elettromagnetico, alcune delle proprietà insolite appena citate sono già date dalla natura, anche se è sempre possibile ingegnerizzarle attraverso appropriate tecnologie di fabbricazione su scala nanometrica. Ad esempio, a

frequenze ottiche, la natura ci dà i materiali plasmonici. I materiali plasmonici sono semplicemente metalli nobili, come oro o argento, che alle frequenze ottiche consentono la propagazione delle onde superficiali estremamente confinate all'interfaccia metallo-dielettrico. La propagazione è data dalla oscillazione collettiva degli elettroni all'interno del metallo che sono eccitati dal campo esterno. Per spiegare tale comportamento anomalo, i metalli sono descritti come materiali dielettrici ed è stato dimostrato che tale propagazione avviene solo se la permittività efficace, o permittività ottica, del metallo è negativa, proprio come i metamateriali alle microonde.

In questo scenario, è evidente che metamateriali e materiali plasmonici possono aprire molte sfide di interesse per i fisici e gli scienziati in generale. Dal punto di vista tecnologico, l'interesse per tali materiali si basa sulla possibilità di progettare dispositivi e sistemi con nuove proprietà o funzionalità, in grado di aprire nuovi campi di applicazione o per migliorare le prestazioni di quelli già esistenti.

In questa tesi, vorrei raccogliere i risultati della mia ricerca per l'impiego di metamateriali e materiali plasmonici per la progettazione di nuovi componenti a microonde e frequenze ottiche. Nel capitolo 1 sono riportati i modelli analitici per l'analisi di metasurfici con inclusioni elettricamente piccole. Queste sono stati utilizzate per realizzare superfici parzialmente riflettenti (PRS) e superfici ad alta impedenza (HIS) per applicazioni in polarizzazione circolare. Capitolo 2 è focalizzato sulla progettazione di un elemento filtrante basato su metamateriale impiegato per la realizzazione di nuovi e compatti componenti a microonde per la guida e la radiazione di campo elettromagnetico. Capitolo 3 è dedicato ai metamateriali ENZ (epsilon-near-zero) e le loro applicazioni in antenne a tromba. Infine, il capitolo 4 è dedicato ai materiali plasmonici che sono stati impiegati per la progettazione di un guida d'onda e una antenna a tromba che lavorano a frequenze ottiche.

In tutti i capitoli, ho riportato lo stato dell'arte sul tema particolare del capitolo e incluso una combinazione di risultati teorici, numerici e sperimentali per la comprensione del comportamento dei metamateriali nella particolare applicazione considerata.

1   Metasuperfici con inclusioni elettricamente piccole

In questo capitolo, è presenta l'analisi e la progettazione di un metasurface costituita da una serie di inclusioni circolari allineate lungo le due direzioni principali del piano della superficie con periodicità inferiore alla lunghezza d'onda. Il modello proposto è stato applicato ad una parete metallica su cui sono stati effettuati dei fori circolari e anche a una serie di patch circolari stampati su un substrato dielettrico elettricamente sottile elettricamente. La prima configurazione realizzare una superficie parzialmente riflettente che induce un onda leaky ed un effetto di beam-forming quando è posta di fronte a una antenna ad apertura, o una antenna a patch, o a un qualsiasi radiatore standard. Il guadagno e larghezza di banda dipendono dalla riflessione (ampiezza e fase) del superficie nonché la distanza dal radiatore stesso. Al contrario, la seconda configurazione è nota come superficie ad alta impedenza ed è posta indietro al radiatore. Poiché le dimensioni sono di molto inferiori alla lunghezza d'onda, l'array di patch e il substrato possono essere descritti in termini di una capacità e una induttanza concentrata, rispettivamente. Intorno alla frequenza di risonanza, la superficie riflette totalmente un'onda elettromagnetica incidente con uno sfasamento nullo. Grazie a questa proprietà, è ampiamente impiegata in sistemi di antenna come riflettore posteriore compatto con migliori prestazioni rispetto al riflettore tipico metallo.

2   Elemento filtrante basato su metamateriale

In questo capitolo, è riportato il modello analitico della particella bi-omega composta da due risonatori ad omega orientati in verso opposto ed opportunamente distanziati. Posizionando le due particelle ad omega molto vicine, l'effetto di accoppiamento tra di loro contribuisce a spostare verso il basso la frequenza di risonanza, ottenendo un risonatore semplice ed elettricamente piccolo che lavora nella gamma delle microonde. Il modello proposto, basato sulla teoria delle antenna piccole, tiene conto di tutti gli effetti di accoppiamento che entrano in gioco quando la distanza tra le due omega è molto piccola. Poi, due particelle bi-omega sono collegate tra loro, al fine di ottenere un trasferimento di energia da un bi-omega, usata come antenna ricevente, e l'altra, l'antenna trasmittente, quando è collocata in una fenditura in uno schermo metallico.

Grazie al suo comportamento risonante, la struttura proposta può essere usato con successo come filtro passa-banda in grado di selezionare la frequenza di interesse con elevata precisione, che è fortemente richiesto in molte applicazioni di guida d'onda e antenne apertura. Tra questi, è presentata la progettazione e la realizzazione sperimentale di componenti a microonde innovative, come ad esempio i filtri in guida d'onda, diplexer, power-splitter, filtri modali, antenne a tromba, ecc I componenti proposti sono verificati attraverso adeguate simulazioni numeriche full-wave e risultati sperimentali.

3 Metamateriali ENZ per antenne ad apertura innovative

In questo capitolo, sono presenti due nuovi layout di lente piatte, costituite da materiale convenzionale e da un metamateriale ENZ (epsilon-near-zero) o da un metamateriale ENZ caricato con induttori. Entrambe le configurazioni sono utilizzate come plug sulle aperture di antenne a tromba, al fine di ottenere nuove prestazioni in radiazione .

In primo luogo, è presentata una lente in metamateriale per antenne ad apertura accorciate che permette di raggiungere su un'ampia gamma di frequenze prestazioni radianti simili a quelle delle antenne corrispondenti con lunghezza ottimale. In funzionamento è basato sul concetto di compensazione di fase: la fase del fronte di campo propagante all'interno della antenna a tromba si propaga con differenti velocità di fase nei due materiali della lente, presentandosi poi con una fase uniforme all'uscita della lente stessa. Inoltre è presentata una versione realistica della lente, realizzata con un allineamento di fili metallici che esibiscono una permittività effettiva vicino allo zero nella gamma di frequenze di interesse. Considerando due esempi in banda C, si dimostra che la lente può essere progettata per antenne a tromba sia coniche che piramidali. In entrambi i casi, la lunghezza delle horn è metà delle corrispondenti versioni ottime, mentre le prestazioni di radiazione ottenute sono simili a quelle delle horn ottime su una banda di frequenza molto ampia.

Successivamente, sono riportati i risultati numerici di una antenna a tromba con diagramma di radiazione orientabile. La rotazione del massimo del diagramma di

radiazione è ottenuta modificando localmente l'indice di rifrazione della lente ENZ al fine di modificare localmente la lunghezza elettrica della lente stessa.

4   Guida d'onda e antenna ad apertura a frequenze ottiche

In questo capitolo, sono stati discussi il design e le prestazioni di una guida d'onda ottica e di una antenna a tromba che lavorano alle frequenze vicine all'infrarosso. Per prima cosa, è stata progettata la guida d'onda a scala nanometrica, che dovrebbe soddisfare alcuni requisiti importanti per essere una buona guida d'onda: da un lato, dove guidare efficacemente la luce e, dall'altro, dove presentare una topologia che è simile alla sua controparte alle frequenze delle microonde. Quindi ci si è basati su una linea di trasmissione simmetrica costituito da una lastra di materiale non plasmonico tra due strati plasmonici. Tale struttura supporta un modo fondamentale che si propaga tyra i due strati metallici e presenta una forte componente di campo elettrico ortogonale ad essi.

Successivamente, si considera il problema della radiazione efficace del campo elettromagnetico guidato. Di recente il concetto di antenna è stato trasferito dalle microonde all'ottica, per via delle possibili applicazioni nella raccolta di energia, nell' illuminazione intelligente, e nei collegamenti ottici per la comunicazione senza fili. Inoltre, i recenti progressi nella nano-tecnologia rendono la possibile realizzazione di tali dispositivi. Quindi, è riportato il progetto di una nano-antenna ottica ottenuta sagomando ad una delle estremità della guida d'onda ottica in modo tale da aumentare l'apertura fisica e progressivamente adattare l'impedenza d'onda all'impedenza dello spazio libero.

This page is intentionally left blank.

Introduction

In the last century, electromagnetic theory has been widely employed to deeply understand the interaction with matter at any scale, from cosmological down to atomic scale related phenomena. Classic electromagnetic theory is also the base of many practical applications which strongly influence everyday life.

It seems very difficult, thus, to add something conceptually new to such well-established theories and technologies. However, around ten years ago, a new concept appeared in the universe of classical electromagnetic theory: *metamaterials*.

What is a "metamaterial"? It is an artificially engineered material whose electromagnetic response is not readily available in nature. For instance, metamaterials can exhibit negative values of the electric permittivity of the magnetic permeability or both in a certain *microwave* frequency range. The unconventional response of these metamaterials is obtained through electrically small metallic inclusions or dielectric inhomogeneities within a dielectric host medium. The exotic properties of metamaterials can be predicted by using quasi-static approaches and considering the interaction among the different inclusions arranged in a 3D lattice. Although the interaction between electromagnetic waves and matter is a hot research topic in Physics, the related applications are widely studied in Electrical and Electronic Engineering. Therefore, metamaterials helped to bridge the gap between these two communities and now physicists and engineers work together on these topics. The current interest in metamaterials is driven by their potential to obtain unprecedented electromagnetic properties useful in several application fields. By using metamaterials, in fact, it is possible to tailor the wave properties almost at will.

Increasing the frequency of the electromagnetic field, some unusual properties are already given by nature, though it is always possible to engineer them through proper nano-scale fabrication technologies. For example, at optical frequencies, nature gives us the *plasmonic materials*. The plasmonic materials are simply noble metals, such as gold or silver, that at *optical frequencies* allow the propagation of surface waves extremely confined at the metal-dielectric interface. The propagation is given by the collective oscillation of the electrons inside the metal that are excited by the external impinging

field. In order to explain such anomalous behavior, metals are described as dielectric materials and it has been shown that such propagation takes place only if the effective permittivity, or optical permittivity, of metal is negative, just as the metamaterials at the microwaves.

With this scenario, it is evident that metamaterials and plasmonic materials may open many challenges of interest to physicists and scientists in general. From the technological and engineering viewpoint, the interest in such materials is based on the possibility of designing devices and systems with new properties or functionalities, able to open up new fields of application or to improve existing ones

In this dissertation, I would like to collect the results of my research on the employment of metamaterials and plasmonic materials for the design of novel components at microwave and optical frequencies. Chapter 1 develops the analytical models for the analysis of metasurfaces with electrically small inclusions. They have been used to realize Partially Reflective Surfaces (PRS) and High-Impedance Surfaces (HIS) for circular polarization applications in antenna field. Chapter 2 is focused on the design of a metamaterial-based filter element employed for the realization of novel compact guiding and radiating microwave components. Chapter 3 is devoted to the epsilon-near zero (ENZ) metamaterials and their applications in horn antennas. Finally, Chapter 4 is devoted to plasmonic materials exploited to design a nano-waveguide, acting as its microwave counterpart, and an innovative horn nano-antenna working at near-infrared and optical frequencies.

In all chapters, I have reported the state-of-the-art on the particular topic of the chapter and included a combination of theoretical, numerical, and experimental results to the understanding of the behavior of metamaterials in the particular considered application.

1 Metasurfaces with electrically small circular inclusions

In this chapter, I present the analysis and design of a metasurface consisting of an array of circular inclusions with a sub-wavelength periodicity. The proposed study is suitable for circular holes in a metal conducting sheet, as well as metallic circular patches printed on a electrically thin metal-backed dielectric substrate. The first configuration realize a Partially Reflective Surface (PRS) that introduces a leaky wave and beam-forming effect when placed in front of a grounded waveguide aperture, patch antenna, or any standard radiator. The gain and bandwidth depend on the reflection (amplitude and phase) from the PRS as well as the distance from the radiator itself. On the contrary, the second configuration is known as High-Impedance Surface (HIS) and it is placed back to the radiator. Since the sub-wavelength dimensions, the array and the metal-backed substrate can be described in terms of a lumped capacitance and a lumped inductance, respectively. Around the resonant frequency, the HIS reflects totally an incident electromagnetic wave with zero shift in phase. Due to this property, it is widely employed in antenna systems as compact back reflector with improved performances with respect to typical metal reflector.

In order to validate the analytical results, I compare the analytical results to the ones resulting from full-wave numerical simulations and from other analytical methods available in the open technical literature.

1.1 Introduction

In the past two decades, the development of wireless communication systems has been possible thanks to significant progress in the fields of electronics and applied electromagnetics. Device miniaturization, superior performances with respect to the state-of-the-art solutions, and low production costs represent the main challenges driving current academic and industry efforts. For what concerns the radiating segment of wireless systems, miniaturization and low-cost solutions are commonly achieved exploiting microstrip printed technology. In order to enhance the performances and reduce the size of the radiating systems, antennas can be properly loaded by artificial materials or surfaces [1]-[5], among which include the so-called metamaterials and metasurfaces [6]-[14]. These engineered materials and surfaces exhibit electromagnetic properties that cannot be found in nature. The recent developments in the field of metamaterials and metasurfaces have led to innovative designs of radiating and transmitting components [4]-[10].

In this chapter, the analytical study of two metasurfaces, i.e. a partially reflected surface and an high impedance surface, with electrically small circular inclusions will be presented.

1.2 Partially reflective surface

In this section, I present a study on a metasurface consisting of a planar array of sub-wavelength circular apertures drilled in a perfect conducting metallic sheet. Possible applications of such structures include artificial dielectrics, antenna radomes, frequency selective surfaces, etc. Particularly, their use is highly desired in antenna applications, allowing to: a) enhance the directivity of the radiators, increasing their effective radiating area; b) reduce the back-radiation and the wind resistance when used as reflectors. Interesting examples of applications to enhance the antenna directivity are reported in [13]-[15].

Being the dimensions of the array elements much smaller compared to the operating wavelength, an effective boundary condition can be used to describe the electromagnetic behavior of the metasurface. By defining an average value of the tangential electric field and of the surface current density on the array plane, in fact, it is possible to introduce an effective grid impedance Z_g describing the electrical properties of the structure [16]-[20].

In the open technical literature the analysis of metasurface composed by two sets of crossed metallic strips has been already presented. When this surface is excited by an electromagnetic plane-wave, the surface current density is uniform along the strips parallel to the electric field vector. On the contrary, when circular holes are considered, the current distribution on the metallic region between two adjacent circular apertures varies according to the local width of the metal. Since the operating wavelength is assumed much larger than the periodicity, a quasi-static approach can be used to describe the electromagnetic behavior of the structure and the current density distribution should depend only on the geometrical parameters of the metallic regions. Considering a square lattice for the aperture arrangement, the structure can be seen as a grid of metal strips with non-constant width where the surface current flows.

Using this approach, the analytical formulas already developed for the grid impedance of a grid of metallic strips with constant width [21] can be properly modified in order to accurately describe the behavior of the considered structure. The new proposed model is verified comparing the obtained reflection coefficient to the one resulting from full-wave numerical simulations based on the employment of CST Studio Suite [22]. According to [23], we have simulated just one unit-cell using proper boundary conditions. As a further reference, we consider also the results given by other accurate analytical models available in the open technical literature and based on the polarizability of the inclusions [16].

In the following, I briefly introduce the approach to the problem and present the analytical method used to evaluate the effective width of the equivalent grid of metal strips. Then, I compare the amplitude of the reflection coefficients for TE and TM polarizations obtained through our model, other models, and full-wave results. Finally, I

draw the conclusions and highlight, under the validity limitations, the advantages of our proposed approach.

1.2.1 Analysis and design of PRS

When a plane-wave impinges on a metallic surface, the tangential components of the electric and magnetic fields excite an uniform surface current density. The electric field reflected by the surface experiences a 180° phase-shift, due to the reaction of the surface. Under the same illumination conditions, the surface current density on a metasurface consisting of an array of sub-wavelength circular apertures is not uniform, but rather shows high values in the metallic regions with minimum width between two adjacent holes (Fig. 1a).
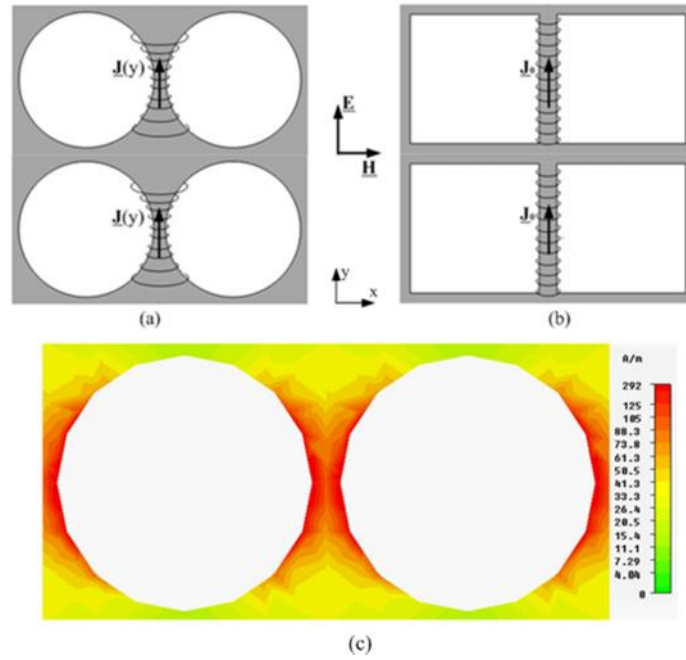
Fig. 1: Representation of the surface current and concatenated magnetic field for an array of (a) circular holes in a metallic sheet and (b) metallic strips; (c) Map of the magnitude of the surface current for $k_0 S = 0.5$ and $R = 0.45\,S$.

Investigating the distribution of the surface current density, we observe that its maximum value is in correspondence of the minimum width of the metallic region between two holes and it decreases moving away from this point (Fig. 1). Since the

operating wavelength is much larger than the periodicity of the structure, the unit-cell is assumed as excited by a quasi-static electromagnetic field. In this case, the current density distribution should depend only on the width of the metallic region in *x*-direction (see Fig. 1a). On the contrary, on metasurface consisting of squared apertures the surface current density is quite constant on the metallic strips between two adjacent squared holes (see Fig. 1b). Starting from this approach, we apply the integral mean value theorem over the metallic region between two circular holes, evaluating an effective width w_{eff} in order to model it as an equivalent array of sub-wavelength squared holes.

In Fig. 2, a zoom on the metallic region between two adjacent circular patches is shown. The integrating area A is vertically defined by the angle φ and horizontally delimited by the edges of the holes .
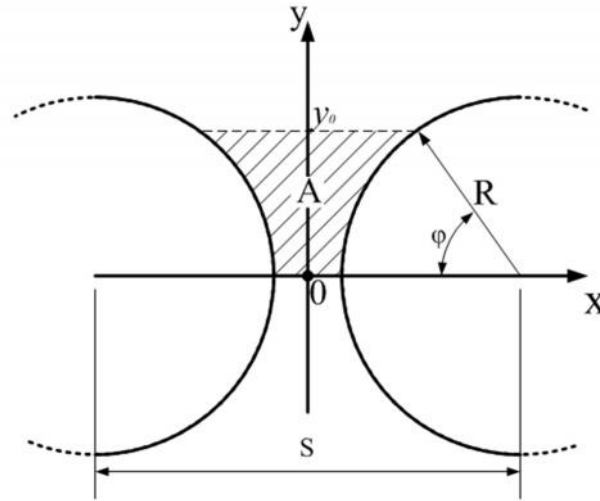
Fig. 2: Integrating region between two adjacent holes.

The area A can be expressed in terms of the periodicity S, the radius R of the holes, and the height y_0 as follows:

$$A = \frac{S}{2} y_0 - \frac{1}{2}\left[R^2 \tan^{-1}\left(\frac{y_0}{\sqrt{R^2 - y_0^2}} \right) + y_0 \sqrt{R^2 - y_0^2} \right] \qquad (1)$$

where $y_0 = R \sin\varphi$. Dividing the area A by y_0, an average value of the width of the metallic region between the two holes as a function of the angle ζ can be found as:

$$w_{eff}(\zeta) = S - R\left(\cos\zeta - \frac{\zeta}{\sin\zeta}\right) \qquad (2)$$

According to the polarization and to the angle of incidence of the incoming wave, the area of the metallic region involved in the flow of the current changes and consequently the effective width of the equivalent strips too. The height y_0, that is directly related to the angle ζ, defines the extension of the area A. In order to evaluate a constant value of the effective width w_{eff}, we define the values of the angle ζ for TE and TM polarization (Fig. 3).
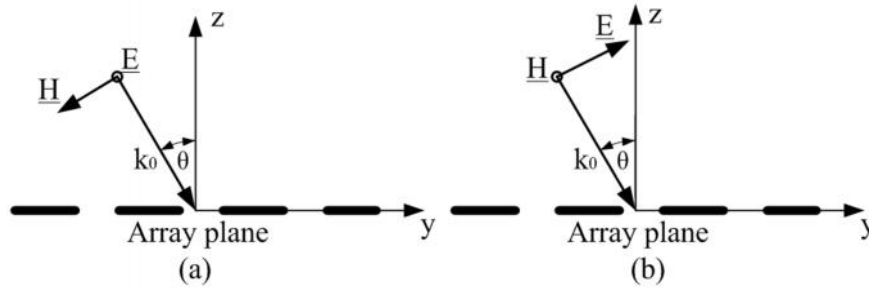
Fig. 3: Oblique incidence: (a) TE polarization; (b) TM polarization.

For TE polarization, the electric field is parallel to the array plane whatever the angle of incidence θ is, as shown in Fig. 3a. In this case, the metallic region involved in the flow of the current density is maximum and defined by the angle:

$$\zeta^{TE} = \frac{f}{2} \qquad (3)$$

For TM polarization, the tangential component of the incident electric field is $E_t = E_0 \cos\theta$ (Fig. 3b) and, consequently, the intensity of the surface current density

decreases with the angle of incidence. The metallic region A (Fig. 2), thus, should decrease as function of the incident angle $_"$, accordingly. In this case, the metallic region involved in the flow of the current varies with the angle of incidence and is defined by the angle:

$$\{^{TM} = \frac{f}{2}\cos^2 {}_"$$

(4)

where the quadratic dependence is justified by the fact that the angle $\{$ defines the coordinate y_0 that in the circumference equation appears in a quadratic form.

Inserting eqs. (3), (4) into (2), we obtain the constant effective width of an equivalent array of metallic strips for both polarizations. It now can be used in the readily available analytical formulas of the grid impedance of an array of metal strips [17]-[18], [21] and we obtain the grid impedance of an array of circular holes in a metal sheet:

$$Z_{g_{holes}}^{TE} = jZ_0\frac{k_0S}{2f}\ln\left[\sin^{-1}\left(\frac{f\, w_{eff}^{TE}}{2S}\right)\right]$$

(5)

$$Z_{g_{holes}}^{TM} = jZ_0\frac{k_0S}{2f}\ln\left[\sin^{-1}\left(\frac{f\, w_{eff}^{TM}}{2S}\right)\right]\left(1 - \frac{\sin^2 {}_"}{2}\right)$$

(6)

where Z_0 and $k_0 = \omega\sqrt{\varepsilon_0\mu_0}$ are the wave impedance and the wave vector in vacuum, respectively, and S is the periodicity of the array. The effective widths w_{eff}^{TE} and w_{eff}^{TM} are constant values evaluated using eq.(2) when the φ is φ^{TE} and φ^{TM} , respectively.

The validity of eqs. (5), (6) is guaranteed when the periodicity S of the structure is sub-wavelength and the effective width of the strips is much smaller than the periodicity [17]-[18], [21]. In order to keep the validity of the formulas after the introduced modifications, the dimensions of the holes should be comparable to the periodicity of the array.

1.2.2 Analytical and numerical results

The electromagnetic properties of the grid array can be expressed in terms of the transmission and reflection coefficients. If the metallic array is printed on a dielectric substrate, it is possible to define an effective permittivity of the surrounding host medium as described in [24]. Using a transmission line model, the shunt reactive impedance Z_g modeling the array is connected to two infinitely extended transmission lines of impedance Z_ℓ, as show in Fig. 4.
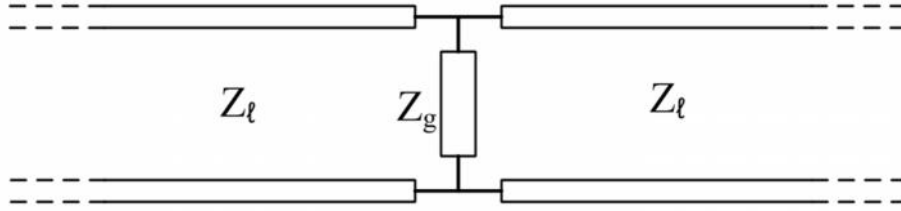

Fig. 4: Transmission–line model of a dense array in a uniform host medium.

If the host medium is the free-space, the characteristic impedance Z_ℓ of the transmission lines is $Z_0 = \sqrt{\sim_0/\nu_0}$. In case of oblique incidence, as show in Fig. 3, the free-space impedances are given by:

$$Z_0^{TE} = \frac{Z_0}{\cos{_{\shortparallel}}}$$
$$Z_0^{TM} = Z_0 \cos{_{\shortparallel}} \tag{7}$$

and the reflection coefficients are:

$$\Gamma^{TE} = -\frac{Z_0^{TE}}{Z_0^{TE} + 2Z_g^{TE}}; \qquad \Gamma^{TM} = -\frac{Z_0^{TM}}{Z_0^{TM} + 2Z_g^{TM}} \tag{8}$$

In Fig. 5, Fig. 6, and Fig. 7 the amplitude of the reflection coefficient versus the normalized period k_0S for different angles of incidence and both polarizations is shown. The radius R of the holes is set to $R = 0.45\,S$. The solid lines represent the amplitude of the reflection coefficient of the array of circular holes in a metallic sheet modeled using the proposed method based on the effective width of the metallic strips. The hollow circles represent the results obtained through the full–wave numerical simulator CST Studio Suite [21]. The two sets of results agree reasonably well in all the reported cases.

For a further validation, we compare our model to the one presented in [16] for a complementary structure, i.e. an array of disks, after a proper application of Babinet's principle (dot-line).
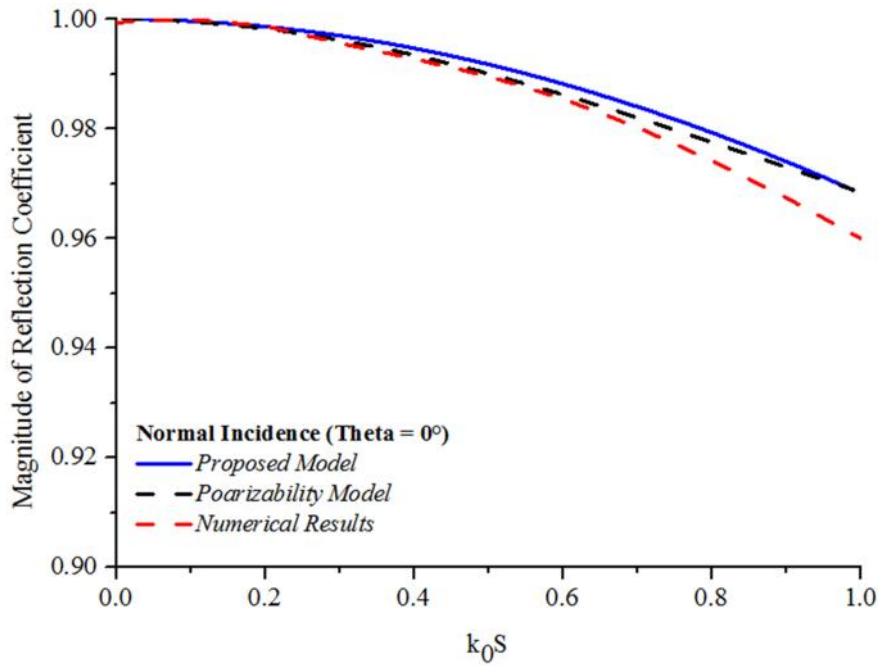
Fig. 5: Magnitude of reflection coefficient vs. normalized periodicity at normal incidence.
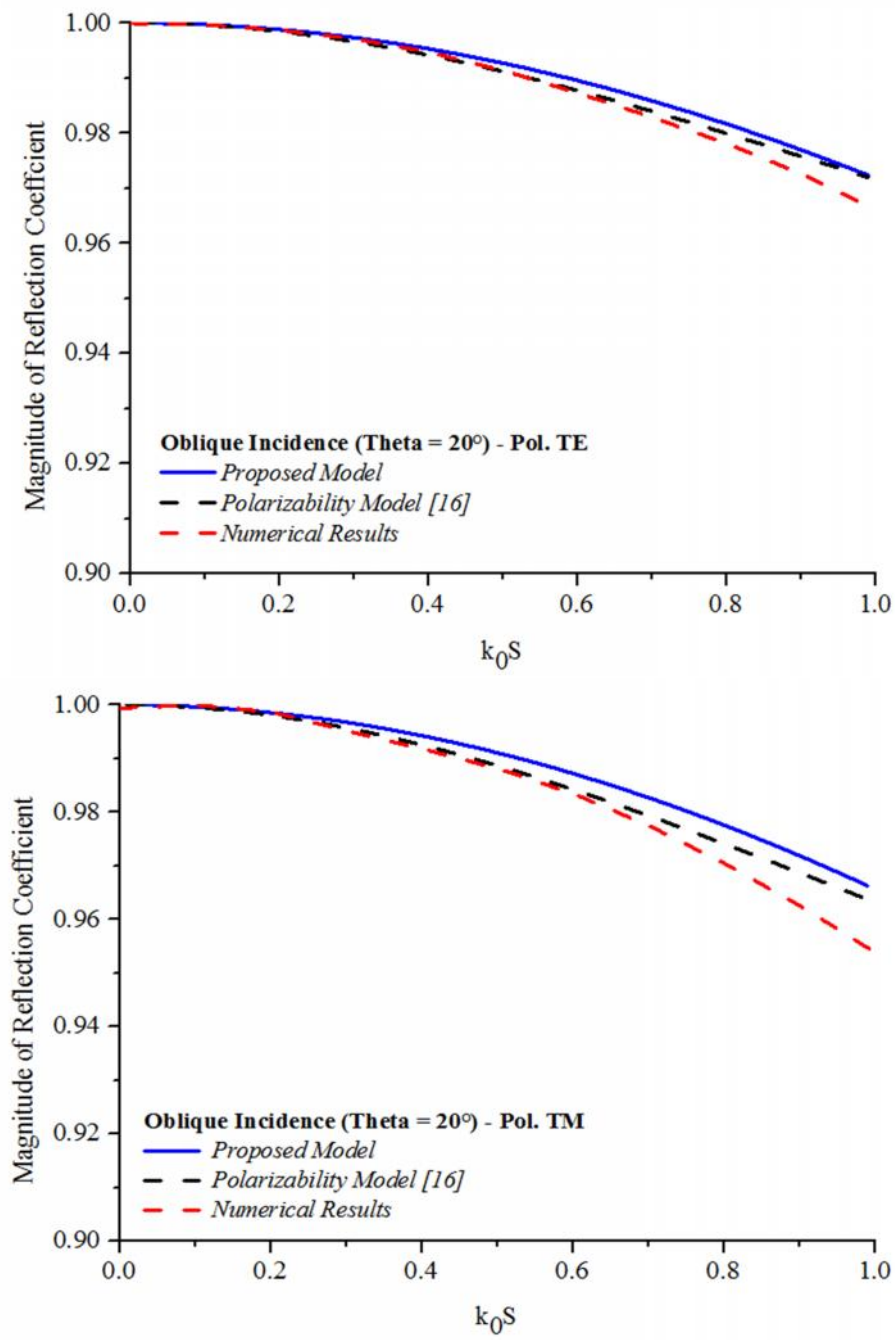
Fig. 6: Reflection coefficient vs. normalized periodicity at oblique incidence (= 20°) for both polarizations.
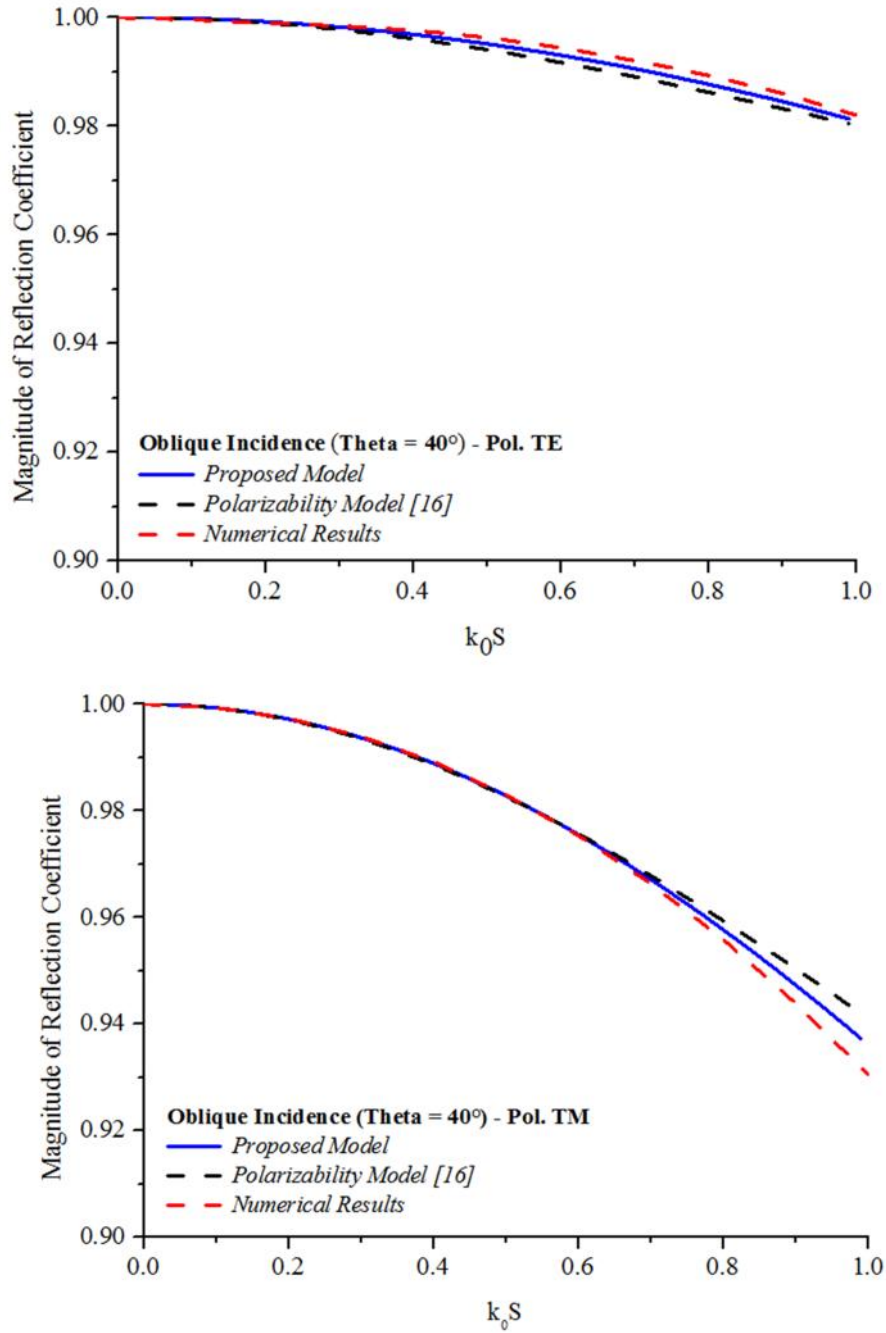
Fig. 7: Reflection coefficient vs. normalized periodicity at oblique incidence (= 40°) for both polarizations.

The agreement between the proposed model, based on the effective width, and the two references, i.e. the numerical simulations and the polarizability-based model, is rather good, showing the validity of the proposed approach.

1.2.3 Conclusions

In this section, a new analytical model for a partially reflective metasurface consisting of an array of circular holes in an ideally conducting sheet has been presented. Investigating the distribution of surface current density, we defined an effective width of the metallic region between two adjacent circular holes. The effective width has been inserted in the simple and compact formulas of the grid impedance of an array of metallic strips. After the reported successful comparison of the results obtained using this approach to the full-wave numerical simulations and other analytical results obtained using more involved and complex methods based on the derivation of the polarizability of the unit-cell, we can conclude that the new model we have developed can be straightforwardly employed for the accurate and fast design of metasurfaces, consisting of arrays of circular apertures in a metallic sheet. The proposed model has been shown to be robust for both polarizations and different angles of incidence.

Before concluding, we remark that the potential of the proposed model resides in the ability to be applied to more complex unit-cell shapes, such as ellipses, rounded bowties and rectangles with high axial ratio, etc. Using the same set of the equations for the grid impedance of regular metallic strips, in fact, the effective width can be straightforwardly evaluated for the different unit-cells, leading to an easy, fast, and accurate design of different metasurfaces. It is worth mentioning also that the methods based on the polarizability of the unit-cell particle, though accurate, need the evaluation of special functions, as reported for the circular case in [16], and, thus, are not readily applicable for a fast design, as our proposed method does.

.

1.3 High impedance surface

As previously mentioned in the introduction of the chapter, in order to enhance the performances and reduce the size of the radiating systems, antennas can be properly loaded by artificial materials or surfaces [1]-[3], [25], [26], among which include the so-called metamaterials and metasurfaces, exhibiting functionalizing properties [4], [6]-[9], [27]-[29]. For instance, in order to reduce the thickness of printed antennas and enhance the performances in terms of efficiency and gain, it is possible to use the concept of High-Impedance Surfaces (HISs) [30], capable of highly reduced propagation of surface waves trapped within the substrate. An HIS is a metasurface consisting of a planar array of metallic patches printed on a metal-backed dielectric substrate. Provided that the array periodicity is electrically small, as well as the dimension of the individual particle representing the array unit-cell, an HIS can be represented in terms of its homogenized surface impedance [30]. At and around its resonant frequency, an HIS approximately behaves as a perfect magnetic wall, leading to several interesting applications in the antenna field [30]-[34]. Shape and dimensions of the individual patch element represent the key parameters for the design of an HIS and the synthesis of its frequency response. Generally, patch elements are arranged in a dense array and exhibit squared [30], hexagonal [31], and rectangular [35] shapes.

In this paper, we refer to an HIS made of a grounded dielectric thin slab with a dense array of circular patches printed on top. Such a configuration is particularly appealing due to its 2D isotropic response on the array plane. The sub-wavelength periodicity of the array and thickness of the substrate, the structure can be studied in the quasi-static regime and consequently in terms of a lumped elements: the metallic patch array can be described as a capacitive reactance, the metal-backed substrate as a inductive one. The shape of the patch element affects the value of the capacitive reactance that need to be properly defined for the geometry under study, i.e. circular in this case. In the open technical literature, it is possible to find two different approaches in the open technical literature: the first considers the dense array as an frequency selective surfaces (FSSs) in long-wavelength regime [36], and the latter defines the electrically small individual patches in terms of an electric dipoles represented through its electric polarizability

[16], [17]. Both define a lumped impedance, that in the case of an array of perfect conducting metallic disks, is capacitive. The sub-wavelength-FSS-based model [36] is derived approximating the Floquet theory under the assumption that the periodicity is few tenths of the operating wavelength. On the contrary the polarizability–based model [16] assumes that the inclusions are so electrically small that they can be described in terms of an electric dipoles, losing the information about the geometry of the inclusion itself.

The aim, thus, is to propose a new model for the grid impedance of a planar array of circular disks that fills the gap between the two models used to evaluate the frequency behavior of an HIS. Starting from a detailed study of the near-field distribution of the electric field around the circular patches, we modify the analytical formulas already developed for the grid impedance of a squared-patch-based HIS [21], [37] in order to accurately describe the behavior of a circular-patch-based one. The new proposed model is validated considering its ability to reproduce the full-wave numerical results obtained through the commercial electromagnetic simulator CST Studio Suite [22]. As further comparison, we report the results of the frequency response estimated by the other models [16], [36].

In the following, I briefly review the model of an HIS and discuss the grid impedance of a circular-patch-based HIS, presenting the related analytical formulas. Then, I show the comparison between the resonant frequencies estimated using the proposed analytical model, the full-wave numerical simulator [22], the sub-wavelength-FSS-based model and the polarizability–based model.

1.3.1 Analysis and design of HIS

An HIS consisting of a regular array of circular patches is shown in Fig. 8. The surface is infinite in the *x-y* plane and the dielectric material considered is non-magnetic, i.e. its permeability is taken to be the free-space permeability μ_0. The thickness and the relative electric permittivity of the dielectric slab are h and ε_r, respectively. The period of the array is D in both directions. The metallic components

are assumed to have a negligible thickness. The radius of the patches is *R*, and *g* is the gap between two adjacent patches.
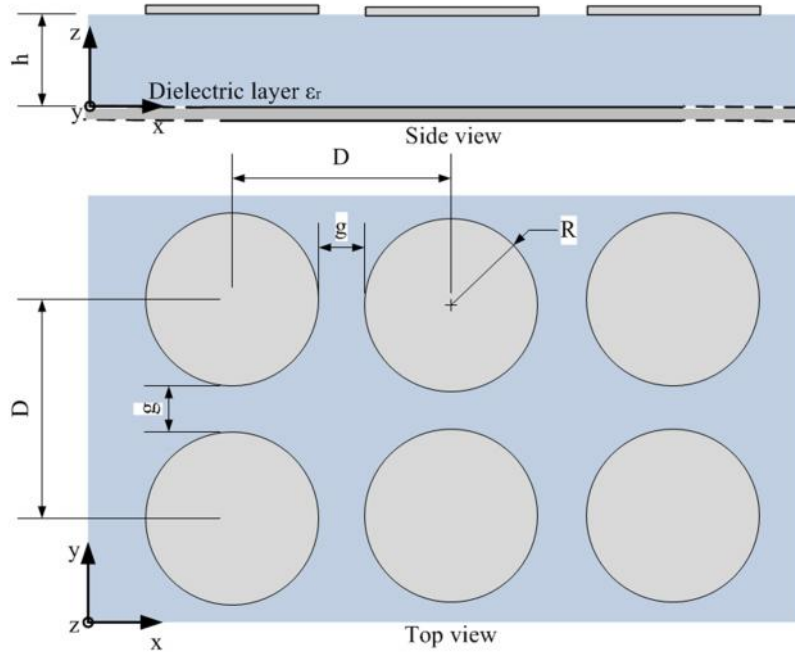
Fig. 8: Side and top views of an HIS made by a regular array of circular patches.

As well known, the frequency behavior of an HIS can be easily studied using the transmission line model shown in Fig. 9.
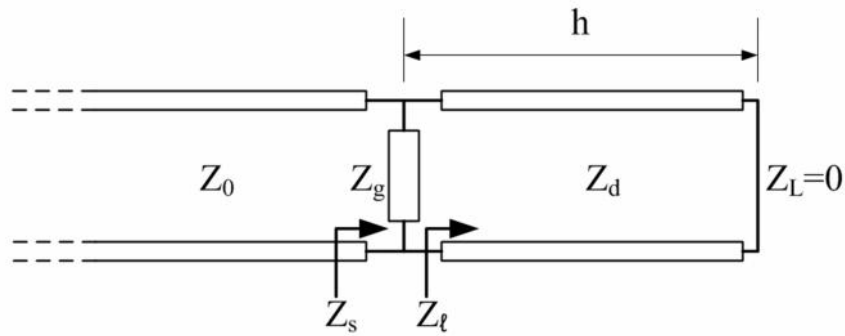

Fig. 9: Transmission line model of the structure reported in Fig.1.

The metal–backed dielectric slab is equivalent to a transmission line of length *h* and characteristic impedance $Z_d = Z_0/\sqrt{v_r}$, where $Z_0 = 377\Omega$ is the free-space wave

impedance, terminated in a vanishing impedance Z_L modeling the metallic ground plane. The shunt impedance Z_g represents the averaged impedance of the grid [17], which is a meaningful parameter when the periodicity D is smaller than the operating wavelength. The total surface impedance of the HIS is given by the input impedance Z_s resulting from the parallel connection between the grid impedance Z_g and the line impedance Z_ℓ:

$$Z_s = \left(\frac{1}{Z_g} + \frac{1}{Z_\ell} \right)^{-1} \tag{9}$$

where the input impedance Z_s exhibits an anti-resonant behavior and the structure shows high values of the surface impedance at and around the resonant frequency.

In order to evaluate the grid impedance Z_g, we investigate on the distribution of the electric charges on the array plane when it is illuminated by a plane wave in long-wavelength regime. As shown in Fig. 10, the electric charges are distributed along the curved edges of the metallic circular elements. In the region of minimum distance between the edges of two adjacent vertical patches the electric field amplitude is maximum.
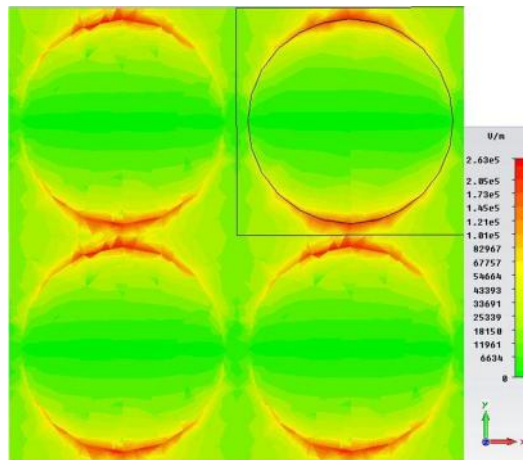
Fig. 10: Map of the electric field amplitude on the plane of an array of circular patches. The exciting electric field is polarized along the *y*-direction.

The distribution of the electric field along the edge is more similar to the one of a squared patch that, under the same condition of excitation, is quite constant along the whole length. In the following we show that, by using a proper modification, the formulas, used for the squared patch case proposed in [21], can be effectively used also for the circular case.

In Fig. 11 I show the squared- and the circular-patch-based structures with the respective geometrical parameters. They have the same periodicity D and the same gap g. The thickness and the electric permittivity of the dielectric slab are also the same. The diameter $2R$ of the circular patches is equal to the length L of the edge of the squared patches.
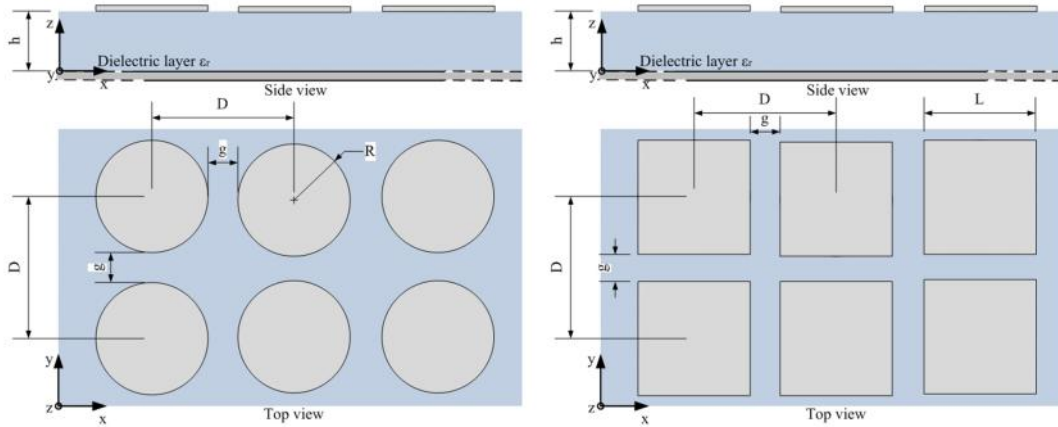
Fig. 11: Side and top views of two High Impedance Surfaces consisting of a regular array of circular (left) and squared (right) patches.

When an uniform plane-wave impinges normally on the surface from the above, the grid impedance Z_g of the HIS with squared patches is given by [17], [21], [37]:

$$Z_g = -j\frac{Z_{eff}}{2\Gamma} \tag{10}$$

where Γ is the grid parameter defined as:

$$\Gamma = \frac{k_{eff} D}{f} \ln\left[\frac{1}{\sin\left(\dfrac{f g}{2D}\right)}\right] \tag{11}$$

and $Z_{eff} = Z_0 \big/ \sqrt{\nu_{eff}}$, $k_{eff} = k_0 \sqrt{\nu_{eff}}$ are the wave impedance and the wave number in the effective medium, respectively, and ν_{eff} is the effective permittivity of the space surrounding the array grid. In fact, according to [24], [38], it is possible to analyze the electromagnetic behavior of a structure at the interface between two dielectrics, one of which is the air, using an effective permittivity $\nu_{eff} = (\nu_r + 1)\big/2$ as if the array elements were embedded in an equivalent effective medium. The formula is accurate for periodic structures whose periodicity is smaller than the operating wavelength and presents a slight dependence on the thickness of the substrate since the electric field lines are confined essentially at the air–dielectric interface due to the proximity of the metallic edges (i.e. the metallic ground plane slightly contribute to the definition of the grid impedance of the array).

In order to modify such formulas for the circular patch case, as reported in Fig. 12, we observe that it is possible to identify a finite region between two adjacent patches where the electric field amplitude is maximum. By applying the integral mean value theorem over this region, an averaged value of the gap g can be evaluated and used in eqs. (10), (11), rectifying, *de facto*, the circular patch in an equivalent squared one with the same periodicity, but with a different value of the gap g. The integration area is shown in Fig. 12. The upper and lower integration limits are given by the edges of the circular patches, while the right and left boundaries can be defined in two alternative ways, considering either the solid or the dotted lines. Solid lines limit the full region following the curvature of ideal electric field lines intersecting orthogonally the metallic edges. Dotted lines, instead, do not consider this curvature, defining a smaller, and less accurate, rectangular region. In the following, we will consider these two cases separately.
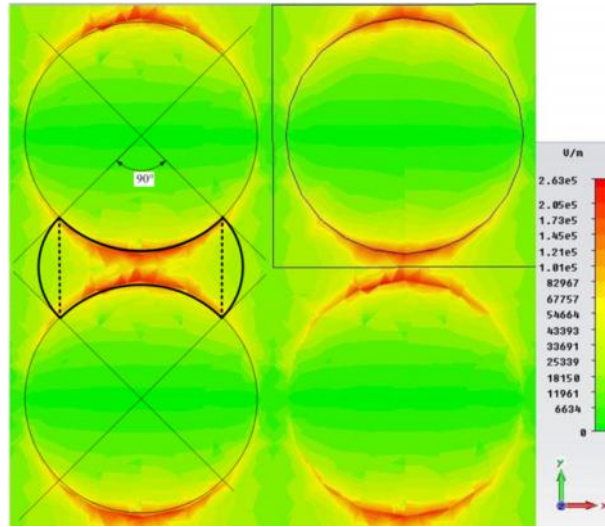
Fig. 12: Full (solid line) and rectangular (dotted line) integrating regions.

RECTANGULAR REGION
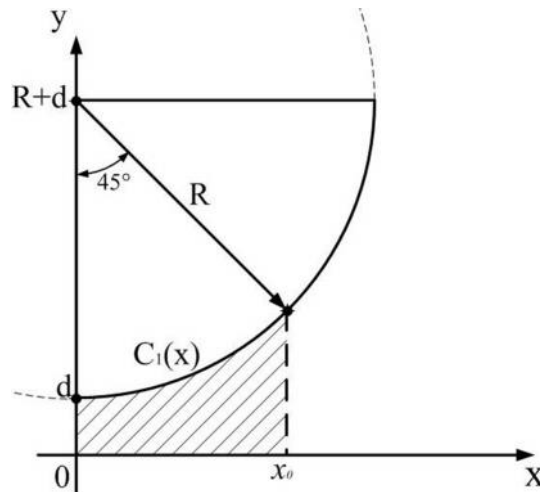
Fig. 13: Rectangular area of integration.

In order to determine the area of the rectangular region, we consider only one quarter of the structure, as shown in Fig. 13. The origin of the rectangular coordinate system is translated between two adjacent patches. The area is defined using *x* and *y* variables as:

$$\begin{cases} 0 \le \mathrm{x} \le \mathrm{x}_0 \\ 0 \le \mathrm{y} \le \mathrm{C}_1\left(\mathrm{x}\right) \end{cases} \tag{12}$$

where x_0 is the maximum value of x in the region of interest and $C_1(x)$ is the function of the arc that identifies the upper limit of the region. The expression of $C_1(x)$ can be found starting from the equation of a circle centered in $\{\overline{x}, \overline{y}\} = \{0, R+d\}$ as:

$$C_1(x) = d + R - \sqrt{R^2 - x^2} \tag{13}$$

The dashed area in Fig. 13 is given by:

$$\int_0^{x_0} C_1(x)\,dx = (d+R)x_0 + $$
$$-\frac{1}{2}\left[R^2 \tan^{-1}\frac{x_0}{\sqrt{R^2 - x_0^2}} + x_0\sqrt{R^2 - x_0^2} \right] \tag{14}$$

Since $x_0 = R/\sqrt{2}$, expression (14) can be simplified as follows:

$$\int_0^{x_0} C_1(x)\,dx = \frac{1}{8}R\left[4\sqrt{2}d + \left(4\sqrt{2} - 2 - f\right)R \right] \tag{15}$$

Now it is possible to evaluate the new averaged value of d between two adjacent patches:

$$\overline{d}_{rect} = \frac{1}{x_0}\int_0^{x_0} C_1(x)\,dx \tag{16}$$

One can express x_0 and R in terms of the periodicity D and of the gap g as:

$$\begin{cases} x_0 = \dfrac{R}{\sqrt{2}} \\[2mm] R = \dfrac{1}{2}(D - g) \\[2mm] g = 2d \end{cases} \tag{17}$$

Using eq. (17) in eqs. (15)-(16), we obtain:

$$\overline{g}_{\text{rect}} = \frac{\left(4\sqrt{2} - 2 - f\right)D + (2 + f)g}{4\sqrt{2}} \tag{18}$$

or, evaluating the numerical coefficients:

$$\overline{g}_{\text{rect}} \cong 0.91g + 0.09D \tag{19}$$

Such an expression can be straightforwardly employed in formulas (10), (11) to estimate the behavior of the circular-patch-based HIS.

FULL REGION
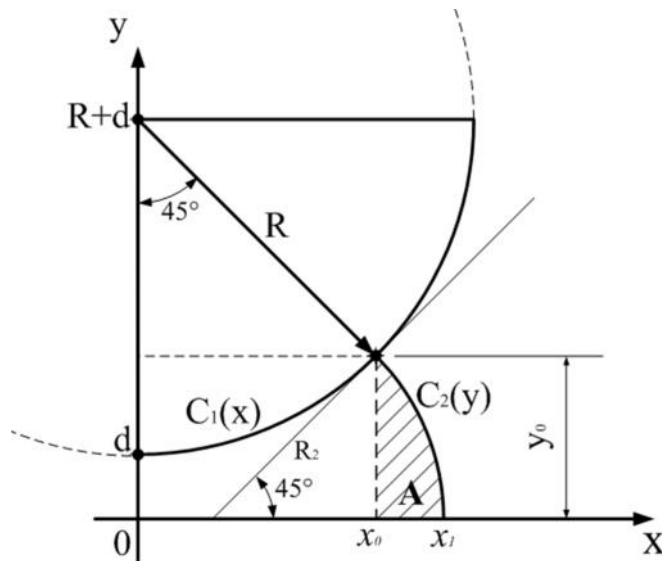
Fig. 14: Full area of integration.

In the case of the full region, the integration area is larger because we consider the area A under the arc of the curve $C_2(y)$, which approximates the electric field lines between two adjacent patches. Being the electric field always orthogonal to metallic surfaces, the arc intersects normally the circumference of the patch. The expression of the curve $C_2(y)$ has been found in the same way as for curve $C_1(x)$ as:

$$C_2(y) = (x_0 - y_0) + \sqrt{R_2^2 - y^2} \tag{20}$$

Only the area A between $C_2(y)$ and x_0 is of interest: the integral of the function $C_2'(y)$ (i.e. function $C_2(y)$ shifted by an amount x_0) is evaluated as:

$$A = \int_0^{y_0} C_2'(y)\,dy = \int_0^{y_0} \left(\sqrt{R_2^2 - y^2} - y_0 \right) dy \tag{21}$$

which returns:

$$A = \int_0^{y_0} C_2'(y)\,dy = -y_0^2 +$$
$$+ \frac{1}{2}\left[y_0 \sqrt{R_2^2 - y_0^2} + R_2^2 \tan^{-1}\left(\frac{y_0}{\sqrt{R_2^2 - y_0^2}} \right) \right] \tag{22}$$

Being $y_0 = R_2 / \sqrt{2}$, eq. (22) can be simplified as:

$$A = \int_0^{y_0} C_2'(y)\,dy = \frac{1}{8}(f - 2)R_2^2 \tag{23}$$

The new averaged value of d between two adjacent patches is:

$$\overline{d}_{full} = \frac{1}{x_1}\left[\int_0^{x_0} C_1(x)dx + \int_0^{y_0} C_2'(y)dy\right] \qquad (24)$$

where $x_1 = x_0 + \left(\sqrt{2}-1\right)y_0$. The two integrals in (24) have been already evaluated in eqs. (15), (23). Consequently, one obtains the expression:

$$\overline{d}_{full} = \frac{1}{2x_1}\left[R\left[4\sqrt{2}d + \left(4\sqrt{2}-2-f\right)R\right] + (f-2)R_2^2\right] \qquad (25)$$

Finally, expressing all the factors in terms of the periodicity D and the gap g, we obtain:

$$\begin{cases} R_2 = \sqrt{2}(R+d) - R \\ x_1 = \left(\sqrt{2}-1\right)(2R+d) \\ R = (D-g)/2 \\ g = 2d \end{cases} \qquad (26)$$

and, thus:

$$\overline{g}_{full} = \frac{1}{8(d-D)}\left[2\left(1+\sqrt{2}\right)g^2 + (f-4)D^2 - \left(\left(2+\sqrt{2}\right)f - 4\right)gD\right] \qquad (27)$$

Again, such an expression can be straightforwardly employed in formulas (10), (11) to estimate the behavior of the circular-patch-based HIS.

1.3.2 Analytical and numerical results

In this Section, we compare the analytical results obtained applying the new proposed models to the ones obtained using the numerical results obtained through CST Microwave Studio. As further comparison we show the results obtained using the sub-wavelength-FSS-based model and the polarizability–based model.

The aim is to show that the first expression of the gap, $\overline{g}_{rect}$, though simple, returns good results, but, generally, the second expression of the gap, $\overline{g}_{full}$, allows obtaining more accurate results.

In order to assess the effectiveness of the proposed model, we first consider its ability to predict the resonance frequency of the HIS. To do that, we define the percentage error on the resonance frequency of the HIS as:

$$\text{err}\% = \frac{f_r^{mod} - f_r^{sim}}{f_r^{sim}} 100 \tag{28}$$

where f_r^{sim} is the resonance frequency of the structure given by the numerical simulator and f_r^{mod} is the one estimated by the model.

The couples (D,g), chosen to test the proposed models, have been collected in cases as shown in Table 1.

CASE	D [mm]	g [mm]
A	3.0	0.30
B	1.0	0.20
C	4.0	0.20
D	1.5	0.05
E	4.0	0.05

Table 1: Couples of values of periodicity *D* and gap *g* of the analyzed structures.

Several different structures with different geometrical dimensions and permittivity values have been simulated. The numerical results are compared to the proposed analytical ones, as shown in Table 2 with the header Rect-region based and Full-region

based, respectively. In the cases A, B, C, and D the resonance frequency is better predicted by the model that uses the expression $\overline{g}_{full}$ for all the three combinations of permittivity and thickness of the substrate. On the contrary, when the periodicity D of the array is much larger than the separation g (case E), the use of $\overline{g}_{full}$ is not recommended any more. In fact, as shown in Fig. 14, the proposed model has been developed considering the region between two adjacent patches under a fixed angle of 90°. On the contrary, in case E, the electric field is strongly confined in the region of minimum distance between two adjacent patches and, when $\overline{g}_{full}$ is evaluated, we overestimate the area in which the electromagnetic energy should be confined. For this reason, $\overline{g}_{rect}$ better predicts the frequency response of the array. However the percentage error is very low for all fifteen configurations, showing the good agreement with the exact full-wave numerical results.

The results of the other analytical models (presented in [16] and [36]) are also shown in Table 2. They both overestimate the resonant frequency of the HIS and return an absolute percentage error which is generally higher than the one of the proposed method. It is worth noticing that only in the case B the other two analytical models are fairly accurate. In this case, in fact, the ratio g/D is smaller compared to the other cases and, thus, the metallic inclusions are more diluted, as required by the models based on the FSS theory [36] and on the polarizability [16].

Substrate Parameters: $\varepsilon_r = 10.2$, h = 1.0 mm								
Case	f_r^{Sim}	Rect-region based		Full-region based		FSS-based		Polarizability-based	
		f_r^{mod}	err%	f_r^{mod}	err%	f_r^{mod}	err%	f_r^{mod}	err%
A	11.99	11.51	**-4.0**	11.87	**-1.0**	13.5	**+12.6**	15.02	**+25.3**
B	19.00	18.11	**-4.7**	18.33	**-3.5**	19.2	**+1.1**	19.70	**+3.7**
C	9.44	9.38	**-0.6**	9.79	**+3.7**	10.91	**+15.6**	13.45	**+42.5**
D	13.65	13.46	**-1.4**	13.9	**+1.8**	15.5	**+13.6**	16.07	**+17.7**
E	8.51	8.72	**+ 2.5**	9.16	**+7.6**	10.4	**+22.2**	13.01	**+52.9**
Substrate Parameters: $\varepsilon_r = 10.2$, h = 2.0 mm								
Case	f_r^{Sim}	Rect-region based		Full-region based		FSS-based		Polarizability-based	
		f_r^{mod}	err%	f_r^{mod}	err%	f_r^{mod}	err%	f_r^{mod}	err%
A	7.79	7.37	**-5.4**	7.53	**-3.3**	8.25	**+5.9**	8.56	**+9.9**
B	10.53	10.16	**-3.5**	10.27	**-2.5**	10.54	**+0.1**	10.64	**+1.0**
C	6.46	6.22	**-3.7**	6.44	**-0.3**	7.2	**+11.5**	7.73	**+19.7**
D	8.59	8.30	**-3.4**	8.52	**-0.8**	9.24	**+7.6**	9.18	**+6.9**
E	5.90	5.83	**-1.2**	6.05	**+2.5**	6.87	**+16.4**	7.45	**+26.3**
Substrate Parameters: $\varepsilon_r = 2.5$, h = 2.0 mm								
Case	f_r^{Sim}	Rect-region based		Full-region based		FSS-based		Polarizability-based	
		f_r^{mod}	err%	f_r^{mod}	err%	f_r^{mod}	err%	f_r^{mod}	err%
A	14.55	13.75	**-5.5**	14.1	**-3.1**	15.51	**+6.6**	16.29	**+11.9**
B	20.50	19.91	**-2.9**	20.03	**-2.3**	20.74	**+1.2**	20.98	**+2.3**
C	11.97	11.45	**-4.3**	11.87	**-0.8**	13.36	**+11.6**	14.58	**+21.8**
D	16.06	15.75	**-1.9**	16.16	**-0.6**	17.7	**+10.2**	17.62	**+9.7**
E	10.90	10.71	**-1.7**	11.15	**+2.3**	12.72	**+16.7**	13.99	**+28.3**

Table 2: Comparison between the resonant frequencies in GHz of 15 different configurations of HISs: f_r^{sim} exact resonant frequency using full-wave simulator; f_r^{mod} using the analytical models.

Three particular configurations have been chosen among the 15 ones reported in Table 2. For all of them the phase of the reflection coefficient has been evaluated as a function of the frequency and compared to the one obtained through the full-wave code (see Fig. 15, Fig. 16, and Fig. 17). The agreement between the proposed model based on the full integrating region and the numerical simulations is rather good in a broad frequency range.
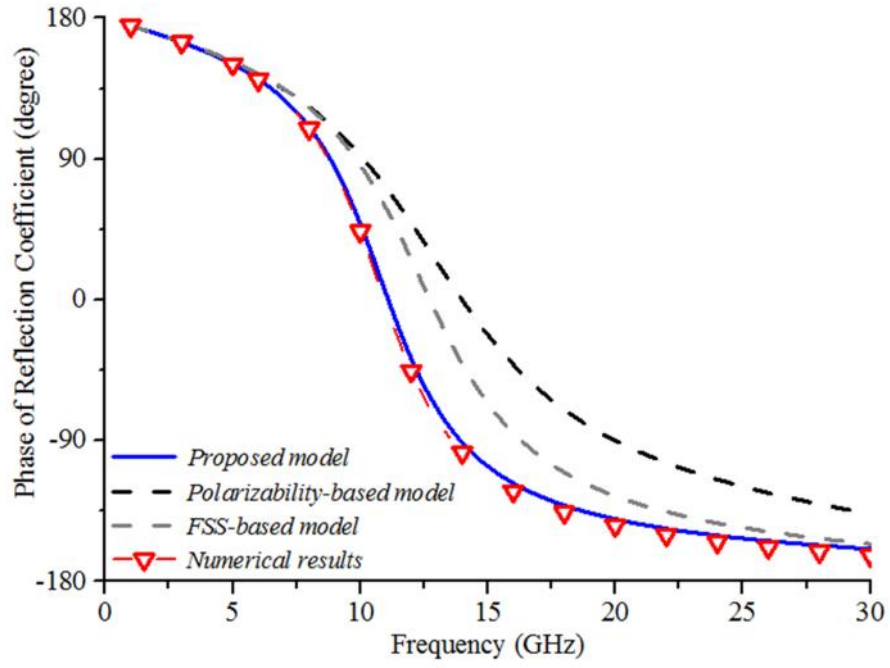
Fig. 15: Phase of the reflection coefficient of an HIS with circular patches ($D = 4\,\text{mm}$, $g = 0.05\,\text{mm}$, $h = 2\,\text{mm}$ and $v_r = 2.5$).
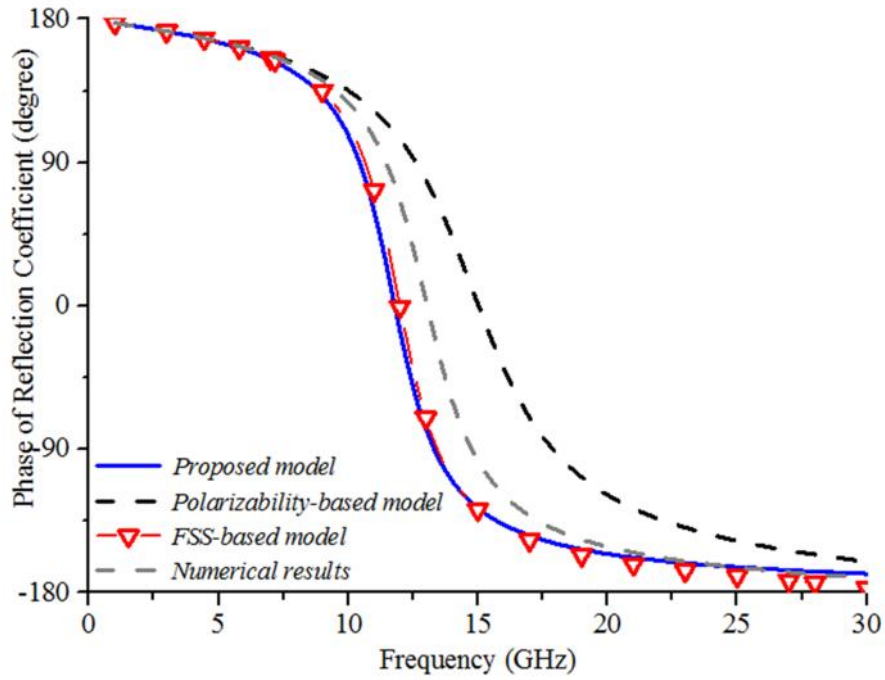
Fig. 16: Phase of the reflection coefficient of an HIS with circular patches ($D = 3\,\text{mm}$, $g = 0.3\,\text{mm}$, $h = 1\,\text{mm}$ and $v_r = 10.2$).
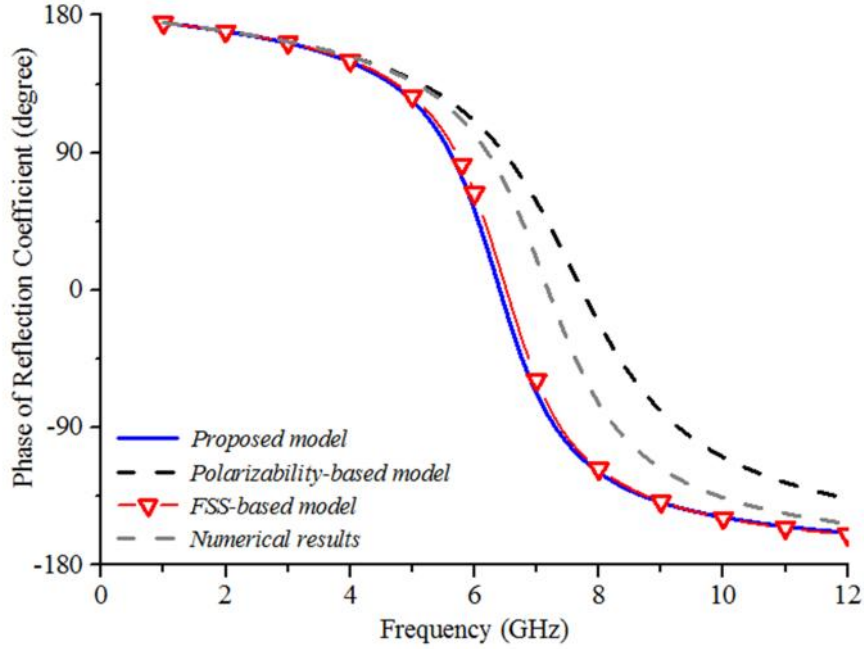
Fig. 17: Phase of the reflection coefficient of an HIS with circular patches ($D = 4\,\mathrm{mm}$, $g = 0.2\,\mathrm{mm}$, $h = 2\,\mathrm{mm}$ and $\nu_r = 10.2$).

1.3.3 Conclusions

In this work, we have presented new accurate analytical formulas for the design of HISs consisting of circular metallic patches excited by a normally impinging plane-wave. The structure can be described using the transmission line theory where a shunt capacitive impedance represents the dense array of circular metallic patches. We have shown that, by inspecting the near-zone electric field distribution around the patches, two sets of new analytical formulas can be derived properly modifying the expression of the grid impedance of a squared-patch-based HIS. They show different degrees of accuracy: the full-region model, which takes into account the curvature of the electric field lines, is generally better, but it gives less accurate results with respect to the rectangular one when the diameter of the patch is much larger than the gap g. However, for several different configurations of HIS, it predicts the frequency behavior of the structure with a low percentage error and a rather good agreement with the full-wave simulation in a broad frequency range, confirming its aspect of general purpose.

The analytical results are compared also with two other models, available in the open technical literature: the sub-wavelength-FSS-based model [36], that has been derived

approximating the Floquet theory under the assumption that the periodicity is few tenths of the operating wavelength, and the polarizability–based model [16], that assumes the inclusions so electrically small that they can be described in terms of an electric dipoles, losing the information about the geometry of the inclusion itself. Except for one case, the models are not able to describe correctly the frequency behavior of the different HISs.

An improvement of the proposed model can be obtained considering a variable integration angle „ as a function of the physical dimension of the array inclusions, rather than a fixed angle of 90°. Future works will be focused on this intriguing aspect, providing eventually a more complete formulation involving also the polarization and the angles of incidence of the impinging plane-wave.

1.4 References

[1]   Bilotti, F., Toscano, A., Vegni, L., "FEM-BEM Formulation for the Analysis of Cavity Backed Patch Antennas on Chiral Substrates," *IEEE Trans. Antennas Propagat.*, Vol. AP-51, pp. 306-311, 2003.

[2]   Bilotti, F., Vegni, L., and A. Toscano, "Radiation and Scattering Features of Patch Antennas with Bianisotropic Substrates," *IEEE Trans. Antennas Propagat.*, Vol. AP-51, pp. 449-456, 2003.

[3]   G. Scamarcio, F. Bilotti, Toscano, A., Vegni, L. ,"Broad band U-slot patch antenna loaded by chiral material," *J. Electromag Waves Applicat.*, Vol. 15, pp. 1303-1317, 2001.

[4]   Bilotti, F., Alù, A., Engheta, N., and Vegni, L. , "Anomalous Properties of Scattering from Cavities Partially Loaded with Double-Negative or Single-Negative Metamaterials," *Progr. Electromag. Res.* (*PIER)*, Vol. 51, pp. 49-63, 2005.

[5]   Bilotti, F., Nucci, L., and Vegni, L., "An SRR Based Microwave Absorber," *Microw. Opt. Technol. Lett.*, Vol. 48, pp. 2171-2175, 2006.

[6]   Bilotti, F., Toscano, A., Vegni, L., Alici, K.B., Aydin, K., and Ozbay, E., "Equivalent Circuit Models for the Design of Metamaterials based on Artificial Magnetic Inclusions," *IEEE Trans. Microw. Theory Tech.*, Vol. MTT-55, pp. 2865-2873, 2007.

[7]   Alù, A., Bilotti, F., Engheta, N., and Vegni, L., "Sub-Wavelength Planar Leaky-Wave Components with Metamaterial Bilayers," *IEEE Trans. Antennas Propagat.*, Vol. AP-55, pp. 882-891, 2007.

[8]   Bilotti, F., Tricarico, S., and Vegni, L., "Electromagnetic cloaking devices for TE and TM polarizations," *New J. Phys.*, Vol. 10, 115035, 2008.

[9]   Bilotti, F., Alù, A., and Vegni, L., "Design of Miniaturized Metamaterial Patch Antennas with μ-Negative Loading," *IEEE Trans. Antennas Propagat.*, Vol. AP-56, pp. 1640-1647, 2008.

[10]   Bilotti, F., Toscano, A., Alici, K.B., Ozbay, E. and Vegni, L., "Design of miniaturized narrowband absorbers based on resonant magnetic inclusions," *IEEE Trans. Electromag. Comp.*, Vol. 53, pp. 63-72, Feb. 2011.

[11]   Tretyakov, S.A., Maslovski, S.I., and Belov, P.A., "An analytical model of metamaterials based on loaded wire dipoles," *IEEE Trans. Antennas Propagat.*, Vol. 51, pp. 2652–2658, 2003.

[12]   Belov, P.A., and Simovski, C.R., "Subwavelength metallic waveguides loaded by uniaxial resonant scatterers," *Phys. Rev. E,* Vol. 72, p. 036618, 2005.

[13]   Guèrin, N., Enoch, S., Tayeb, G., Sabouroux, P., Vincent, P., and Legay, H., "A metallic Fabry-Perot directive antenna", *IEEE Trans. Antennas Propagat.*, Vol. AP-54, pp. 220–224, 2006.

[14]   Kumar, A., and Hristov, H.D., *Microwave Cavity Antennas*, Artech House, New York, 1989.

[15]   Yang, F., and Rahmat-Samii, Y., "*Electromagnetic Band Gap Structures in Antenna Engineering*", Cambridge University Press, 2008.

[16]   Viitanen, A.J., Hanninen, I., and Tretyakov, S., "Analytycal Model for regular dense arrays of planar dipole scatteres," *Progr. Elettromag. Research (PIER)*, Vol. 38, pp. 97–110, 2002.

[17] Tretyakov, S., *Analytical modeling in applied electromagnetic*, Artech House, Boston, 2003.

[18] Yatsenko, V.V., Tretyakov, S.A., Maslovski, S.I., Sochava, A.A., "Higher order impedance boundary conditions for sparse wire grids" *IEEE Trans. Antennas and Propag.*, Vol. 48, No. 5, pp.720-727, 2000.

[19] Yatsenko, V.V., Maslovski, S.I., and Tretyakov, S.A., "Electromagnetic Interaction of parallel arrays of dipole scatterers", *Prog. in Electromagnetic Research*, Vol. 25, pp. 285-307, 2000.

[20] Tretyakov, S.A. and Viitanen, A., "Line of periodically arranged passive dipole scatterers," *Electrical Engineering*, Vol. 82, pp. 353–361, 2000.

[21] Luukkonen, O., Simovsky, C.R., Granet, G., Goussetis, G., Lioubtchenko, D., Raisanen, A., and Tretyakov, S., "Simple and accurate analytical model of planar grids and high-impedance surfaces comprising metal strips," *IEEE Trans. Antennas Propagat.*, Vol. AP-56, pp.1624–1632, 2008.

[22] CST Studio Suite 2010, Computer Simulation Technology, http://www.cst.com.

[23] Marcuvitz, N, "*Waveguide Handbook*", McGraw-Hill Book Company, 1951.

[24] Compton, R.C., Whitbourn, L.B., and McPherdan, R.C., "Strip gratings at a dielectric interface and application of Babinet's principle," *Appl. Opt.,* Vol. 23, pp. 3236-3242, 1984.

[25] Bilotti, F., and Vegni, L., "Chiral Cover Effects on Microstrip Antennas," *IEEE Trans. Antennas Propagat.*, Vol. AP-51, pp. 2891-2898, 2003.

[26] Vegni, L., Toscano, A., and Bilotti, F., "Shielding and Radiation Characteristics of Planar Layered Inhomogeneous Composites," *IEEE Trans. Antennas Propagat.*, Vol. AP-51, pp. 2869-2877, 2003.

[27] Ziolkowski, R.W., and Engheta, N., Eds., *IEEE Trans. Antennas Propagat.*, Special Issue on Metamaterials, Vol. AP-51, 2003.

[28] Vardaxoglou, J.C., *Frequency Selective Surfaces: Analysis and Design*, Research Studies Press, Taunton, England, 1997.

[29] Bilotti, F., Nucci, L., and Vegni, L.,"An SRR Based Microwave Absorber," *Microw. Opt. Technol. Lett.*, Vol. 48, pp. 2171-2175, 2006.

[30] Sievenpiper, D., Zhang, L., Broas, R.F.J., Alexopolous, N., Yablonovitch, E., "High-impedance electromagnetic surfaces with a forbidden frequency band," IEEE Trans. Microw. Theory Tech., Vol. MTT-47, pp.2059–2074, 1999.

[31] Sievenpiper, D., High-impedance electromagnetic surfaces, PhD. Dissertation, UCLA, 1999. Available at www.ee.ucla.edu/labs/photon/thesis/ThesisDan.pdf.

[32] De Cos, M.E., Alvarez, Y., and Las-Heras, F., "A novel approach for RCS reduction using a combination of artificial magnetic conductors," Progr. in Electromagn. Research (PIER), Vol. 107, pp.147–159, 2010.

[33] Chang, C.S., Li, J.Y., Lin, W.J., Houng, M.P., Chen, L.S., and Lin, D.B., "Controlling the frequency of simultaneous switching noise suppression by using embedded dielectric resonators in high impedance surface structure," Progr. Electromagn. Research Lett., Vol. 11, pp.149–158, 2009.

[34] De Cos, M.E., Alvarez, Y., Hadarig, R., and Las-Heras, F., "Flexible uniplanar artificial magnetic conductor," Progr. in Electromagn. Research (PIER), Vol.106, pp.349–362, 2010.

[35] Sievenpiper, D., Yablonovitch, E., Winn, J.N., Fan, S., Villeneuve, P.R., and Joannopoulos, J.D., "3D Metallo-Dielectric Photonic Crystals with Strong Capacitive Coupling between Metallic Islands," Phys. Rev. Lett., Vol. 80, pp. 2829–2832, 1998.

[36] Zarrillo, G., and K. Aguiar, "Closed-form low frequency solutions for electromagnetic waves through a frequency selective surface", IEEE Trans. Ant. & Propag., Vol. AP-35, No. 12, 1987.

[37] Lee, S., G. Zarrillo, and C. L. Law, "Simple formulas for Transmission trough periodic Metal Grids or Plattes", *IEEE Trans. Ant. & Propag.*, Vol. AP-30, No. 5, 1982.

[38] Timusk, T., and Richards, P.L., "Near millimeter wave bandpass filters," *Appl. Opt.,* Vol. 20, pp.1355–1360, 1981.

2 Metamaterial-based filter element for waveguide applications

In this chapter, I present the analytical model of the bi-omega particle consisting of two opposite-oriented and spaced omega resonators. Properly placing the two omega particles very close to each other, the coupling effect between them contributes to shift down the resonant frequency, achieving a simple and deeply electrically small inclusion working in the microwave frequency range. The proposed model, based on the small antenna theory, takes into account all the coupling effects that comes into play when the distance between the two omegas is very small. Then, two bi-omega particles are connected together, in order to obtain a transfer of energy from one bi-omega, used as receiving antenna, and the other, the transmitting antenna, when it is placed across a slit in a metallic screen. Due to its resonant behavior, the proposed structure can be successfully used as pass-band filter able to select the frequency of interest with high accuracy, which is strongly required in many waveguide and aperture antenna applications. Among them, I present the design and the experimental realization of innovative microwave components, such as waveguide filters, diplexers, power-splitters, modal filters, horn antennas, etc. The ideas are verified through proper full-wave numerical simulations and experimental results.

2.1 Introduction

In the last decades, resonant electrically small scatterers have attracted the attention of the scientific community due to their appealing employment in the realization of artificial materials and to the realization of new compact narrowband components.

If we consider the artificial materials, as well as metamaterials, they are composed by metallic scatterers properly arranged in a dielectric host medium. Such inclusions behave as the molecules of usual polarizable materials, and the shape and the dimensions of the scatterers define the effective electric and magnetic response to an electromagnetic excitation. According to the homogenization constrains, in order to describe the metamaterial in terms of effective dielectric parameters, the dimensions of the scatterers need to be much smaller than the operating wavelength in the host medium [1]. On the other hand , resonant electrically small inclusions in stand-alone configuration can be successfully used as a simple compact resonator for realizing metamaterial-inspired electrically small antennas [2]-[5]. Moreover, smaller inclusions let to squeeze the metamaterials samples to be employed in new ever more compact devices. For this reason, one of the main scientific/technical issues in this research field is to conceive, and properly model, smaller and smaller sub-wavelength inclusions. As far as magnetic metamaterial inclusions are concerned, one approach is to couple two or more magnetic particles, such as split-ring resonators (SRRs) in edge- and broad-side direction [6], or to increase the number of rings [7]. In this framework, the omega particle [8]-[9] exhibits a lower resonant frequency than a single-ring SRR with the same dimensions does. This is due to presence of the stems acting as an electrically small electric dipole, i.e. a capacitive load. Moreover, as for the SRRs, properly placing two omega particles very close to each other, the coupling effect between them contributes to shift down the resonant frequency, achieving, thus, dramatically electrically small inclusions.

Here, I consider a bi-omega particle, which consists of two opposite-oriented and spaced omega resonators, as shown in Fig.1, that can be employed as the unit-cell for a negative permeability (i.e. MNG) metamaterial or as a simple stand-alone compact resonator. Since the particle dimensions are sub-wavelength, we describe the

electromagnetic behavior of the bi-omega particle by using an equivalent circuit model, which takes into account all the electric and magnetic coupling effects between the two single omegas. The results of the analytical model are compared to the numerical ones, showing a very good agreement.

Then, I consider two bi-omega particles connected together by the means of their omega arms. This structure is employed to effectively transmit power through sub-wavelength apertures, that is one widespread applications of metamaterials. In fact the metamaterial concepts have been exploited to efficiently transmit power through sub-wavelength apertures drilled in an opaque screen [10]-[19]. In this framework, one of the proposed approaches is based on the excitation of a strong magnetic or electric dipole resonance at the aperture or in its close proximity [14], [15], [19]. For instance, in [15] it has been numerically and experimentally demonstrated that it is possible to efficiently transmit power through an aperture by placing a single split-ring resonator in front of the aperture itself. A further extension of this approach has been proposed in [19], where two split-ring resonators (disconnected or connected to each other) are used at both sides of the aperture. It is worth noticing that in [14], [15], [19], this transmission phenomenon has been referred to as enhanced transmission (or extraordinary transmission), in order to remark that the resonators, placed across or in close proximity of an electrically small aperture, enable an enhancement of the transmission with respect to the case of the aperture alone. Though this definition is still rather controversial, because it can be argued that the term enhanced transmission has been originally referred to somehow loaded resonating apertures (i.e. the aperture itself plays a role in the transmission enhancement, thanks to the presence of additional non-resonating structures), the resulting effect of increasing the power extracted from or passing through a sub-wavelength aperture is, anyway, of interest for several applications, such as electrically small radiating apertures, aperture coupling in waveguide components, self-filtering aperture and waveguide components, efficient scanning and imaging probes, etc.

In the following, by exploiting the equivalent circuit representations of the planar omega resonators [20]-[21], I first derive the equivalent circuit of the individual bi-

omega particle and I verify it through proper full-wave numerical simulations. Then, I show the operation of the connected bio-omega particle.

2.2 The bi-omega particle

As previously mentioned, a bi-omega inclusion consists of two opposite-oriented omega resonators, spaced by the quantity d (Fig. 18). Each omega is composed by an electrically small loop of radius a and an electrically small dipole of length ℓ, connected by a pair of metallic strips of length h separated by a gap g. The width of the metallic strip is w.
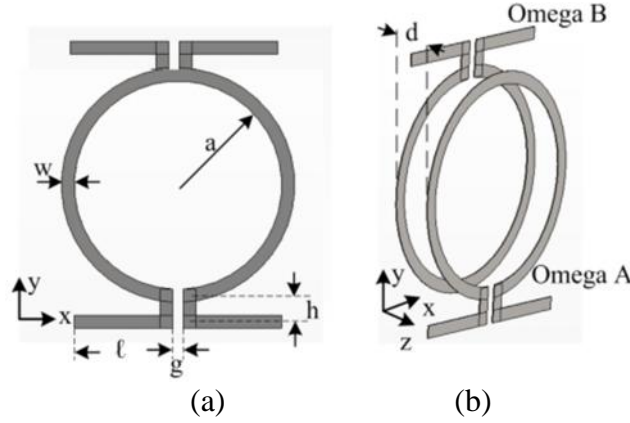
Fig. 18: Geometrical sketch of the bi-omega particle: (a) front and (b) prospective view.

In order to have a magnetic response from the particle, it is excited by a magnetic field parallel to the loop axis $\mathbf{H} = H_z \hat{\mathbf{z}}$ and an electric field parallel to the loop plane $\mathbf{E} = E_y \hat{\mathbf{y}}$. According to the small antenna theory [22], the *single omega* particle can be studied, in first approximation, as the parallel connection of the small loop antenna impedance Z_l and the small dipole one Z_d, as already done for similar chiral inclusions [23] (see Fig. 19).
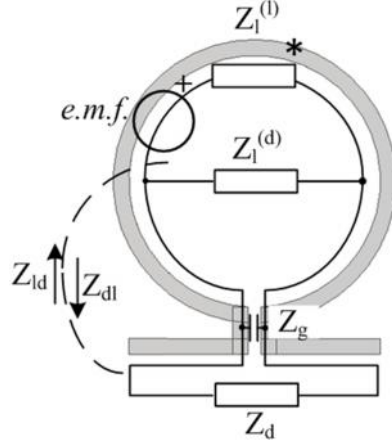
Fig. 19: Equivalent circuit model of the single omega particle (graphical representation).

The loop impedance Z_l is given by both contributions of the loop antenna impedance $Z_l^{(l)}$ and the electric dipole of the loop $Z_l^{(d)}$. So:

$$\frac{1}{Z_l} = \frac{1}{R_l^{(l)} + j\check{S}L_l} + \frac{1}{R_l^{(d)} + 1/(j\check{S}C_l)} = \frac{1}{Z_l^{(l)}} + \frac{1}{Z_l^{(d)}} \tag{29}$$

where $R_l^{(l)}$, $R_l^{(d)}$ are the radiation resistances, L_l, C_l are the self-inductance and capacitance of the loop and of the electric dipole of the loop, respectively. Similarly, the equivalent impedance of the dipole connected to the loop is given by:

$$Z_d = R_d + \frac{1}{j\check{S}C_d} + j\check{S}L_d \tag{30}$$

The lumped circuit elements of both impedances Z_l and Z_d can be found in [22]:

$$R_l^{(l)} = (k^2 S)^2 \frac{y}{6f}; \qquad R_l^{(d)} = (k\,a)^2 \frac{y}{6f}$$

$$C_l = \frac{vf^2 a}{3\ln(2a/w)}; \quad L_l = \text{~}a\left[\ln\left(\frac{16a}{w}\right) - 2\right] \tag{31}$$

$$R_d = (k\,l)^2 \frac{\mathsf{y}}{6f}; \quad C_d = \frac{\mathsf{v}f\,l}{\ln(4l/w)}; \quad L_d = \frac{\sim l}{3f}\left[\ln\left(\frac{4l}{w}\right) - \frac{11}{6}\right] \tag{32}$$

Although this model was fairly accurate for chiral scatterers where the loop plane is orthogonal to the dipole axis, it is not when I consider a planar omega inclusion because the electric dipole moment of the loop and the one of the stems couple and the resonant frequency is no more predicted by the simple small antenna model described just before.

The mutual impedance due to coupling between two small dipolar antennas can be derived, modifying the dipole antenna impedance of a short dipole [22]. A dipole can be seen as a transmission line divaricated at its end of the quantity ℓ, i.e. the semi-length of the dipole. If it is a simple open-circutic segment of transmission line, its input impedance will be:

$$Z_{in}^{o.c.} = -jZ_c \cot(k\ell) \tag{33}$$

where Z_c is the characteristic impedance of the line. However, when the last part of the line is divaricated to get the dipole, its characteristic impedance change and it can be evaluated using the characteristic impedance of a biconical antenna in the case limit of small angle of the cone [22]:

$$Z_{ant} = 120\left[\ln\left(\frac{2\ell}{r_0}\right) - 1\right] \tag{34}$$

where r_0 is the radius of the dipole. Now, if we extend this concept to two short dipoles very close to each other, I can approximate the antenna impedance seen by the receiving antennas as the one seen by a biconical antennas whose radius is the distance between them. So, coming back to our problem, the coupling between the dipole and the electric dipole moment of the loop is identified by two mutual impedances, called Z_{dl} and Z_{ld} according to the active antenna and the receiving one:

$$Z_{dl} = -jZ_{ant}^{(l)} \cot(ka)$$
$$Z_{ld} = -jZ_{ant}^{(d)} \cot(k\ell)$$

(35)

where $Z_{ant}^{(l)}$, $Z_{ant}^{(d)}$ are the characteristic impedances of the antennas [22], which can be written for our geometry as follows:

$$Z_{ant}^{(l)} = 120\left[\ln\left(\frac{2a}{a+h+w/2}\right)-1\right]$$
$$Z_{ant}^{(d)} = 120\left[\ln\left(\frac{2\ell}{a+h+w/2}\right)-1\right]$$

(36)

Moreover, a capacitive reactance Z_g models the capacitive coupling between the short metal strips that connect the loop to the dipole:

$$Z_g = -j\left(\check{S}v(w+h)\frac{K(\sqrt{1-k^2})}{K(k)}\right)^{-1} ; \quad k = \frac{g}{2w+g}$$

(37)

where $K(\cdot)$ is the complete elliptic integral of the first kind. Finally, due to the considered excitation, the circuit is fed by an electromotive force *e.m.f.* induced on the loop portion of the omega particle by the variation of magnetic field B_z across the electrical cross-sectional area S of the loop:

$$e.m.f. = -j\check{S}B_z S$$

(38)

In order to evaluate the Thevenin impedance connected to the termination of the voltage source generator, *e.m.f.,* I represent the equivalent circuit of Fig. 19 according to the standard electro–technical circuit representation:
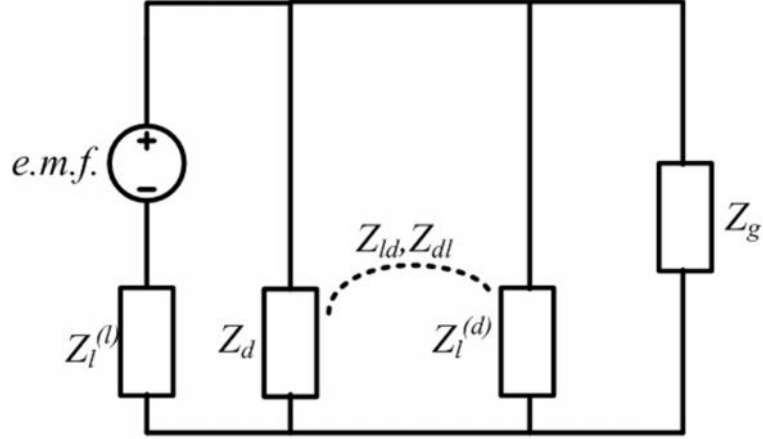
Fig. 20: Equivalent circuit model of omega particle (standard representation).

The equivalent Thevenin impedance reads:

$$Z_{TOT} = Z_l^{(l)} + \left(\frac{1}{Z_d + Z_{dl}} + \frac{1}{Z_l^{(d)} + Z_{ld}} + \frac{1}{Z_g} \right)^{-1} \tag{39}$$

and the current that flows in the circuit is:

$$I = -j \frac{\check{S} \sim H_z S}{Z_{TOT}} \tag{40}$$

At the resonance, the imaginary part of Z_{TOT} vanishes and the current that flows in the circuit is maximum, leading to the maximum scattering exhibited by the electrically small particle. In order to verify this, I set a proper full-wave simulation [24] where the particle is assumed to be in free-space and with the following dimensions: $a = 4.0 \ mm$; $\ell = 4.0 \ mm$; $g = 0.4 \ mm$; $h = 0.5 \ mm$; $w = 0.5 \ mm$. It is illuminated by a unit-amplitude plane-wave, having the magnetic field directed as the axes of the loops and the electric field parallel to the loop plane. We have put a magnetic field probes at the centers of the loop to record the component of the magnetic field directed as the loop axis. The result of this exercise is represented in Fig. 21 where the comparison between the current I and the field reordered by the magnetic probe versus frequency is shown.
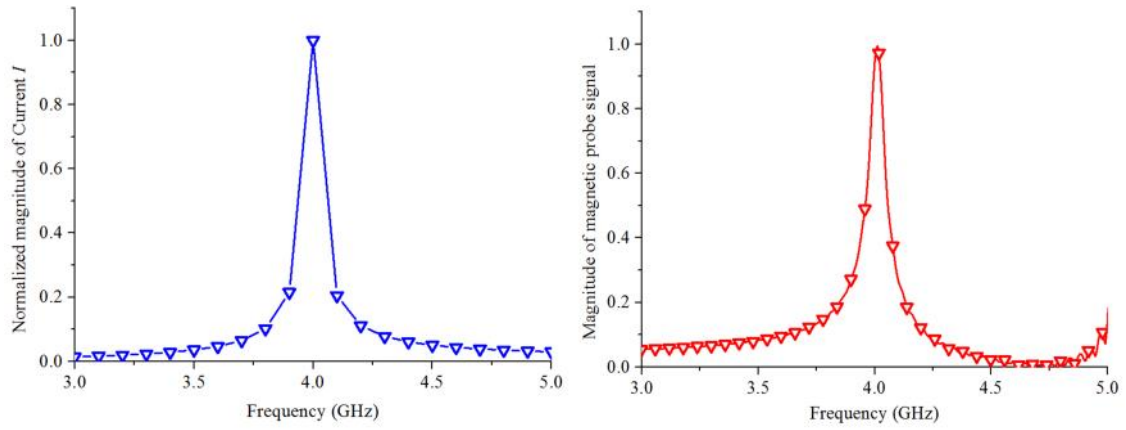
Fig. 21: Resonant frequency predicted by the model (left) and the numerical result (right).

As expected, at the resonant frequency the current flowing on the metallic loop is maximum and also the scattering. Thanks to the full-wave simulator, I can show the scattering parameter of the particle and, as inset, the representation of the currents at the resonant frequency. The result is reported in
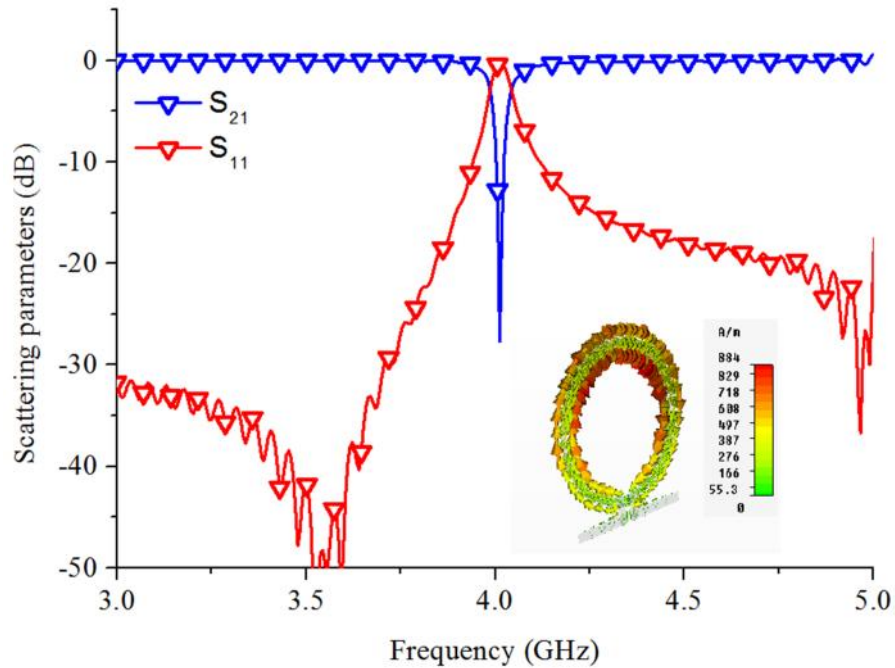
Fig. 22: Scattering parameters of a TEM waveguide filled with one omega particle. Inset: Representation of surface current at the resonant frequency.

When a second omega particle is placed very close to the first one, to get the *bi-omega particle* (Fig. 18), several coupling effects come into play and need to be modeled. In Fig. 23, I indicate with dash lines all the electric couplings between the dipolar components of the two particles. The starred elements, instead, i.e. the two loop impedances, are magnetically coupled since the currents flow in the same direction, according to the Biot–Savart law. The mutual impedances between the elements can be evaluated as in eqs. (33), (34) properly setting the parameters. The loop mutual impedance due to the loop current can be evaluated as follows [25]:

$$Z_{ll} = -j\check{S}\frac{1}{2} \sim S\frac{a^2}{\sqrt{\left(a^2+d^2\right)^3}} \tag{41}$$

So the equivalent circuit model for two omega particle in broadside coupling is reported in Fig. 23.
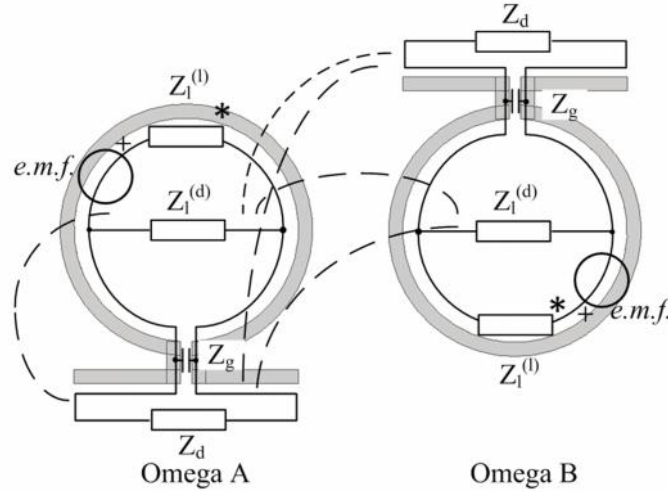
Fig. 23: Equivalent circuit model of the bi-omega particle with mutual impedances given by the electric (dash lines) and magnetic coupling (starred elements).

In order to verify the effectiveness of the model presented, I evaluate the resonant frequency of the bi-omega particle with the same procedure of reported for the single one for different values of the spacing d. The geometrical dimensions are the same of the previous example. In this case, I focus my attention of the spacing d because it is the

key parameter to test the correct modeling of all the coupling effects that come into play. In Fig. 24, we report the comparison of the analytical and numerical results obtained by a properly set of full-wave electromagnetic simulations. The results show a very good agreement, proving the effectiveness of the proposed model. It is worth noticing that for very small values of the spacing d, the resonant frequency shifts down, leading to a further miniaturization of the entire inclusion. As the distance increases, the coupling effects decrease and the resonant frequency of the bi-omega particle tends to the one of the stand-alone omega inclusion.
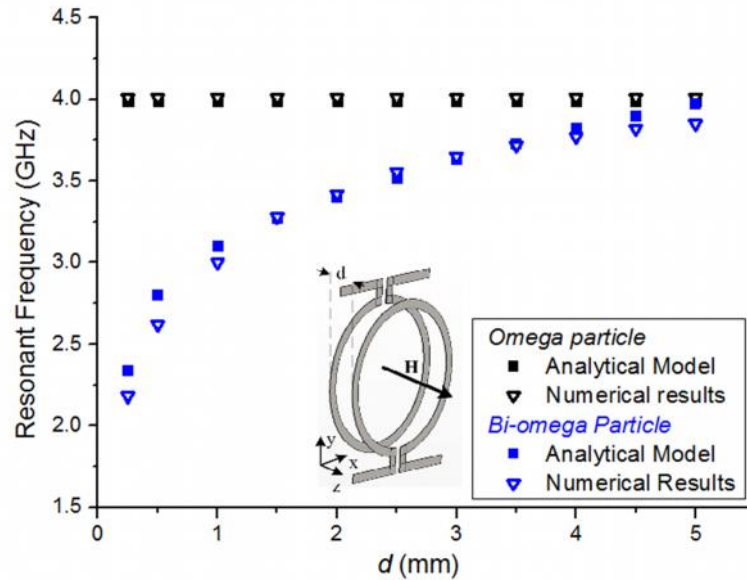
Fig. 24: Comparison between analytical and numerical results of the resonant frequency versus distance d between omegas.

2.3 Connected bi-omega particle

Now I consider two bi-omega particles connected bi-omega particle depicted in Fig. 25.
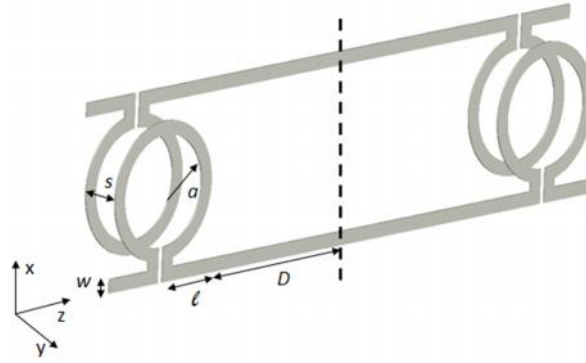
Fig. 25: Geometry of the connected bi-omega particle.

The structure consists of two individual bi-omega particles connected through a transmission line having length equal to 2D. As for any symmetric structure, it is possible to assume that the connected bi-omega particle supports two fundamental modes, having event and odd field symmetries, respectively. Such modes can be easily studied considering only half of the structure and terminating it on either a perfect magnetic or a perfect electric wall, respectively. This means that the equivalent circuit model of Fig. 23 needs to be loaded with a transmission line stub with length D terminated on either an open- or a short-circuit. By using such representations, it is possible to estimate the resonant frequencies of the two fundamental modes supported by such a symmetric structure as reported in.
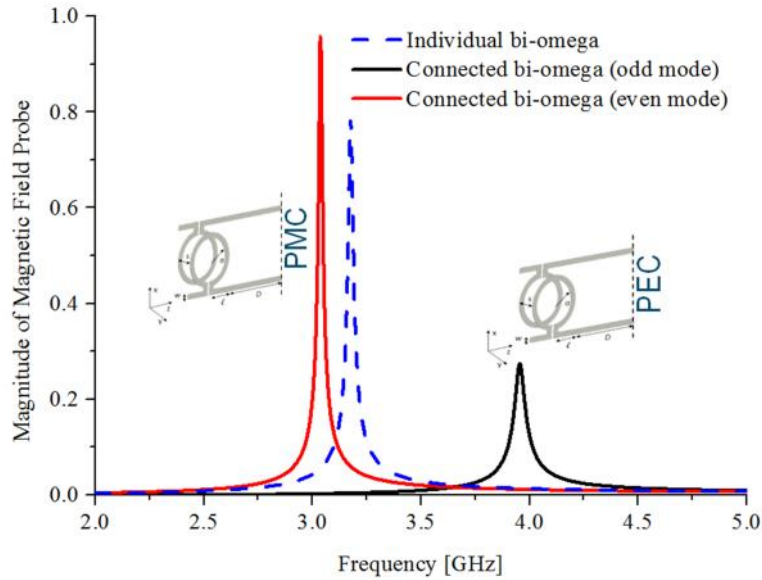
Fig. 26: Numerical results for even and odd modes of the connected bi-omega particle.

The two predicted resonant frequencies for the even and odd modes are 3.04 GHz and 3.94 GHz, respectively. It is worth noticing that the individual bi-omega particle resonates at an intermediate frequency. In the case of the even mode of the connected bi-omega particle, in fact, the loading stub returns a capacitive impedance (open-circuit termination), which slightly lowers the resonant frequency of the individual bi-omega particle, while in the case of the odd mode, the loading stub returns an inductive impedance (short-circuit termination) which, as expected, causes an increase of the resonant frequency in comparison to the one of the individual bi-omega particle.

To further validate the model, we show in Fig. 27 the current density distributions on the metallizations of the connected bi-omega particle at the two resonant frequencies. In the left panel, we see the expected even mode behavior, characterized by an electromagnetic coupling between the two bi-omega particles, even though they are physically connected by the metallic arms. In the right panel, instead, we see that, as expected, at the odd mode resonance the arms are strongly excited. Basically, while the even symmetry of the electric field does not allow a voltage drop along the metallic arms at the lower resonant frequency, the odd symmetry of the electric field at the higher resonant frequency, instead, causes a strong voltage drop between the two ends of the arms and, thus, strong currents flow along the connecting transmission line.
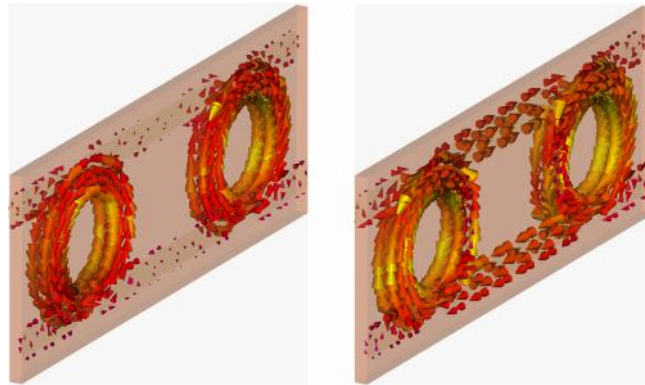
Fig. 27. Simulated current density distributions on the metallizations of the connected bi-omega particle at *3.04 GHz* (left) and at *3.94 GHz* (right).

2.4 Metamaterial-inspired waveguide filter

The connected bi-omega particle is an interesting structure to realize a *metamaterial-inspired filtering module* based on the intriguing concept of enhanced transmission. In order to verify such functionality, the connected bi-omega particle has be placed across a sub-wavelength aperture in an infinitely extended metallic screen as shown in Fig. 28. The metallic screen is illuminated from the left by an horn antenna that excites, at the resonant frequency, the bi-omega particle. The connection between the two bi-omegas let to transfer the energy from the receiving bi-omega to the transmitting one. A second horn antenna captures the signal radiated by the transmitting b-omega in the right semi–infinite space.
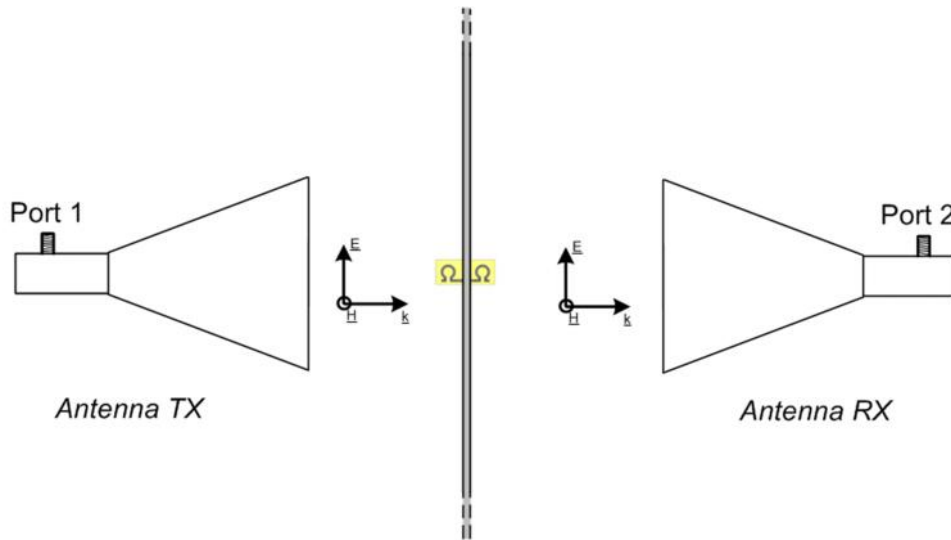
Fig. 28: Free-space measurement setup: the connected bi-omega particle is placed across an aperture in a metal screen.

The metal screen with the aperture has been placed between two identical standard horn antennas (WR 284 and WR 187 waveguide dimensions have been used to cover the frequency range between *3* and *6 GHz*). The system has been calibrated setting the S21 scattering parameter equal to 0 dB when the metal screen with the aperture is present. Then, the inclusion has been placed across the aperture and the transmission spectra have been acquired by using a vector network analyzer connected to the horn

antennas. The acquired scattering parameter S21, thus, corresponds to the transmission enhancement factor due to the presence of the connected bi-omega particle across the aperture with respect to the case of the aperture alone. This result has been reported in Fig. 29 and, comparing it to the corresponding ones shown in Fig. 26, we find an excellent agreement among analytical, numerical, and experimental data.
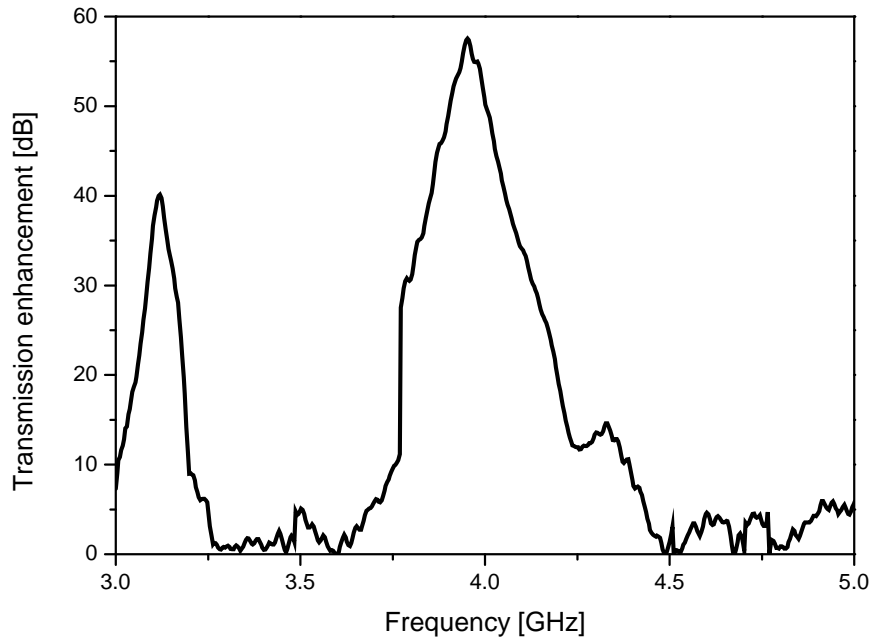
Fig. 29: Measured transmission enhancement as a function of the frequency.

Due to the electrically small dimensions of the entire filtering module, it can be integrated in a regular waveguide as shown in Fig. 30. A metallic screen with a drilled rectangular aperture is used to cover the cross-section of a regular WR 90 waveguide (the theoretical cut-off frequency is *6.56 GHz*). The idea is to design a connected bi-omega particle whose fundamental modes work within the mono-modal frequency range of the waveguide in such a way to obtain a frequency selective transmission. By using the following geometrical and material parameters (*a = 1 mm, l = 1.8 mm, w = 0.4 mm, h = 0.5 mm, D = 1.85 mm*, being the slab parameters $_r$ *= 2.7, s = 0.762 mm*.), and assuming again the omegas excited by a magnetic field component orthogonal to the loops plane, the analytical model developed predicts two resonant frequencies at *7.7 GHz* and *10 GHz* for the even and the odd mode, respectively.
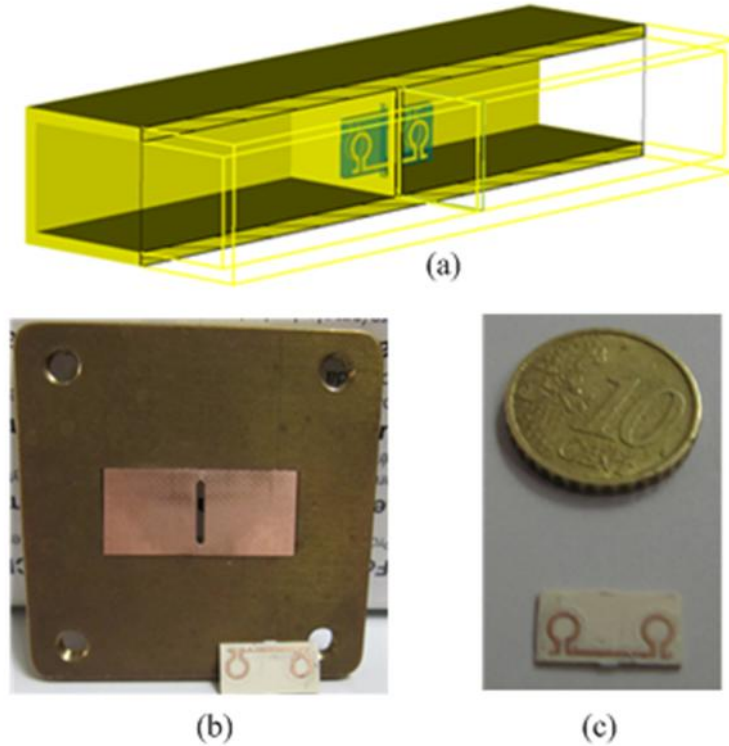
Fig. 30. (a) A metallic screen with a drilled rectangular aperture is used to cover the cross-section of a WR 90 waveguide. (b) Photo showing the fabricated filter element and (c) the fabricated connected bi-omega particle.

I realize the same particle on a 12 mm x 4 x 0.762 mm GML 2032 (r = 2.7 and tan = 0.0025) dielectric board and placed across a rectangular slit according to the setup sketched in Fig. 10. The omega particles at the entrance face of the screen are expected to be excited by the transverse (with respect to the waveguide axis) component of the magnetic field of the fundamental TE10 mode. In order to test the transmission properties of the structure shown in Fig. 10, we have built the experimental setup by using two WR 90 waveguide straight sections sandwiching a sample holder. The metallic screen has been obtained by using a 0.762 mm thick GML 2032 slab with copper metallization on both sides. The slab has been cut with the same dimensions of the WR 90 cross-section and a rectangular slit with dimensions 4 mm x 1 mm has been drilled on it. Finally, the screen has been placed inside the sample holder and the dielectric board with the printed omegas has been fixed across the slit.

I simulate the structure by using CST Studio Suite and the numerical results shown in Fig. 31. The obtained resonant frequencies for the two modes are 7.67 GHz

and 9.94 GHz, respectively. This result confirms also the robustness of the connected bi-omega particle against the variation of the surrounding environment, resulting in a straightforward design of the particle, whatever is the layout where it is used.
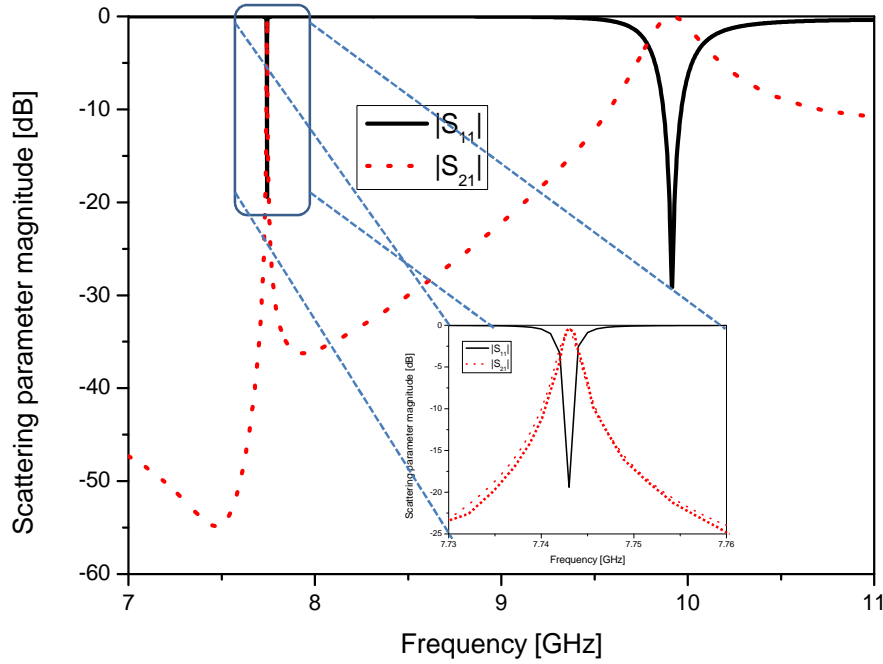
Fig. 31. Magnitude of the simulated scattering parameters for the structure depicted in Fig. 30.

After the numerical verification of the efficient transmission at the resonant frequencies of the two fundamental modes of the connected bi-omega particle, we have conducted also the experiments. Considering that the suggested operation range of the WR 90 waveguide is *8.2-12.4 GHz*, the first resonance at *7.67 GHz* (though being above the theoretical cut-off of the waveguide) cannot be accurately measured. Therefore, I have focused my attention on the second resonance only (i.e. the one at *9.94 GHz*). After a proper TRL calibration of the measurement setup at the sample holder section, I have measured the scattering parameters at the two ports of the waveguide by using a vector network analyzer in two cases: a) presence of the slotted screen only, b) presence of the screen with the connected bi-omega particle fixed across the slit. In Fig. 32, I show the comparison between the experimentally measured and the numerically computed scattering parameter magnitudes in the frequency range *9-11 GHz*. Again, the agreement between numerical and experimental results is very good.
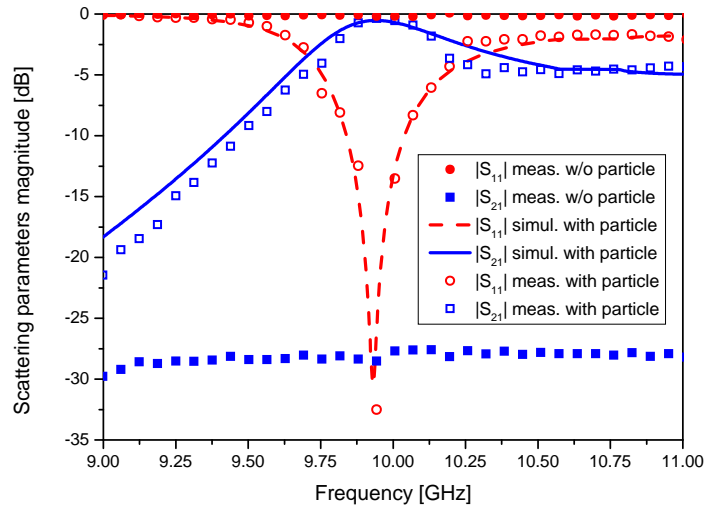
Fig. 32: Comparison between simulated and measured magnitudes of the scattering parameters of the waveguide depicted in Fig. 30.

2.5 Self-filtering horn antenna

Horn apertures find application as feeds for reflector antennas and are used for point-to-point radio links [26]. A typical application is in the receiving modules of satellite communications, which are characterized by long-distances and narrowband signals. The distance between the satellite and the receiving module leads to weak received signals and, thus, special care is usually devoted to the reduction of possible noise sources. On the other hand, horn antennas typically operate in a frequency range bounded by the cut-off frequencies of the fundamental and the first higher order mode, respectively. Such a frequency range is usually much larger than the signal bandwidth. Therefore, additional components to clean the out-of-band noise are usually needed. The introduction of such components, however, make the receiving system more bulky, heavy, and expensive.

In order to satisfy the aforementioned requirements, I present an innovative design of a horn antenna capable of self-filtering the out-of-band noise contribution by the means of the integration of the metamaterial-inspired filtering module presented in the previous section. At and around the resonant frequency of the omegas, the signal is transmitted through the slit, while the remaining frequencies are reflected back.

The proposed idea is verified through proper full-wave numerical simulations and experimental results.

2.5.1 Overview of the aperture antenna

Exploiting the concept introduced in the previous section, I present a new horn antenna setup, which allows filtering out the broadband noise and receive only a narrowband signal. The proposed configuration is sketched in . The connected bi-omega particle, placed across a slit on a metallic screen inserted between two sections of a WR-62 waveguide, exhibits an odd mode resonant frequency at around 12.6 GHz, whereas the even mode resonant frequency is below the cut-off frequency of the waveguide. The screen is modeled as a 1 mm thick copper plate, with the same transverse dimensions of the WR-62 waveguide. The transverse dimensions of the vertical slit drilled at the centre

the screen are 2 mm x 4.5 mm. The center of the slab is aligned to the center of the screen in such a way that half of the connected bi-omega particle is in the first section of the waveguide and half in the second section. All the metallizations printed on the slab are assumed to be made of copper with thickness of 35 µm.
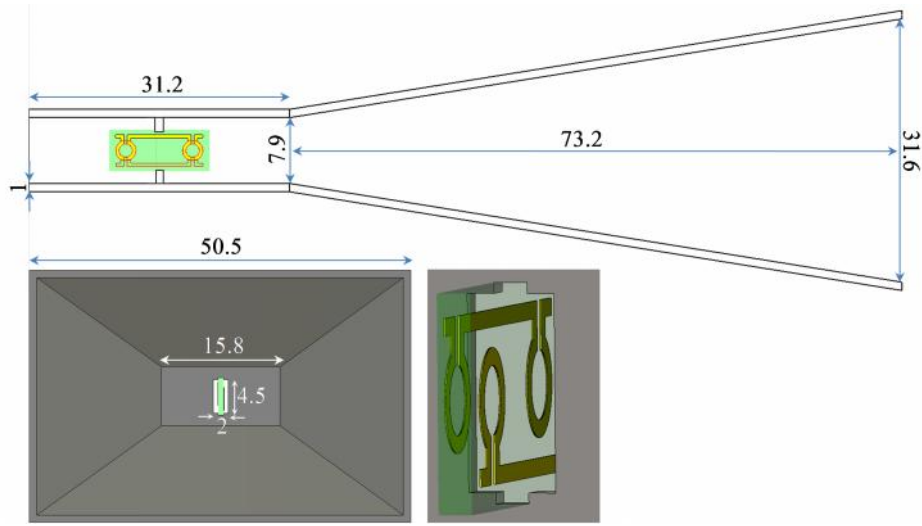
Fig. 33: (up) Longitudinal section and (down-left) front-view of the new proposed horn antenna. The dimensions are in mm. (down-right) Zoom to show how the attachment between the slab and the screen is realized

The connected bi-omega particle, exhibiting an odd mode resonant frequency at around 12.6 GHz, is placed across a slit on a metallic screen inserted between two sections of a WR-62 waveguide (please, note that the even mode resonant frequency is below the cut-off frequency of the waveguide). The screen is modeled as a 1 mm thick copper plate, with the same transverse dimensions of the WR-62 waveguide. The transverse dimensions of the vertical slit drilled at the center of the screen are 2 mm x 4.5 mm. The center of the slab is aligned to the center of the screen in such a way that half of the connected bi-omega particle is in the first section of the waveguide and half in the second section. All the metallizations printed on the slab are assumed to be made of copper with thickness of 35 µm.

In order to test experimentally the proposed antenna layout, I have fabricated a working prototype by modifying the standard WR-62 horn (Flann 18240-15) shown in Fig. 34. The horn antenna is connected to one end of a straight section of a WR-62 waveguide having the other end connected to a coaxial-to-waveguide transition.

Between the waveguide and the horn, I have inserted a 1 mm thick sample holder, which has been filled up with a copper plate, where we have drilled a vertical rectangular slit. The drilled screen has been produced by using the LPKF Protomat-S milling machine, which has also been used to fabricate the sample of the connected bi-omega particle with the same geometrical and electrical parameters reported in Fig. 33 (Fig. 34b).

(a)   *(b)*
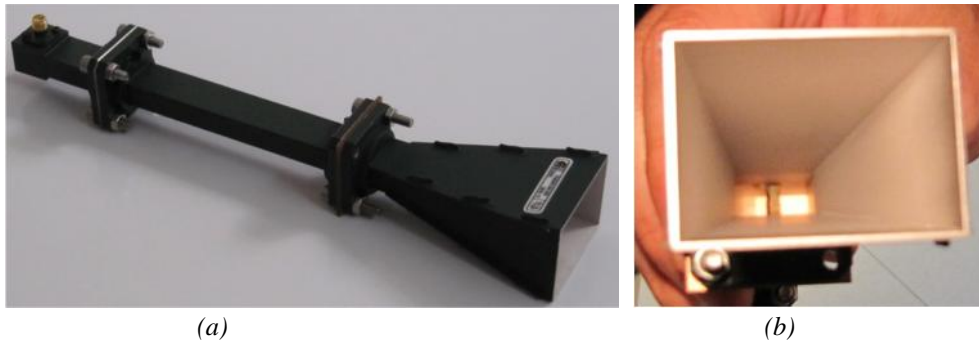
Fig. 34: (a) Regular antenna structure consisting of a coaxial-to-waveguide transition, a straight section of a WR-62 waveguide, and a WR-62 horn. (b) Fabricated antenna with filtering element inside.

2.5.2 Electrical and radiating performaces

The matching properties of the horn, measured by using the Rohde & Schwarz ZVB14 vector network analyzer (VNA) after a proper calibration procedure, are reported in Fig. 35 and compared to the ones obtained by a full-wave numerical simulation [24]. The measured realized gain is reported in . The obtained results are both consistent with the ones resulting from the numerical simulations and confirm the validity of the proposed approach.

As expected, the horn antenna is matched to the port impedance only in a narrow frequency band around the resonant frequency of the connected bi-omega particle (12.6 GHz). The comparison between the matching properties of the regular horn antenna and the ones of the horn with the inserted metamaterial-inspired filtering element clearly shows the particle effect and the achieved self-filtering properties of the new antenna. Radiation properties have been also simulated and compared to the ones of a regular horn with the same dimensions without the connected bi-omega particle. The results concerning the realized gain are shown in Fig. 36. As expected, within a narrow

frequency band around 12.6 GHz, the radiating properties of the two antennas are almost identical, while the new proposed radiator does not operate so efficiently at the remaining frequencies.
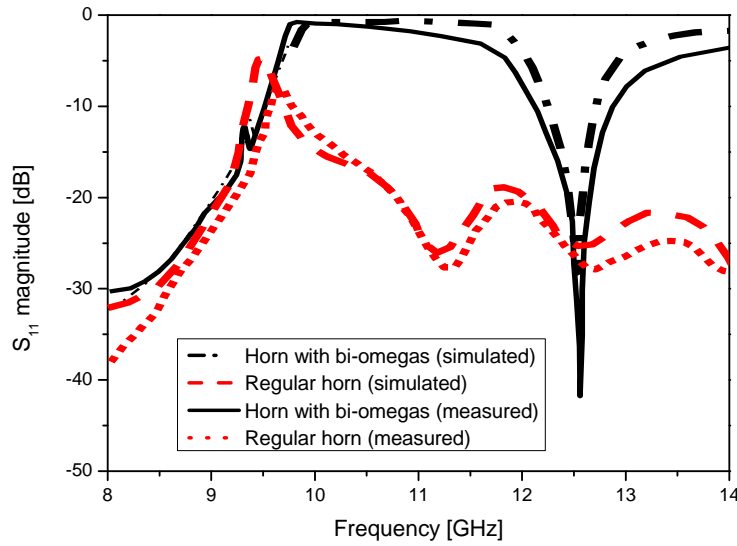
Fig. 35. Simulated and measured matching properties of the WR-62 regular horn antenna and of the WR-62 horn with the insertion of the connected bi-omega particle of Figure 1
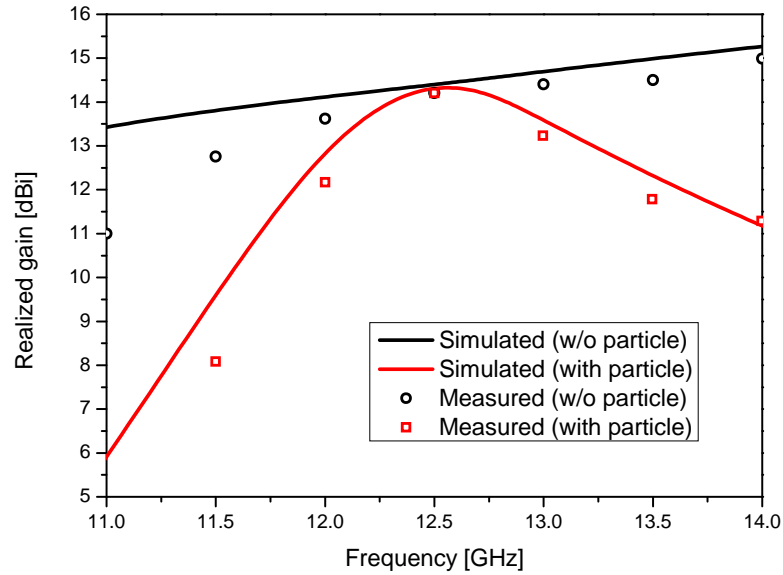
Fig. 36: Simulated and measured realized gain of the WR-62 regular horn antenna and of the WR-62 horn with the insertion of the filter element.

2.5.3 Conclusions

The presented self-filtering horn antenna design exhibits appealing performances for satellite system as well as for any antenna system where a compact low-noise antenna is required. The numerical simulation, and the experimental realization of an innovative self-filtering low-noise horn antenna shows its ability to filter the received signal The proposed radiator consists of a WR-62 waveguide connected to a regular WR-62 horn antenna with inserted the metamaterial-inspired filtering element.

I, first, have designed a connected bi-omega particle, whose odd mode resonates at 12.6 GHz. Then, I have numerically and experimentally demonstrated that by placing such a particle at the throat of a regular WR-62 horn radiator it is possible to reduce the antenna operation bandwidth, allowing power transmission only in a limited frequency band centered around the resonant frequency of the connected bi-omega particle. The proposed setup, thus, can be successfully used to reduce the amount of noise captured by a regular horn in receiving modules of satellite communication systems, where the signal bandwidth is usually narrower compared to the horn operation frequency range. It is worth noticing that in the reduced frequency band of operation, the new proposed horn exhibits the same radiating performances of the regular horn and that the filtering properties have been obtained by keeping the same space occupancy with respect to the regular horn. The proposed filtering structure, thus, can be considered as a light and cheap add-on module that can be easily integrated in any existing horn antenna, in order to reduce its operation bandwidth and avoid capturing undesired noise.

2.6 Waveguide power splitters

Here, I present a new family of waveguide power splitters based on the use of connected bi-omega particles. The new layout consists of an H-plane T-junction, whose ports are characterized by the same cross-section. The output ports are both closed with a metallic screen and energy is allowed to pass through by means of a vertical slit drilled in each metallic screen. In order to make transmission efficient, two identical particles, printed on the two faces of a dielectric slab, are placed across the slits. Depending on the design, at the resonant frequencies of the two bi-omega particles, we obtain either balanced or unbalanced power splitting between the two output ports. In addition, we show that by using switches mounted on either or both bi-omega resonators we may obtain a reconfigurable response.

2.6.1 Balanced and unbalanced configurations

The filtering module configuration consisting of a metallic screen with a sub-wavelength aperture in which the connected bi-omega particle in placed across has been employed also to realize new family of compact power splitter. The balanced configuration is shown in Fig. 37. The connected bi-omega particles are placed at the distance t from the metallic wall that closes the input waveguide. This distance should be determined in order to maximize the coupling with the guided electromagnetic field and to guarantee the efficient power transfer from the waveguide 1 to the waveguides 2 and 3.
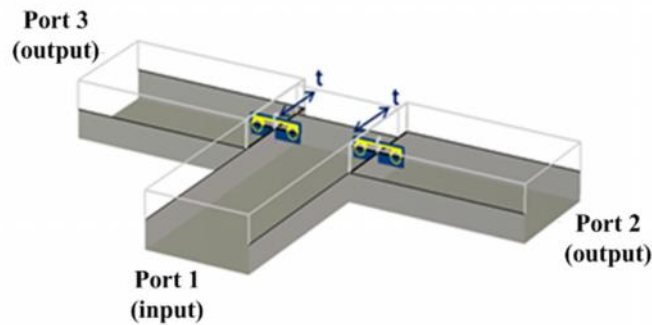
Fig. 37. 3D geometrical sketch of the balanced power splitter.

So, the distance between the bi-omega resonators and the conductive wall at the end of the principal waveguide had to be carefully designed. In fact, the resonators are excited by the magnetic field component orthogonal to the loops. Such a component, however, vanishes on the ending wall of the principal waveguide. Therefore, considering three WR90 waveguides connected via two identical bi-omega particles in order to make the presented configuration a realizable design, I set the distance t to a quarter of the guided wavelength (i.e. $t = 9\ mm$), obtaining the maximum excitation of the loops and, thus, the best performances of the component.

Then, I realize the experimental setup, shown in Fig. 38, where port 1 and port 2 are both connected to the vector network analyzer R&S ZVB-14, while port 3 is terminated with a matched load in order to reduce the reflections as much as possible.
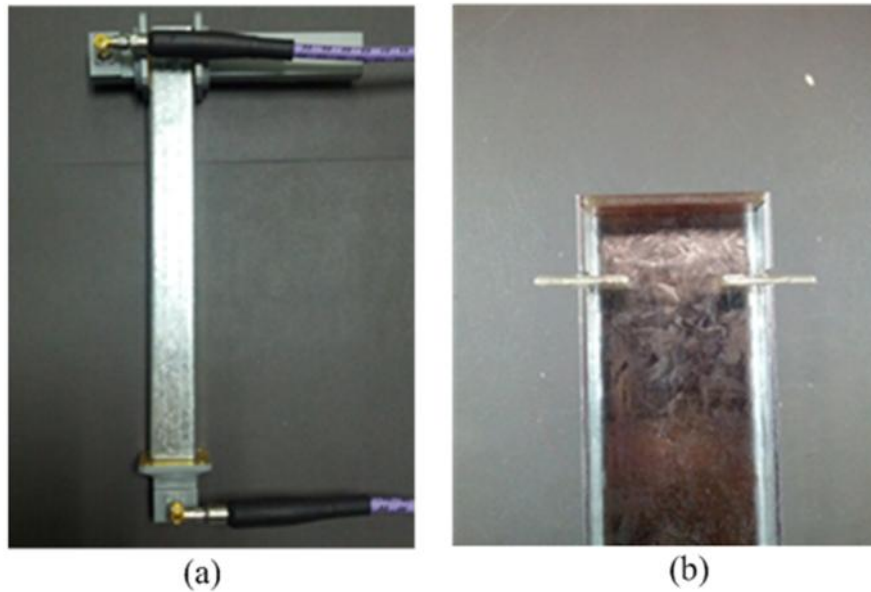
Fig. 38: Top view of the experimental setup: (a) overview and (b) internal view of the power plitter.

The performances of the balanced power splitter has been evaluated numerically by using the full-wave simulator CST [24] and experimentally (Fig. 38). The results shown in Fig. 39 confirm the steadiness of the resonant frequency and the correct operation of the power splitter (perfect power division and impedance matching at the input port).
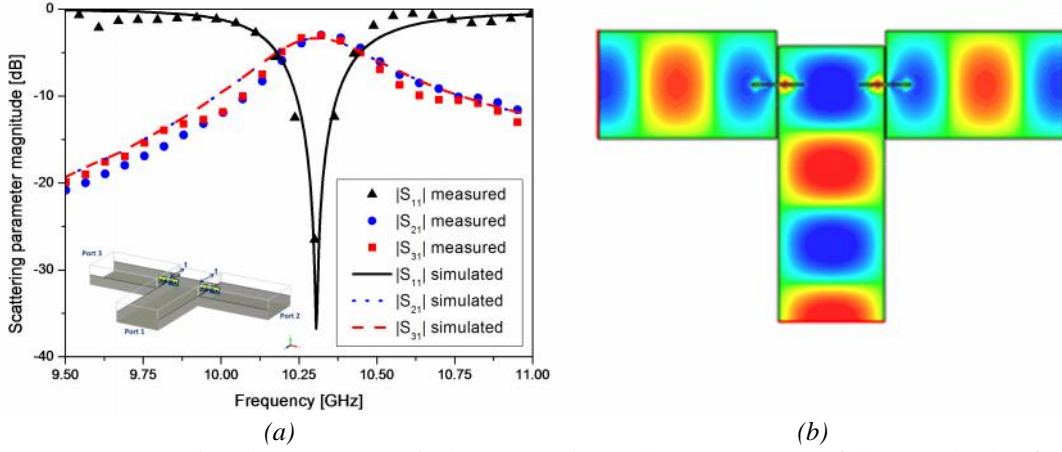
Fig. 39. (a) Comparison between numerical and experimental measurements of the magnitude of the S-parameters of the balanced power splitter. (b) Map of the electric field at the operative frequency of the connected bi-omega particle, i.e. *10.27 GHz*.

Now, if more power needs to be delivered to an output port and less power to the other one, an unbalanced power splitter is required. In order to design such a component, it is possible to start from the fully balanced design shown in Fig. 37 and apply the due changes. As previously anticipated, the distance t between the particles and the ending wall of the principal waveguide plays an important role in the design. One possibility to unbalance the power splitting is to keep t as a quarter of the guided wavelength for the particle at port 2 and shift the particle at port 3 of a length d towards the terminating wall. In this way, since the coupling between the field propagating in the principal waveguide and the particle at port 2 is stronger than the one with the particle at port 3, an increasing of the power transmission at port 2 is expected with respect to the one at port 3.

Also for the unbalanced power slitters, I realize the experimental setup shown in Fig. 40. Port 2 and port 3 are now misaligned in order to reduce the coupling to one of the two ports. The numerical and experimental results are shown in Fig. 41. Return loss is about 25 dB at the design frequency and the transmission coefficient magnitudes are $|S21| = -1.7$ dB and $|S31| = -4.8$ dB, respectively.
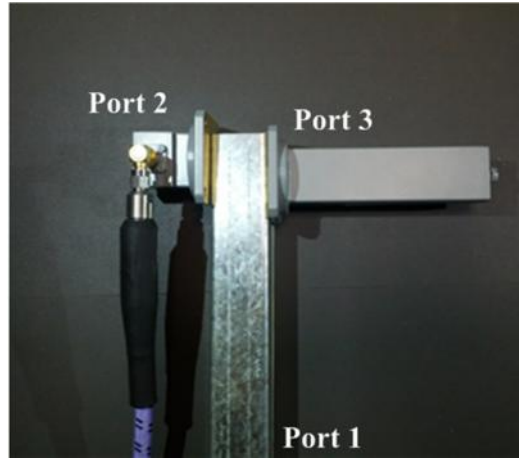
Fig. 40: Top view of the experimental setup for unbalanced power splitter.
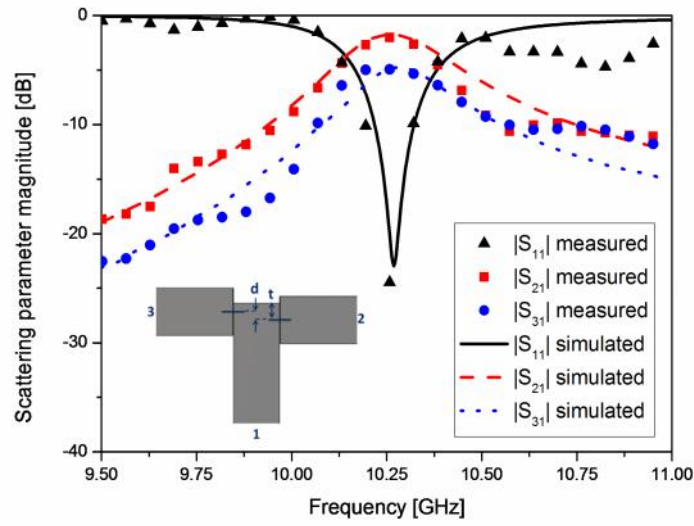
(a)
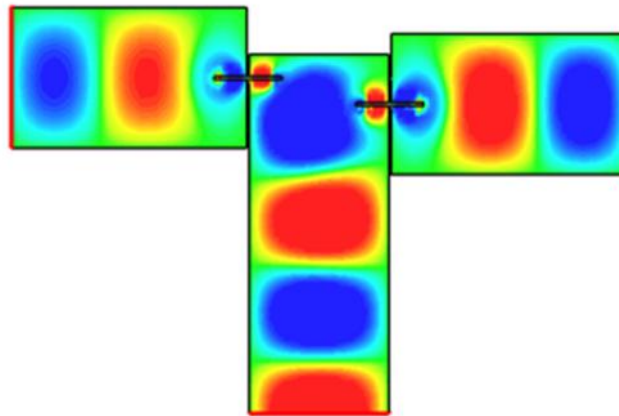
(b)

Fig. 41. (a) Magnitude of the S-parameters of an unbalanced power splitter with a shift *d = 4.3 mm*. In the inset, a top view of the unbalanced power splitter is shown. (b) Map of the electric field at the operative frequency of the connected bi-omega particle, i.e. *10.27 GHz.*

2.6.2 Reconfigurable configuration

Sometimes a real-time control of the amount of power delivered to the two output ports may be needed and, thus, a reconfigurable power splitter is needed. One possibility is to use switches placed across the gaps of one or both the bi-omega particles, in order to control resonant frequency of the connected bi-omega particle.

In the experimental setups here reported, instead of the use of switches, I used two different connected bi-omega particles: one (e.g. the one at Port 3) with the four gaps all short-circuited, and another with a cut between the loop and the dipole of the omega particle. In the both cases, the functionality of the connected bi-omega particle is compromised and the power is not more delivered though the sub-wavelength aperture.

The results shown in Fig. 6 confirm the expected operation of the component.

(a)   *(b)*

(c)
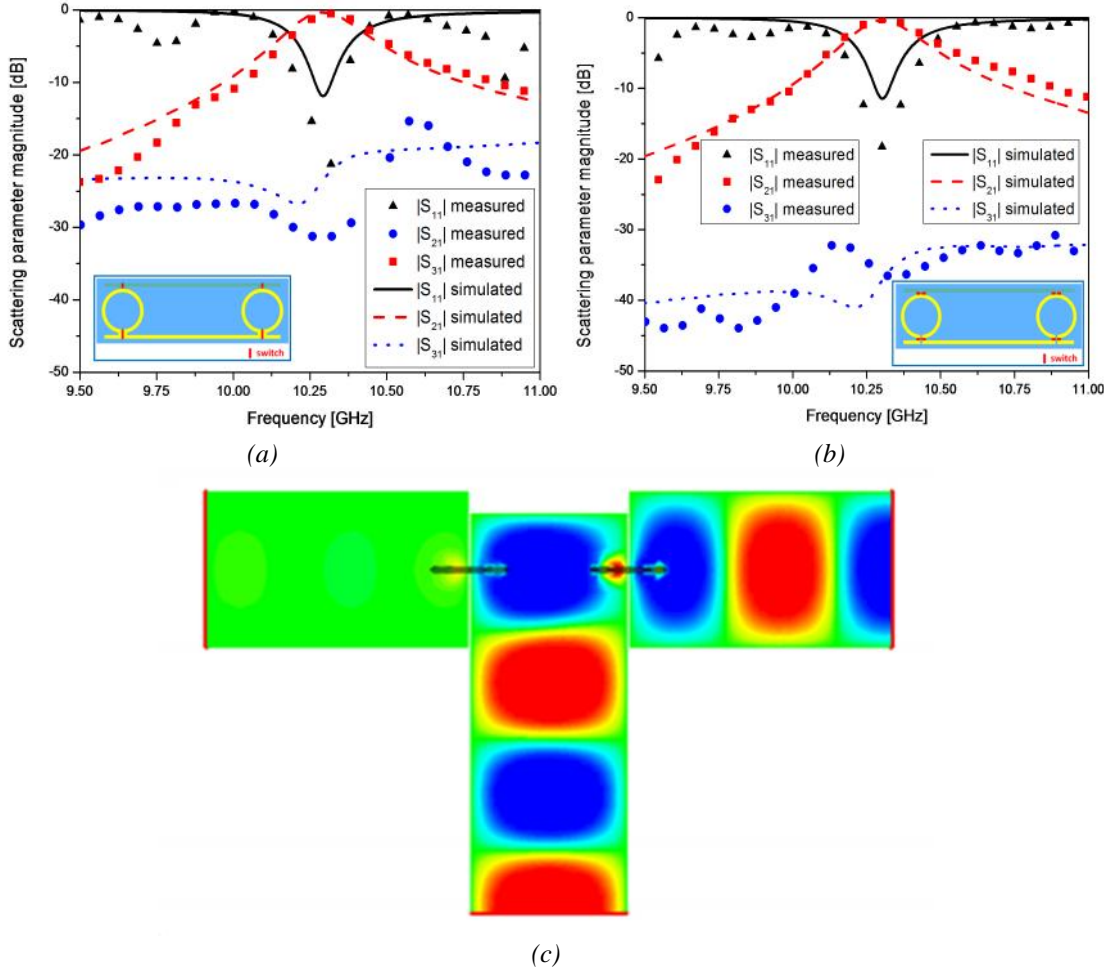
Fig. 42: Magnitude of the S-parameters of the reconfigurable power splitters: (a) the switches are all closed, and (b) the switches are all open. The modified connected bi-omega particle is placed at port 3. (c) Map of the electric field at the operative frequency of the connected bi-omega particle, i.e. *10.27 GHz*.

2.7 References

[1] A. Sihvola, Electromagnetic mixing formulas and applications, IEE Publishing, EM Wave Series, London, 1999.

[2] J. Peng, and R.W. Ziolkowski, "Broadband, efficient, electrically small metmamaterial-inspired anrtennas facilitated by active near-field resonant parasitic elements", IEEE Trans Antennas Propag., Vol. 58, No. 2, pp. 318-327, 2010

[3] J. Peng, and R.W. Ziolkowski, "Multi-frequency, linear and circular polarized, metmaterial-inspired, near-field resoanat parasitic antennas", IEEE Trans Antennas Propag., Vol. 59, No. 5, pp. 1446-1459, 2011.

[4] Z. Ning and R.W. Ziolkowski, "Active metamaterial-inspired broad-bandwidth, efficient , electrically small antennas", IEEE Antennas Propag. Lett., Vol. 10, pp. 1582-1585, 2011.

[5] M. Barbuto, F. Bilotti, and A. Toscano, "Design of a multifunctional SRR-loaded printed monopole antenna" Int. Journ. RF Microw. Computer-Aided Eng., vol.22 No. 4, pp.552-557, 2012.

[6] R. Marqués, F. Mesa, J. Martel, and F. Medina, "Comparative analysis of edge- and broadside-coupled split ring resonators for metamaterial design—Theory and experiment," IEEE Trans. Antennas Propag., vol. 51, no. 10, pp. 2572–2581, Oct. 2003.

[7] F. Bilotti, A. Toscano, and L. Vegni, "Design of Spiral and Multiple Split-Ring Resonators for the Realization of Miniaturized Metamaterial Samples", IEEE Trans. Antennas Propag., Vol. 55, No. 8, pp. 2258-2267, 2007.

[8] J. Huangfu, L. Ran, H. Chen, X. Zhang, K. Chen, T.M. Grzegorczyk, and J.A. Kong, "Experimental confirmation of negative index of a metamaterial composed of -like metallic patterns," Appl. Phys. Lett., Vol. 84, 1537, 2004.

[9] S.A. Tretyakov, C.R. Simovsky, and M. Hudlicka, "Bianisotropic route to the realization and matching of backward-wave metamaterial slab", Phys. Rev. B, Vol. 75, 153104, 2007.

[10] D.E. Grupp, Henri J. Lezec, T. Thio, and, T. W. Ebbesen, "Beyond the Bethe limit: Tunable enhanced light transmission through a single sub-wavelength aperture," Advanced Mat., Vol. 11, pp. 860-862, 1999.

[11] A.A. Oliner and D.R. Jackson, "Leaky surface plasmon theory for dramatically enhanced transmission through a subwavelength aperture, Part I: Basic features," Proc IEEE AP-S Symp. 2003, pp. 1091-1094.

[12] A. Alu, F. Bilotti, N. Engheta, and L. Vegni, "Metamaterial covers over a small aperture," IEEE Trans. Antennas Propagat., Vol 54, pp. 1632-1643, 2006.

[13] A. Alù, F. Bilotti, N. Engheta, L. Vegni, "Sub-wavelength planar leaky-wave components with metamaterial bilayers," IEEE Trans. Antennas Propagat., Vol. 55, pp. 882-891, 2007.

[14] F. Bilotti, L. Scorrano, E. Ozbay, and L. Vegni, "Enhanced transmission through a sub-wavelength aperture: Resonant approaches employing metamaterials," J. Opt. A: Pure Appl. Opt., Vol. 11, 114029, 2009.

[15] K. Aydin, A.O. Cakmak, L. Sahin, Z. Li, F. Bilotti, L. Vegni, and E. Ozbay, "Split ring resonator-coupled enhanced transmission through a single subwavelength aperture," Phys. Rev. Lett., Vol. 102, 013904, 2009.

[16] K.B. Alici, F. Bilotti, L. Vegni, and E. Ozbay, "Optimization and tunability of deep subwavelength resonators for metamaterial applications: complete enhanced transmission through a subwavelength aperture," Opt. Expr., Vol. 17, pp. 5933-5943, 2009.

[17] L. Scorrano, S. Tricarico, F. Bilotti, "Resonating plasmonic particles to achieve power transmission enhancement," IEEE Photon. Technol. Lett., Vol. 22, pp. 938-940, 2010.

[18] L. Scorrano, F. Bilotti, and L. Vegni, "Achieving power transmission enhancement by using nano-rings made of silver spheres," IEEE Photon. Technol. Lett., Vol. 22, pp. 1595-1597, 2010.

[19] D. Ates, A.O. Cakmak, E. Colak, R. Zhao, C.M. Soukoulis, and E. Ozbay, "Transmission enhancement through deep sub-wavelength apertures using connected split-ring resonators," Opt. Expr., Vol. 18, 3952, 2010.

[20] S. A. Tretyakov, F. Mariotte, C. R. Simovski, T. G. Kharina and J. Heliot "Analytical antenna model for chiral scatterers: Comparison with numerical and experimental data," IEEE Trans. Antennas Propagat., Vol. 44, pp. 1006-1014, 1996.

[21] C.R. Simovski, S. A. Tretyakov, and A. A. Sochava "Antenna model for conductive omega particles," J. Electromag. Waves Applicat., Vol. 11, pp. 1509-1530, 1997.

[22] S.A. Schelkunoff, and H.T. Friis, Antennas: Theory and Practice, Bell Telephone Laboratories, Inc., 1952.

[23] S.A. Tretyakov, F. Mariotte, C. R. Simovski, T. G. Kharina and J. Heliot "Analytical antenna model for chiral scatterers: Comparison with numerical and experimental data," IEEE Trans. Antennas Propagat., Vol. 44, pp. 1006-1014, 1996.

[24] CST Studio Suite 2011, CST Computer Simulation Technology, http://www.cst.com.

[25] A.N. Lagarkov, V.N. Semenenko, V.A. Chistyaev, D.E. Ryabov, S.A. Tretyakov, and C.R. Simovski "Resonance properties of bi-helix media at microwaves," Electromag., Vol. 17, pp. 213-237, 1997.

[26] C.A. Balanis, Antenna Theory: Analysis and Design, 3rd ed., John Wiley and Sons: New Jersey, 2005, pp.739–810.

3 ENZ metamaterial lens for novel aperture antennas

In this chapter, I present two novel designs of flat lens, made by a conventional material and an epsilon near-zero (ENZ) metamaterial or by loaded ENZ metamaterial, to plug up the aperture of aperture antennas, in order to achieve new radiation performances.

First, I present a metamaterial lens for shortened aperture antennas that lets to achieve radiating performances similar to the ones of the corresponding optimum horn over a broad frequency range. Lens operation is based on the phase-compensation concept: phase-fronts of the field propagating along the short flare of the horn propagate with different phase velocities in the two lens materials, resulting in an uniform phase distribution on the aperture. A realistic version of the lens, realized with a wire-medium and exhibiting a near-zero real part of the effective permittivity in the frequency range of interest, is presented. Considering two examples working in the C-band, we show that the lens can be designed for both conical and pyramidal horn antennas. In both cases, the length of the horns is half the one of the corresponding optimum versions, while the obtained radiation performances are similar to those of the optimum horns over a broad frequency band.

Then, I present the numerical results of an aperture horn antenna with steerable radiation diagram. The rotation of the maximum of the radiation diagram is obtained modifying locally the index of refraction of the ENZ lens in order to change locally the electrical path inside the lens.

3.1 Introduction

In the last decade, a new class of artificial materials, i.e. metamaterials, has been widely investigated. Metamaterials exhibit anomalous values of relative permittivity and permeability, e.g. negative or low-positive (i.e. less than 1) values, within a frequency range of interest (e.g. microwave frequencies) [1]–[7]. A microwave metamaterial typically consists of a dense array of electrically small metallic particles embedded in a host medium. According to the homogenization constraints [8], such an artificial material can be described in terms of effective relative permittivity and permeability. For instance, in order to obtain negative values of the effective permittivity, the host material can be filled up with thin conducting rods [9]-[10], whereas negative values of the permeability can be obtained by using an array of split–ring resonators [2]–[4], [11]. The design of the particles allows tailoring the effective properties of the metamaterials, resulting in the design of devices and components with enhanced performances with respect to the conventional ones [12]–[19].

Among the different metamaterials, low–index materials, epsilon near–zero (ENZ), and mu near–zero (MNZ) metamaterials, have been widely investigated, due to their intriguing properties. For instance, propagation through a low-index material results in a phase–shift of the propagating field much lower than the one in free-space [20]. Moreover, in [21]-[22] transmission and reflection properties of low–index, ENZ, and MNZ slabs have been presented, showing how such structures can work as spatial filters for a given polarization. The aforementioned electromagnetic properties have been exploited in several different contexts and applications. In [23], for instance, a slab of either ENZ or MNZ material placed in front of a sub–wavelength hole has been used to enhance the transmission through the aperture. Novel waveguide components with sharp bends [24] and compact matched adapters [25] have been also demonstrated. Moreover, as far as antennas are concerned, it has been shown that covering the surface of a printed antenna with a low–index slab leads to an enhancement of the directivity [26]–[29].

In modern radar and satellite systems, microwave antennas with high-directivity and steerable radiation diagram are required for tracking, space, and remote sensing

applications [30]. A common radiator used for achieving high gains is the horn antenna, exhibiting good bandwidth performances and radiation efficiency. The gain of a horn antenna is inherently related to its physical dimensions, and, thus, high gain horns are typically heavy and rather bulky components [31]-[33]. On the contrary, in order to steer a beam into a desired direction typically a phased-arrayed antennas are used. The beam tilt is obtained by imposing electrical phase differences between the antenna elements, in such a way that a constructive interference of the fields radiated by each antenna element is achieved in the desired direction [34]. Moreover, in order to achieve high gain antenna system, typically several antenna elements are employed, increasing the complexity of the system. Although a single aperture antenna, e.g. an horn antenna, may be successfully employed to achieve in the same time high-gain and simply antenna systems [31]-[33], the steering of the main beam is nowadays given only to mechanical tilt system of the antenna that directs the aperture towards the desired direction.

The availability of compact horn antennas with gain performances comparable to the ones of regular and even optimum horns or aperture antennas with electronic steerable main lobe would represent a remarkable achievement in the field.

3.2 Broadband compact horn antennas

In the open technical literature, the first attempts to reduce the physical dimensions of a horn antenna have been proposed in [35]–[39], where pyramidal horns have been loaded with an ENZ metamaterial implemented through a proper wire–medium. In that case, however, horn directivity has been effectively increased but, due to the inherent dispersion of the wire-medium effective permittivity (i.e. following Drude dispersion [40]), the directivity enhancement was observed only in a narrow frequency band. In [41] a comparative study based on measurements and simulations of conical horns with an inserted metallic cone-sphere, with an integrated dielectric lens and with a flat ENZ metamaterial lens has been reported, showing that the radiating performances of the horn with the ENZ flat lens are on average worse than those ones of the other two loaded horns in the mono–modal frequency band.

Here I propose a new approach to use ENZ metamaterials to enhance the directivity of horn antennas over a broad frequency range. To this end, I propose a new flat lens to be placed at the aperture of the horn consisting of an inner part made by a conventional (i.e. epsilon positive, EPS) material and an outer part made by an ENZ metamaterial. Lens operation is based on the phase-compensation concept: the portion of the field propagating along the axis of the horn interacts only with the EPS material of the lens, while the portion of the field close to the horn plates interacts with the ENZ metamaterial. If the two materials of the lens and their thickness are properly chosen, we show that the phase-front of the field after the lens is uniform, leading to an enhancement of the directivity, though the horn is rather short. Starting from the theoretical study of the transmission properties through a bulk ENZ slab, I derive the formulas for the design of the flat lens and validate them by the means of proper full–wave numerical simulations.

3.2.1 Theory and design of EPS-ENZ lens

I start the study of ENZ material considering a planar slab with permittivity ε_{ENZ}, permeability μ_0, and thickness d_{ENZ}, infinitely extended along x– and y–directions (Fig. 43). The slab is illuminated by a normally incident plane–wave propagating in free–space towards the positive direction of the z–axis.
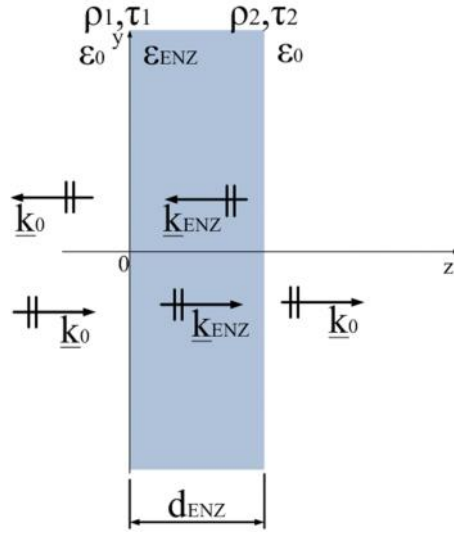
Fig. 43. A planar slab made of an ENZ material excited from the left side by a normally incident plane-wave.

Assuming that the magnetic field is linearly polarized along the x–axis, the transmission coefficient T is [30]:

$$T = \frac{\tau_1 \tau_2 e^{-jk_{ENZ}d_{ENZ}}}{1 + \rho_1 \rho_2 e^{-2jk_{ENZ}d_{ENZ}}} \tag{42}$$

where $k_{ENZ} = \omega\sqrt{\varepsilon_{ENZ}\mu_0}$ and $\rho_1, \tau_1, \rho_2, \tau_2$ are the reflection and transmission coefficients at $z = 0$ and $z = d_{ENZ}$, respectively.

In Fig. 44, I report the phase of the transmission coefficient T as a function of the electrical thickness of the slab d_{ENZ}/λ_0 for different values of ε_{ENZ}. As expected, the phase–shift is much lower in the ENZ slab with respect to free–space for the same propagation distance. Therefore, the electromagnetic field travels with a higher phase–

velocity inside the ENZ slab. This property will be exploited in the following to compensate the bending of the phase–fronts of the field propagating along the edges of an horn antenna.
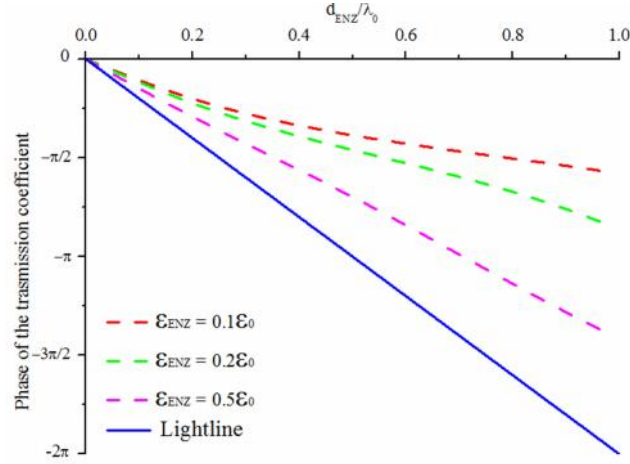
Fig. 44: Phase of the transmission coefficient through a planar ENZ slab for different values of ε_{ENZ} as a function of the electrical thickness d_{ENZ}/λ_0 .

I consider now a regular horn antenna designed to exhibit the desired radiating performances in a given frequency band. As a particular case, I can consider the optimum horn, exhibiting the maximum gain in the broadside direction for a given aperture dimension. Typically, the design formulas for regular optimum horns return the minimum length and aperture dimensions to reach the desired gain value. Formulas for pyramidal and conical horns are widely reported in textbooks [30]–[33].

The geometrical sketches of an optimum horn and its corresponding shortened version loaded with the EPS–ENZ lens are shown in Fig. 45. The compact horn has the same aperture dimensions and is fed by the same waveguide as the optimum horn, but its length is shorter. As shown in Fig. 45, the EPS–ENZ lens placed at the aperture of the antenna (the lens is placed inside the horn) is geometrically characterized by the thickness d_L and the aperture dimension A_L . Such dimensions have to be properly designed, in order to assure an uniform phase distribution on the aperture at $z'=0$, similar to the one of the optimum horn.
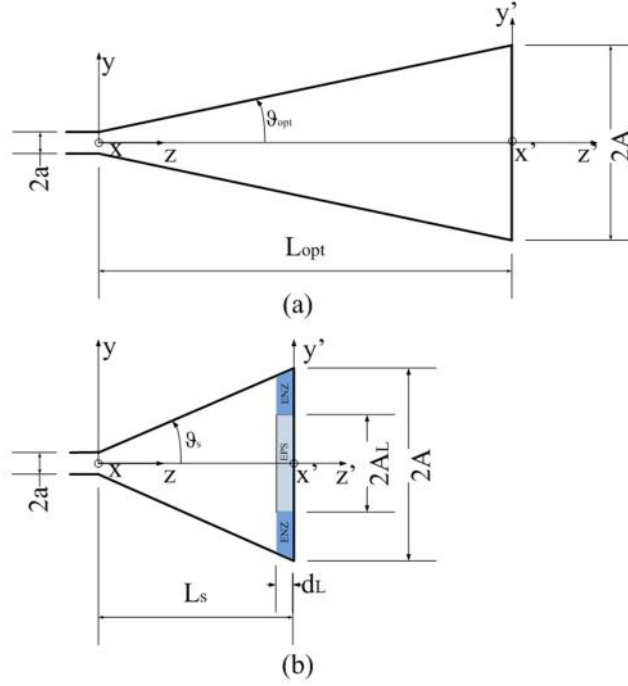
Fig. 45: Geometrical sketch of (a) an optimum horn and (b) the shortened horn loaded with the EPS/ENZ lens.

In order to evaluate the geometrical dimensions of the lens, we consider one of the two principal planes of the horn, i.e. either the E– or the H–plane, at a time. The design procedure consists of applying the design formulas twice, one for each of the two planes. In order to evaluate the phase distribution at the aperture of the optimum and of the lens–loaded short horns we assume, for the moment, that both ENZ and EPS materials are perfectly matched at both interfaces with the free–space. In this way, we may focus our attention on the phase distribution only. We will relax this constraint later. The mode guided by the horn is characterized by a curved phase–front and for each point of the aperture we can evaluate the phase value φ, which depends on the length of the horn and on the distance of the point from the axis of the horn. Considering the coordinate systems of Fig. 45, the phase φ can be written as follows:

$$\varphi(y',L)=\frac{k_0 A}{A-a}L\left(1-\sqrt{1+\frac{y'^2}{\left(\frac{A}{A-a}\right)^2 L^2}}\right) \tag{43}$$

where L is the length of the horn antenna: $L = L_{opt}$ for the optimum horn and $L = L_s$ for the short horn. If $L_s = \alpha L_{opt}$, the value α (with $\alpha < 1$) represents the length reduction. Since the aperture dimensions are the same for both antennas, the shortened horn is characterized by a flare angle $\vartheta_s > \vartheta_{opt}$, which leads to an higher phase value φ for the field close to the plates ($y' = A$) than in the case of the full–length horn. The phase–fronts, thus, are expected to be more curved than in the optimum case. The presence of the ENZ material at the horn edges allows, thus, compensating the relative phase differences at the aperture of the shortened horn. The thickness d_L of the lens is designed such that the shortened and the optimum horn exhibit the same phase φ at the edge of horn. Assuming that the lens materials are lossless and that the permittivity ε_{EPS} and ε_{ENZ} are set by the designer, the thickness d_L must satisfy the following identity:

$$\left[\varphi\left(y' = A, L = L_s \right) + \mathrm{Arg}\left[T\left(d_L \right) \right] \right] - \left[\varphi\left(y' = 0, L = L_s \right) - k_{EPS} d_L \right] =$$
$$\varphi\left(y' = A, L = L_{opt} \right) - \varphi\left(y' = 0, L = L_{opt} \right) \tag{44}$$

where $k_{EPS} = \omega \sqrt{\varepsilon_{EPS} \mu_0}$. The left–hand side of eq. (44) represents the new phase difference between the edge $\left(y' = A \right)$ and the center $\left(y' = 0 \right)$ of the aperture of the shortened horn when the lens of thickness d_L is present. The right-hand side, instead, represents the same phase difference evaluated for the optimum horn.

Once the thickness of the lens is determined, we need to derive the aperture dimension A_L of the lens. This quantity can be obtained imposing that the maximum value of the phase allowed at $y' = A_L$ (before the lens) is at least equal to the phase at the edge of the optimum horn. When such a phase-front travels through the lens, the portion of the field propagating inside the EPS material experiences the same phase–shift as in the case of the optimum horn, while the portion of the field propagating through the ENZ material experiences the same phase–shift as at the one at the edge of the optimum horn. Thus, the design formula reads:

$$\varphi\left(y'=A_L, L=L_s-d_L\right)=\varphi\left(y'=A, L=L_{opt}\right) \tag{45}$$

3.2.2 Proof of concept: numerical simulations

Here, I report on the numerical validation of the design formulas (44), (45), by simulating the antenna performances using CST Microwave Studio [42]. Let us consider first a horn antenna with the following electrical dimensions: $L_{opt}=10\lambda_0$, $A=3\lambda_0$, $a=0.3\lambda_0$, where λ_0 is the wavelength at the frequency f_0 at which we desire the maximum gain. Such an antenna will be considered as the reference one. In , we plot the electric field phase map on the E–plane.
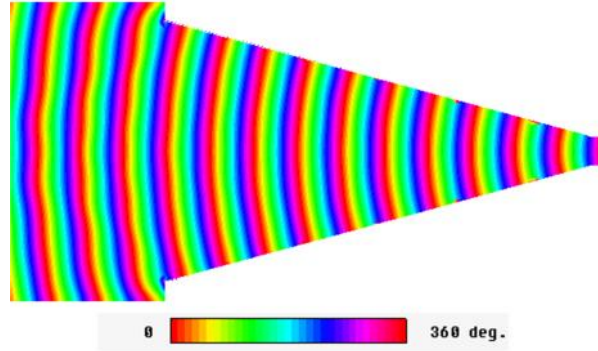
Fig. 46: Electric field phase map at the design frequency f_0 of the reference horn antenna.

As expected, the phase of the electromagnetic field at the aperture is rather uniform and, consequently, an high gain is achieved. In order to test the design formulas (44), (45), I consider three different shortened horn antennas with length $L_s=\alpha L_{opt}$, where r is 0.6, 0.5, 0.4, respectively. Assuming the lens made by lossless ideal materials and setting the EPS and ENZ permittivity to $\varepsilon_{ENZ}=0.1\varepsilon_0$ and $\varepsilon_{EPS}=\varepsilon_0$, I use the formulas to design the proper lens for each of the shortened horns. Applying eqs. (44), (45), the following values for the thickness and the aperture dimension of the lens are obtained: $d_L=(0.41,\ 0.55,\ 0.74)\lambda_0$, and $A_L=(2.41,\ 2.21,\ 1.7)\lambda_0$ for $=(0.6,\ 0.5,\ 0.4)$, respectively.

In Fig. 47, Fig. 48, Fig. 49, I report the electric field phase maps at the design frequency with and without the EPS–ENZ lens.

(a)   *(b)*
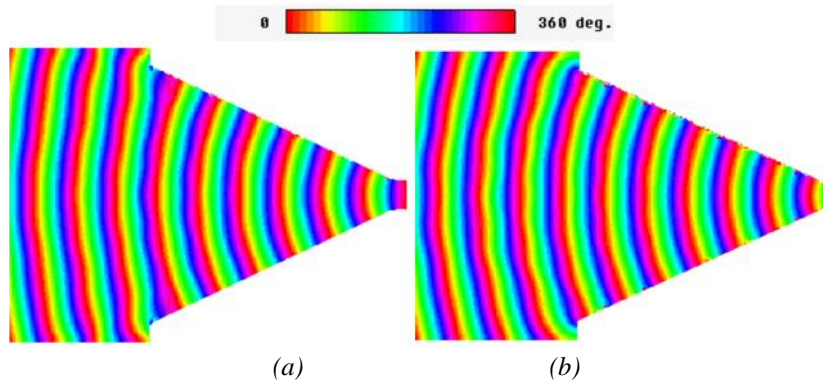
Fig. 47: Electric field phase map at the design frequency f_0 for a shortened horn with length $L_s = 0.6L_{opt}$ (a) without and (b) with the EPS–ENZ lens.

(a)   *(b)*
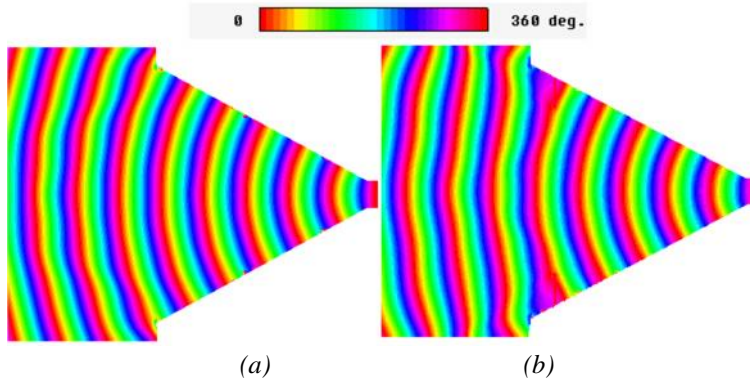
Fig. 48: Electric field phase map at the design frequency f_0 for a shortened horn with length $L_s = 0.5L_{opt}$ (a) without and (b) with the EPS-ENZ lens.

(a)   *(b)*
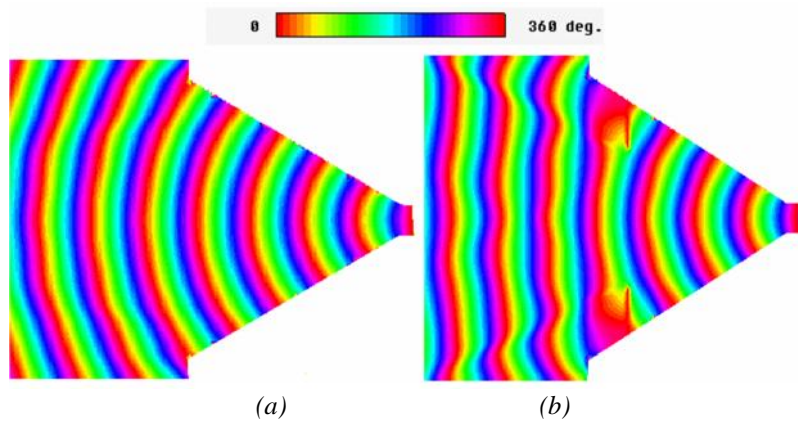
Fig. 49: Electric field phase map at the design frequency f_0 for a shortened horn with length $L_s = 0.4L_{opt}$ (a) without and (b) with the EPS-ENZ lens.

In this first verification of the proposed layout, I have considered the ENZ metamaterial as an ideal isotropic material. In the following I consider its actual implementation through a proper wire-medium.

3.2.3 Design of realistic ENZ-EPS lens

In order to design a realistic lens, the ENZ medium has been implemented through a proper wire–medium (WM) consisting of a dense periodic array of conducting wires aligned parallel to the impinging electric field vector. Two wire arrangements, placed one orthogonal to the other, create the crossed configuration shown in Fig. 50, which is commonly employed in the case of circular–polarized impinging fields. In order to make the simulation faster, the wires have been considered with squared cross–section.

As a first order approximation useful for the initial design of the lens, the real and imaginary parts of the effective permittivity of the WM can be estimated by using the retrieval methods proposed in [43],[44], which make use of the complex transmission/reflection coefficients, evaluated when the structure is illuminated by a normally impinging plane–wave on the WM–air interface. Of course, this first order model of the WM permittivity function can be further improved by using the formulation reported in [45], but this leads to more complex investigations, which are out of the scope of the present paper. However, we will show in the following that the simplified model of the WM based on reflection/transmission data leads, anyway, to reasonable results and can be considered as a good starting point for the actual implementation of the lens.
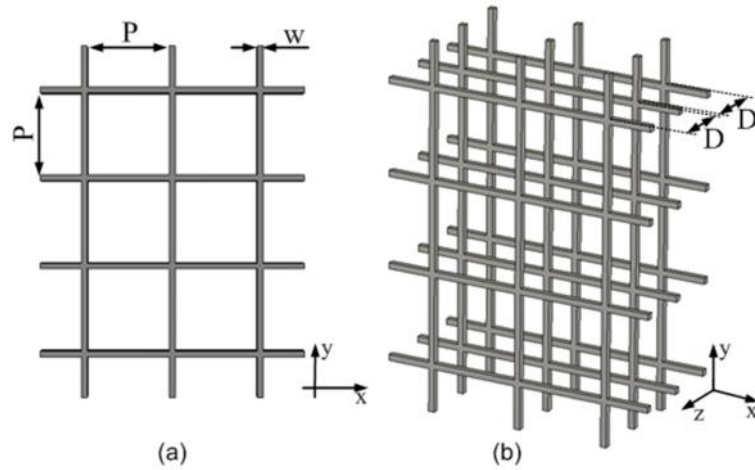
Fig. 50: Wire-medium composed by three grids of crossed metal wires:(a) front view; (b) prospective view.

The periodicity P in the x-y plane, the thickness of the wires w, and the periodicity D in the z–direction, i.e. the distance between two adjacent grids, have been numerically optimized in order to obtain the desired ENZ behavior and the maximum amplitude of the transmission coefficient in the frequency band of interest. As an example, in Fig. 51 the retrieved complex effective permittivity function of the crossed WM for given electrical dimensions of the geometrical parameters is shown. In this simulation, wires are assumed to be made of copper and conduction losses, thus, have been fully taken into account.
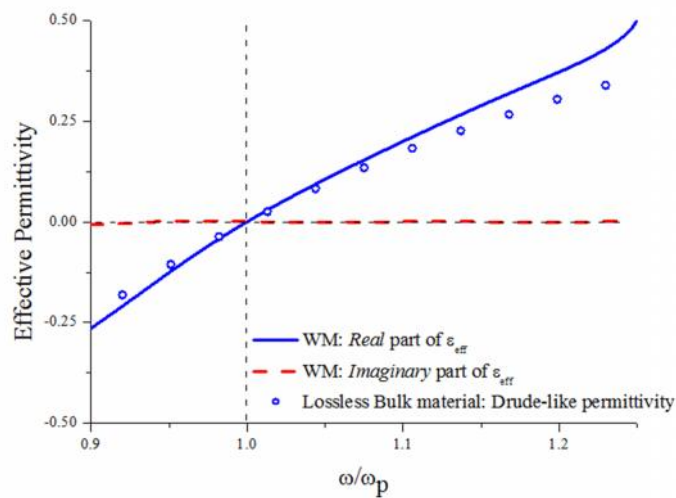
Fig. 51: Retrieved complex effective permittivity of a copper WM with $D = 0.27\lambda_p$, $P = 0.43\lambda_p$, $w = 0.03\lambda_p$ as a function of the normalized angular frequency compared to the Drude–like dispersion.

In Fig. 51, the real part of the retrieved permittivity is compared to the one resulting from a Drude–like dispersion model:

$$\varepsilon_r(\omega) = 1 - \frac{\omega_p^2}{\omega^2} \tag{46}$$

showing a rather good agreement around the plasma frequency in the range $[1.0;1.2]\omega_p$, which, as it will be shown later, can coincide with the mono–modal frequency range of the waveguide feeding the horn. On the contrary, as expected, the imaginary part of the effective permittivity is almost vanishing, leading to negligible losses, typical of a non-resonating structure.

Before continuing, I would remark that, although the dispersive behavior of the ENZ metamaterial is usually considered as an undesired effect, in this case, however, it is necessary to obtain the operation of the short horn over a broad frequency range. In Fig. 44, the difference between the curves for $\varepsilon_{ENZ} < \varepsilon_0$ and the light line represents the phase gain experienced by the field when propagating though the ENZ part of the lens with respect to the EPS part (e.g. just air). Consider for the moment that at a certain frequency the electrical thickness of the lens is 0.1 and the effective permittivity of the WM is $0.1\varepsilon_0$, resulting in a given phase gain experienced by the field. Now, when increasing the frequency, the effective permittivity increases, as well, due to the Drude–like dispersion of the WM, but the lens becomes electrically thicker. The field, thus, propagates longer in the ENZ material and the phase gain remains quite constant over a broad frequency range.

In the following, I show two examples of realistic implementations of the EPS–ENZ lens for a conical and a pyramidal horn, respectively. In both cases, the horn lengths are set as *half* of the length of the optimum horn. First, I consider the case of the conical horn. Following the work by King [46], the optimum conical horn having a broadside gain of *23 dBi* at *6 GHz* is characterized by an aperture diameter $2R = 294\,mm$ and a length $L_{opt} = 490\,mm$. The horn is fed by a circular waveguide with diameter $2r = 32\,mm$, whose cut-off frequency is *5.5 GHz*. The optimum conical horn is shown in a.

The shortened version of the optimum conical horn, whose length L_s is 50% shorter than the one of the optimum case (Fig. 10b), has been obtained by loading it with the EPS–ENZ lens. For the EPS medium we have used just air, while the ENZ annular part of the lens is made by a crossed WM. The lens has been designed to work at *6 GHz,* where it is assumed that the effective relative permittivity of the ENZ material is 0.1. Then, by using eqs. (44), (45), I have evaluated the diameter $2R_L$ and the thickness d_L of the lens as *160 mm* and *29 mm,* respectively. Also the WM needs to be properly designed, satisfying the following constraints: the plasma frequency is set at $f_p = 5.5\,GHz$ and the thickness d_{ENZ} coincides with d_L. According to the previous considerations about the WM, the ENZ frequency band extends from the plasma frequency up to about $7\,GHz$, which corresponds to the boundary of the monomodal frequency band of the feeding circular waveguide.

(a) *(b)*
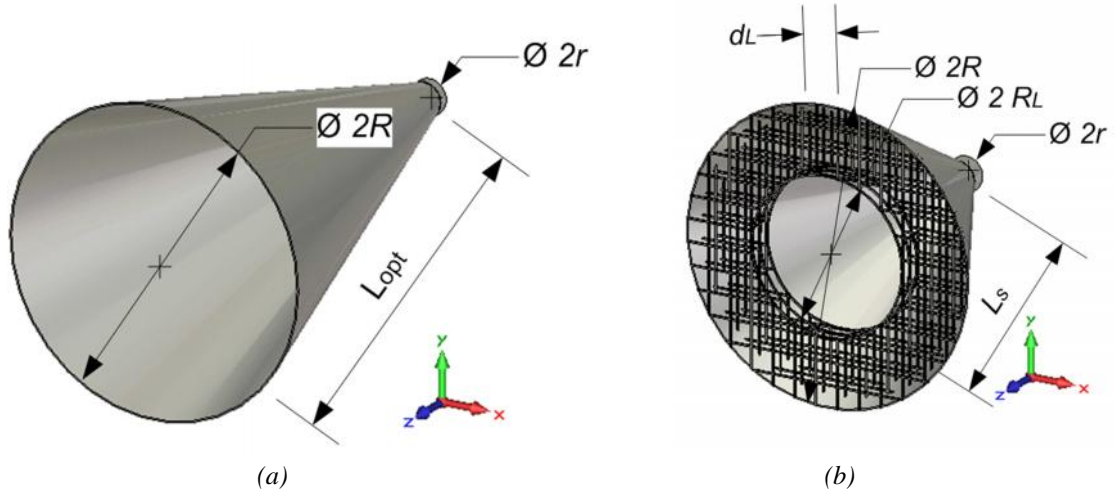
Fig. 52: Prospective view of (a) the optimum conical horn with length L_{opt} and (b) the shortened conical horn with length L_s.

I report the numerical results, obtained by the simulation, of the performances of four conical horns: the optimum one and the shortened one *without* any lens, with *full-ENZ* lens, as in [35]–[39], and with the proposed *EPS–ENZ lens*. In order to increase the reliability of the reported numerical results, we have used two different full-wave simulators that implement two different numerical techniques: CST Microwave Studio

(*Finite Integral Technique*) [42] and Empire XCcel (*Finite-Difference Time-Domain*) [47]. The first one has been used to simulate all the structures under study, whereas the second one as a countercheck for the evaluation of the performances of the shortened horns in presence of the proposed EPS-ENZ lens. The two full-wave simulators give very similar results in terms of radiation diagrams and matching properties.

In Fig. 53, I report the broadside gain as a function of the frequency of the four horn antennas. The broadside gain of the optimum horn and of the shortened one with the EPS–ENZ lens are rather close, confirming that the proposed lens effectively increases the gain of the short horn over the entire monomodal frequency band of the feeding waveguide. In particular, at *6.20 GHz* the shortened horn exhibits the same gain of the optimum one. It is possible to note here that in the case of the shortened horn loaded with a full–ENZ lens (i.e. the solution proposed in [35]–[39]) the gain is comparable to the one of the optimum horn only in a narrow band close to the plasma frequency of the WM, where it effectively acts as spatial filter. In Fig. 54, we report the radiation pattern at *6.20 GHz* of the optimum horn and of the shortened one with and without the lens. The optimum and the proposed shortened horns with the EPS-ENZ lens exhibit the same beamwidth and the same values of the realized gain. Moreover, despite the presence of the WM lens, the side-lobe level is lower than *-20 dB* on both planes.
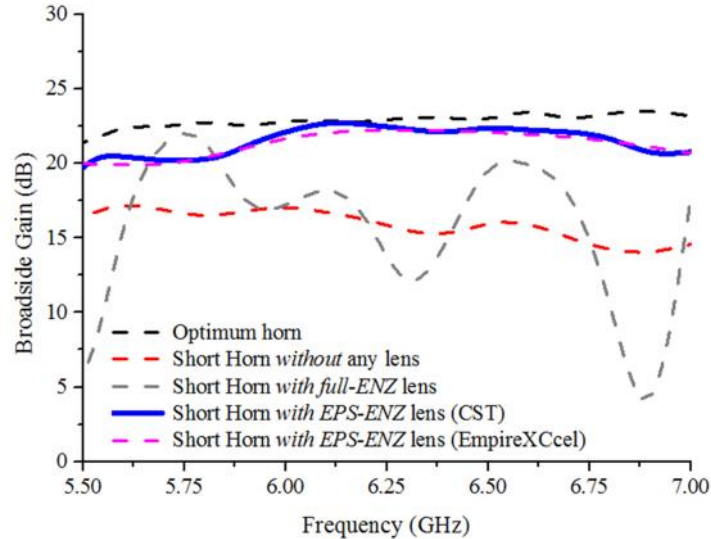
Fig. 53: Comparison between the broadside gain of the optimum conical horn and of the shortened versions without any lens, with full-ENZ lens and with EPS–ENZ lens.

(a) *(b)*
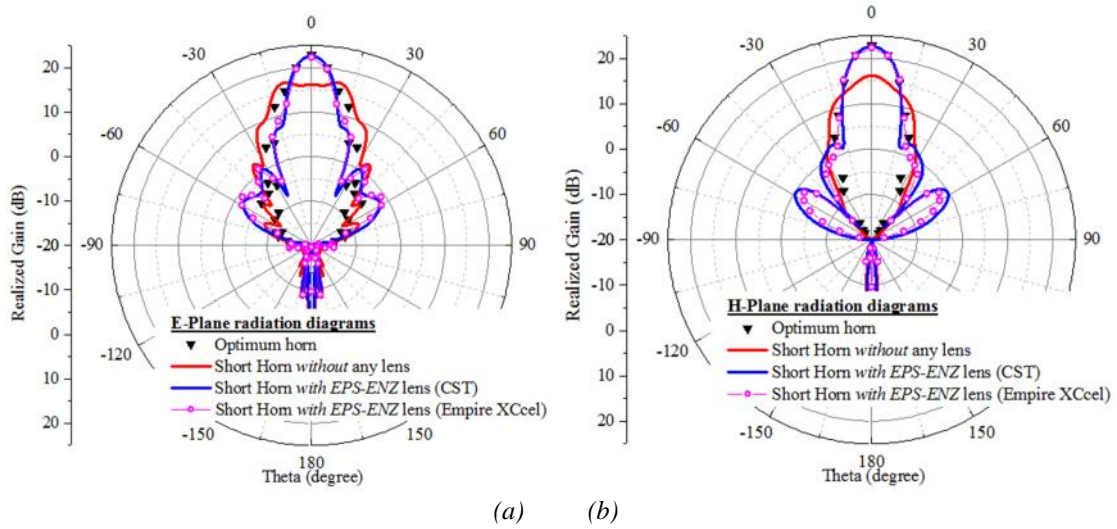
Fig. 54: Comparison between the radiation patterns of conical horns at 6.2 GHz on the (a) E–plane and (b) H–plane.

The amplitude of the scattering parameter S_{11} at the input port of the horns is shown in . It is possible noticing that the presence of the crossed WM on the aperture does not affect the matching properties of the antenna: S_{11} amplitude is well below the reference value of *-10 dB* from *5.75 GHz* to *7.00 GHz*
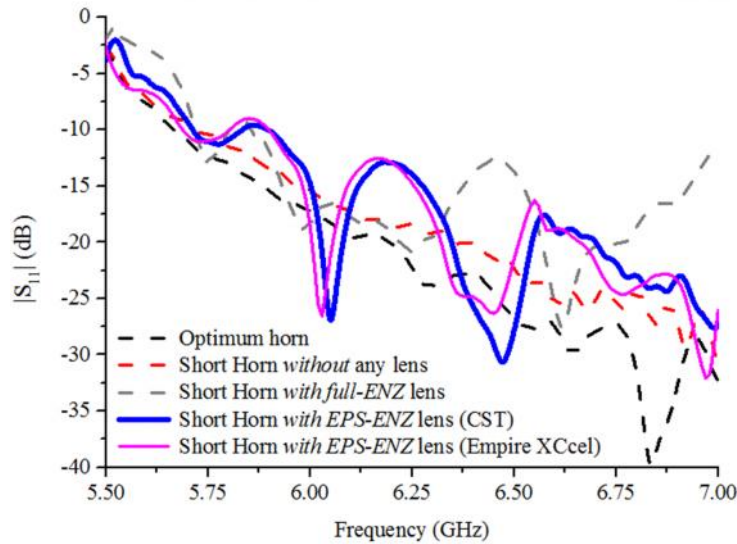
Fig. 55: Comparison between the amplitudes of the scattering parameters S_{11} of the optimum conical horn and of the shortened versions without any lens, with full-ENZ lens and with EPS–ENZ lens.

Now I consider an optimum pyramidal horn antenna (Fig. 56a) designed to exhibit *23 dBi* of gain in the broadside direction at *6 GHz*. The dimensions of the feeding

waveguide are $a = 40.4\,mm$ and $b = 20.2\,mm$, whereas the dimensions of the horn are $A = 409.6\,mm$, $B = 204.8\,mm$ and $L_{opt} = 695.2\,mm$. As an example, let us consider also in this case a shortened version of the optimum horn whose length L_S is 50% shorter than the one of the optimum horn (Fig. 56b). The aperture of the shortened antenna is loaded with an EPS–ENZ lens, where the EPS medium is again air and the ENZ part is made by two different crossed WMs, because of the different phase–shifts of the propagating field along the two flares. In this case, thus, the lens design consists in two steps: one for the E–plane and one for the H–plane. Following the same design procedure of the shortened conical horn, the dimensions of the EPS–ENZ lens for the pyramidal horn are the following: $A_L = 276.0\ mm$, $B_L = 142.6\ mm$, $d_L^E = 15.1\ mm$ and $d_L^H = 39.0\ mm$, where the superscripts E and H refer to the E– and the H–plane, respectively. Also in this case, we have compared four pyramidal horns: the optimum one and the shortened one without any lens, with full-ENZ lens, and with the proposed EPS–ENZ lens.

(a)   *(b)*
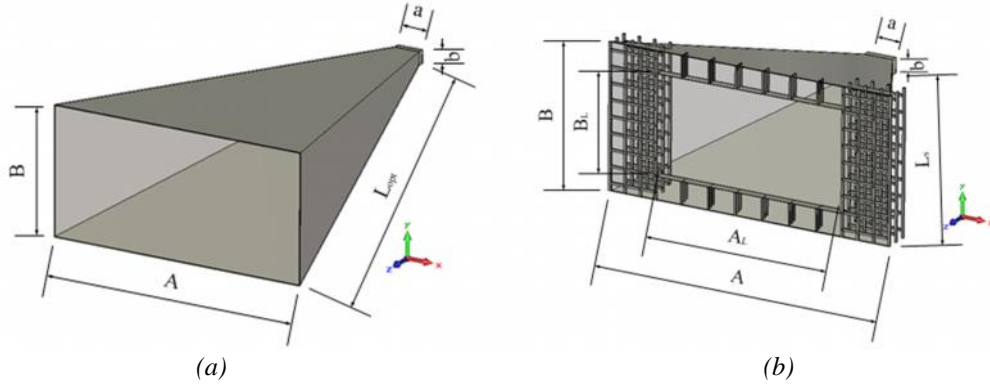
Fig. 56: Prospective view of (a) the optimum pyramidal horn with length L_{opt} and (b) the shortened pyramidal horn with length L_S.

In Fig. 57, I report the broadside gain as a function of the frequency of the four horn antennas. It is worth noticing that also for the pyramidal horn it is possible to achieve a gain enhancement over a broad frequency range by using the ESP-ENZ lens. The broadside gain of the shortened pyramidal horn in Fig. 56b is close to the one of the optimum horn in Fig. 56a. Again, the shortened horn loaded with a full–ENZ lens

exhibits a gain improvement only in a narrow band close to the plasma frequency of the WM, where it acts as a spatial filter.
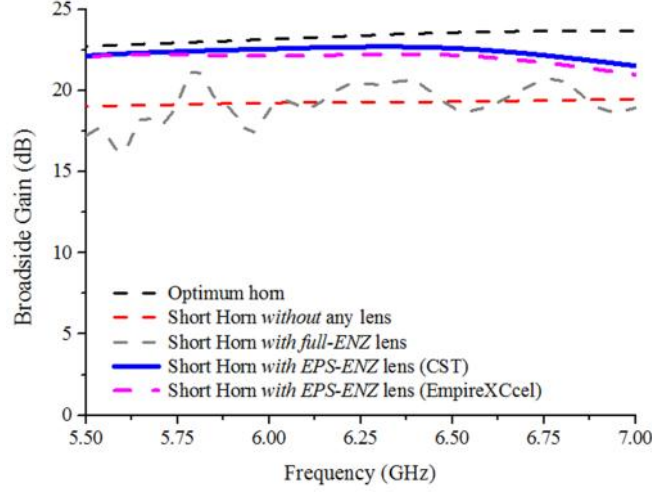
Fig. 57: Comparison between the broadside gain of the optimum pyramidal horn and of the shortened versions without any lens, with full-ENZ lens and with EPS–ENZ lens.

In Fig. 58, the radiation patterns at *6.00 GHz* of the optimum horn and of the shortened one with and without the lens are reported. It is worth noticing that also in the case of the pyramidal horn the optimum one and the proposed shortened version with the EPS-ENZ lens exhibit the same beamwidth and the same values of the realized gain. The side-lobe level is lower than *-10 dB* on both planes. Side lobes are higher than in the case of the conical horn, but their level is still much lower than *-10 dB*. This design and its performances can be directly compared to the state-of-the-art solutions that are intrinsically narrowband [35]-[39].
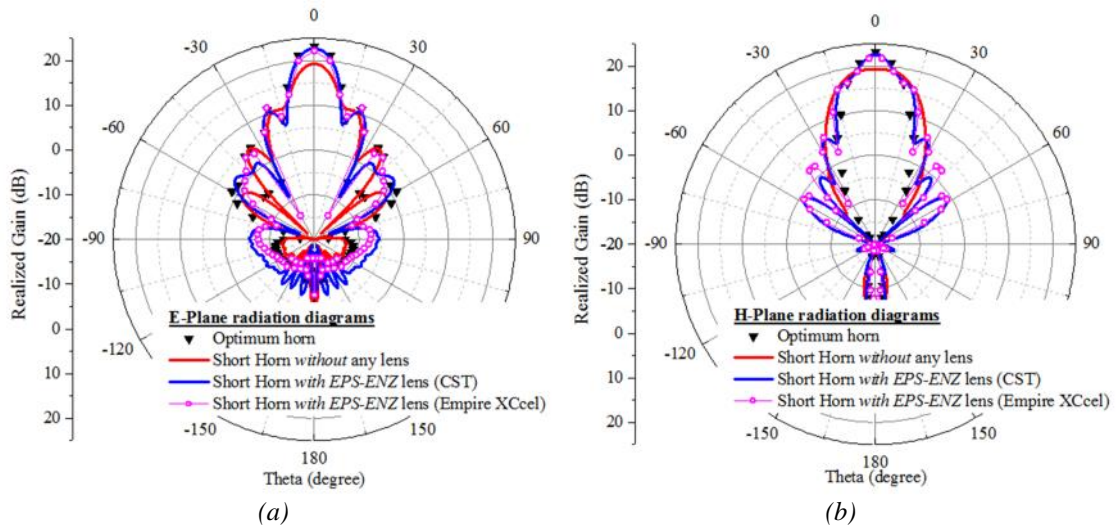
Fig. 58: Comparison between the radiation patterns of pyramidal horns at 6.0 GHz on the (a) E–plane and (b) H–plane.

Finally, in Fig. 17, I report the amplitude of the scattering parameter S_{11} at the input port of the horn antennas. The presence of the EPS–ENZ lens on the aperture does not affect the matching properties of the antenna: the S_{11} amplitude is around *-30 dB* over the entire band of interest (from *5.50 GHz* to *7.00 GHz)*.
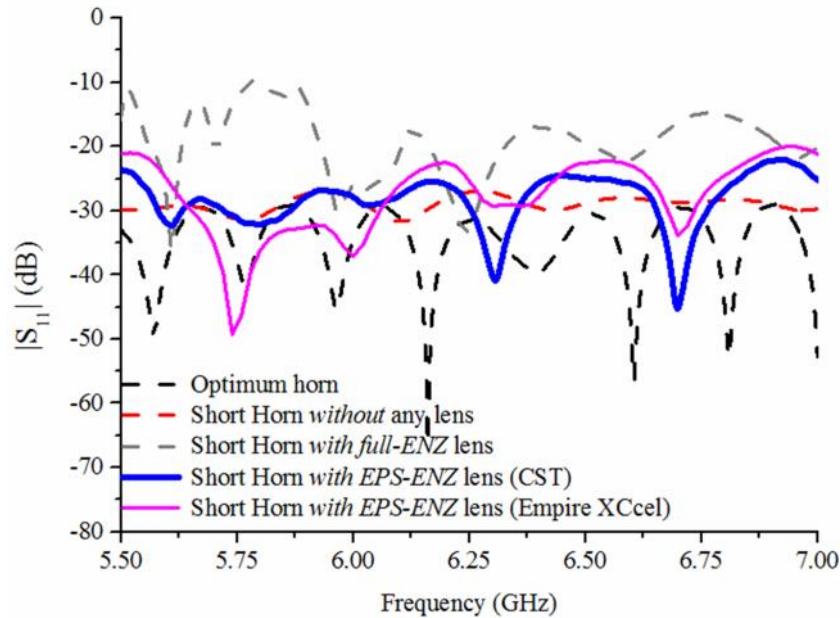
Fig. 59: Comparison between the amplitudes of the scattering parameters S_{11} of the optimum pyramidal horn and of the shortened versions without any lens, with full-ENZ lens and with EPS–ENZ lens.

3.2.4 Discussion and conclusions

Here, I have presented the design of an artificial flat lens made of a conventional material and an ENZ metamaterial. The lens is applied to the aperture of a shortened horn antenna, in order to achieve radiation performances similar to the ones of the corresponding optimum horn over a broad frequency range. The design formulas for the lens have been derived and the whole design procedure has been presented. Then, realistic versions of the lens for both conical and pyramidal horn antennas have been proposed by using a crossed WM and applied to shortened horn antennas working in C-band, whose lengths are half the length of the corresponding optimum horns. The radiating performances of the shortened horns loaded with the proposed lens are similar to the ones of the optimum horn over a broad frequency band, overcoming the narrowband behavior of the previous solutions proposed in the literature employing ENZ-based lenses. This new class of compact broadband radiators can be widely employed in satellite and radar systems.

3.3 Horn antennas with steerable beam

Recently, some groups investigate the possibility to use tunable metamaterials to realize antenna radome that allows the deviation of the main beam [48]. Although such a technique is interesting, it requires of more than one radiator to achieve high gains and, also, the radome increases the dimensions of the antenna system because it is an external add-on.

Here, I propose an approach in which a single horn antenna system is equipped with the steerable function without increasing the dimensions of the antenna system. The steering is obtained by using a metamaterial epsilon-near-zero (ENZ) lens properly loaded with some lumped elements. The lens consists of a wire medium that is directly plugged on the antenna aperture in order to avoid to increase of the size of the antenna. In order to achieve the beam steering, part of the lens is loaded with lumped elements, whereas the rest is not. The lumped elements change locally the effective permittivity function of the wire medium and, thus, when the wave propagates through, the phase velocity is different, leading to a desired far field radiation pattern.

In the following, the design of the lens is presented and then I report of some numerical results of the antenna with steerable radiation diagram

3.3.1 Inductive loads for the wire-medium

The wire medium is a typical metamaterial structure consisting of an dense array of thin wires aligned in a certain direction. It is employed to realize an artificial material that exhibits negative, or less than unity, values of the relative permittivity function. In order to consider such artificial structure as a uniform materials, it is required that the diameter and periodicity of the array is much smaller than the operating wavelength and, thus, the single wire is excited by an quasi-static electromagnetic field.

Consider the wire medium in air shown in Fig. 60, where the periodicity is a and the radius of the wires is r_0. Assume that the external electric field is parallel to the wire axes and consider only a part of the infinitely conducting wires of length d.
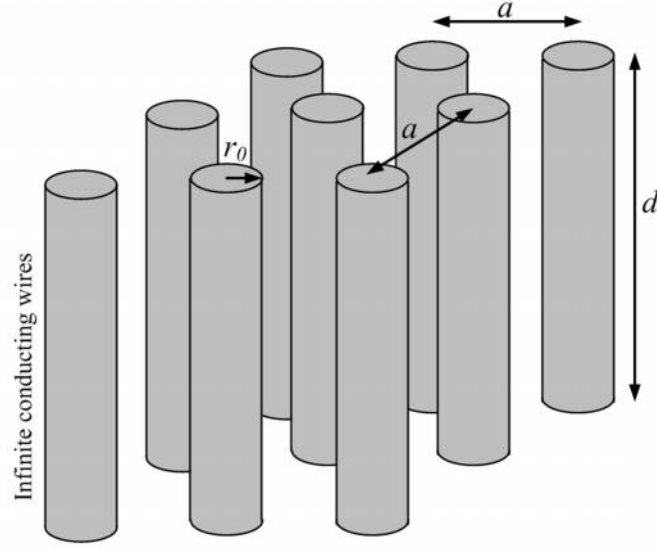
Fig. 60: Geometry of a wire-medium: an infinite periodical array of conducting wires.

Due to the external electric field E, a voltage difference $V=Ed$ is present between any two point spaced of d along a wire. So a current I flows along the wire itself, which reads, from the circuit theory:

$$V = j\check{S}LdI = Ed \qquad (47)$$

where L is the inductance p.u.l. (per unit of lenght) of the single wire.

Now, the current I that flows in the wire medium affects the polarizzability of the medium itself. By using the expression in (47), I can write:

$$P = \frac{J}{j\check{S}} = \frac{I}{j\check{S}a^2} = -\frac{E}{\check{S}^2 a^2 L} \qquad (48)$$

Consequently, the electric displacement vector D is related to the electric field an to the polarization inside the medium as follows:

$$D = \mathsf{v}_0 E + P = \left(\mathsf{v}_0 - \frac{1}{\check{S}^2 a^2 L}\right) E \qquad (49)$$

The terms in brackets in eq. (49) is the first order expression that represents the effective permittivity of the wire medium. It is possible to note that the negative

permittivity is obtained acting on the periodicity of the array and on the inductance p.u.l. of the single wire. Moreover, a dependence on the frequency confirms the intrinsic dispersivity of the metamaterials. The plasma frequency, i.e. the frequency at which D=0, is:

$$\check{S}_p = \frac{1}{\left(v_0 a^2 L\right)^{1/2}} \tag{50}$$

The electromagnetic properties of the wire medium at a given frequency, so, can be tailored acting on these two parameters, i.e. periodicity a and inductance L. The periodicity a is a mechanical characteristic of the medium and, thus, difficult to change quickly for a rapid configuration of the electromagnetic properties of the medium. On the contrary, the inductance L is an electrical parameter and it can be changed properly loading the wires with inductive lumped elements. Considering this second method, I can write:

$$\check{S}_p^{(load)} = \frac{1}{\left(v_0 a^2 \left(L + L_{load}\right)\right)^{1/2}} \tag{51}$$

that is the plasma frequency of the loaded wire medium. Since only positive values of L_{load} are permitted, the plasma frequency of the loaded wire medium results smaller than the one of the stand-alone wire medium. In Fig. 61, I report a qualitative graph for the comparison between of a loaded and unloaded wire medium, whose effective permittivity is well described by the Drude model.
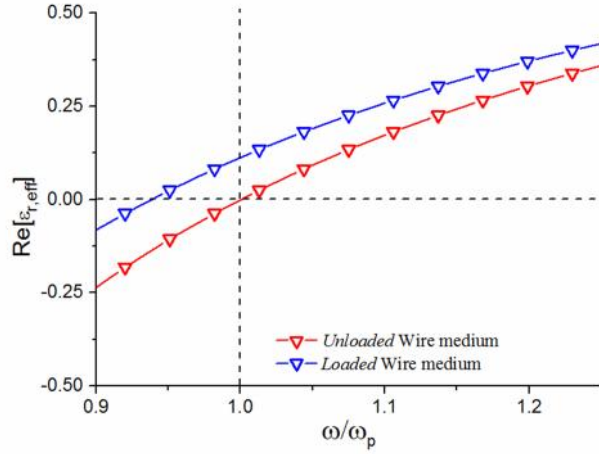
Fig. 61: Comparison between the real parts of effective permittivity function of a loaded and an unloaded wire medium.

It is possible to note from Fig. 61 that around the plasma frequencies of both wire mediums the values of the permittivity for the loaded WM are always higher than the ones of the unloaded WM. Remembering that the phase delay experienced by a wave through a slab of thickness h is $\Delta\{ = k_0\sqrt{v_{eff}}\,h$, the wave experiences an higher phase delay when propagates in the loaded wire medium with respect to the one in the unloaded counterpart. This feature will be deeply exploited in the following to realize the horn antenna with steerable radiation diagrams.

3.3.2 Horn antenna with steered main beam

Here, I present the layout and the electrical and radiation performances of an horn antenna working in C band with the ENZ lens that allows to achieve the electronic steering of the main beam.

In Fig. 62 the horn antenna working in C-band with the wire medium lens id shown. The dimensions are the following: $A = 180mm$, $B = 138.4mm$, $a = 39.55mm$, $A = 19.78mm$, $L_{horn} = 160mm$. The antenna ha been designed in order to have a gain $G_{max} = 18.1dBi$ at 6 GHz.
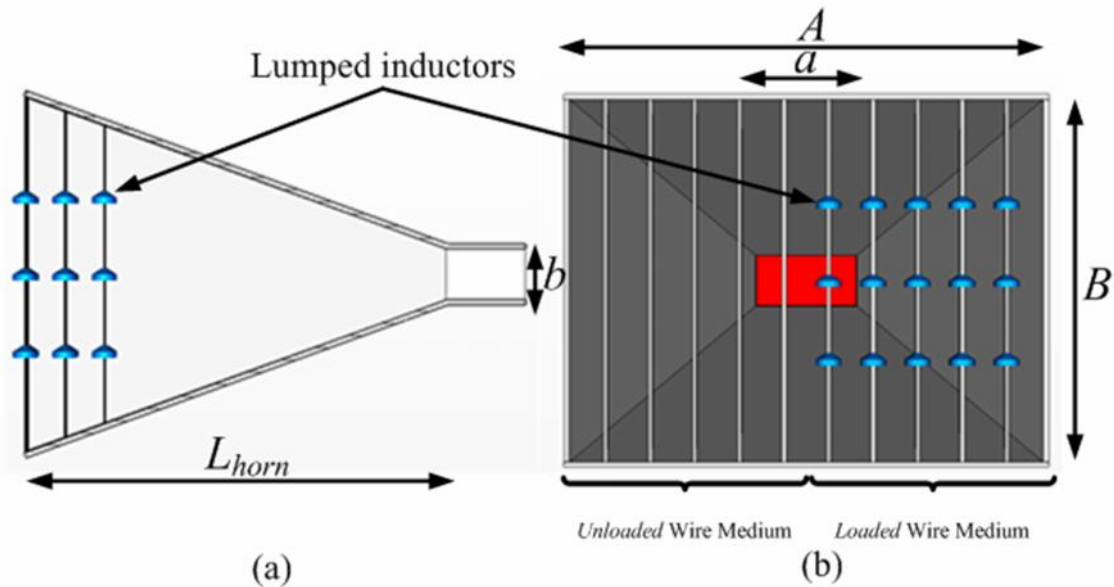
Fig. 62: Horn antenna with wire-medium lens with loaded and unloaded wires.

The lens is composed by three rows of metallic wires spaced of 15 mm. The distance between the wires of the same row is 16.9 mm and the value of the inductances is 7 nH. This values have been derived numerically [42] in order to maximize the transmission through the wire medium at the desired frequency, i.e. 5.9 GHz.

First of all, I report the scattering parameter S_{11} at the input port of the antenna shown in Fig. 63 because it indicates if the presence of the wire medium disturbs or not the propagation of the radiated field. In this case, the scattering parameter S_{11} is well below the -15 dB around the design frequency.
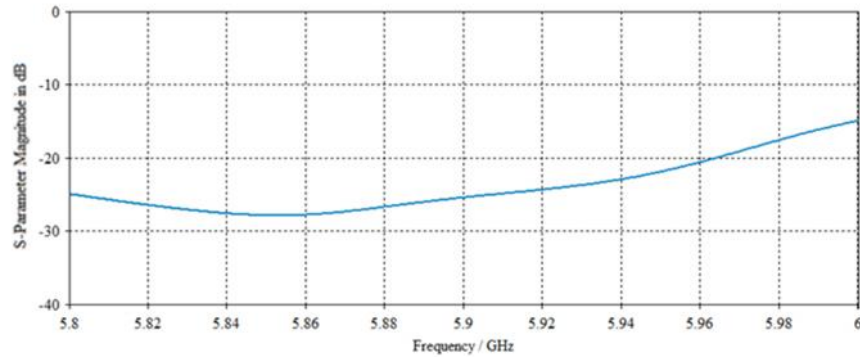
Fig. 63: Scattering parameter S_{11} at the input port of the antenna versus frequency.

As far as the radiation performances are concerned, I report in Fig. 64 the maps of the radiated electric field. In Fig. 64a, it is possible to see the propagation of the electric field from above the antenna. The portion of field that interacts with the unloaded wire medium propagates with an higher phase velocity with respect to the one that propagates in the loaded one and, thus a rotation of the phase front is obtained at the output. In particular, in Fig. 64b, I report the phase map of the electromagnetic field on the aperture of the antenna, where it is possible to note the two areas with different phase values.

(a)

(b)
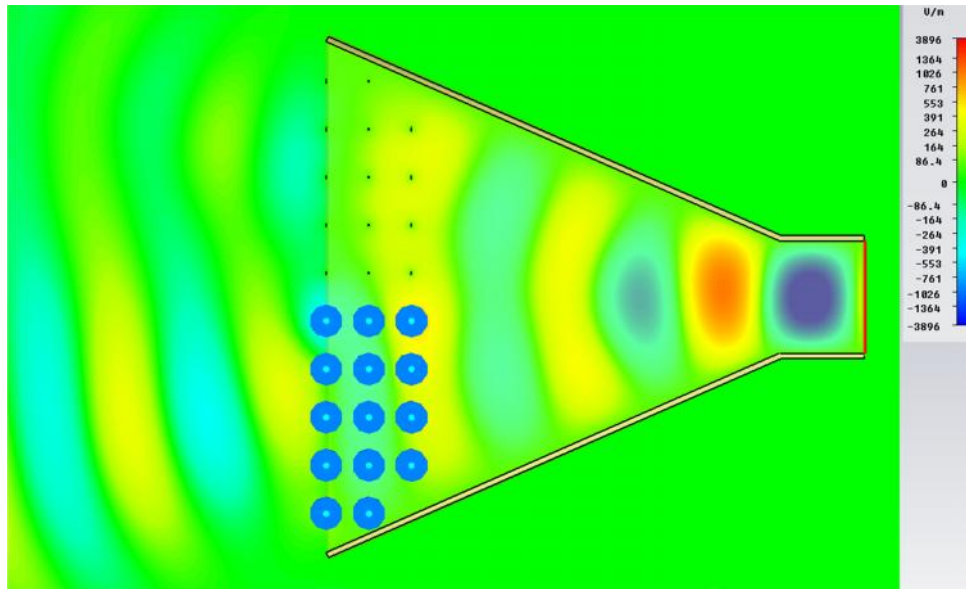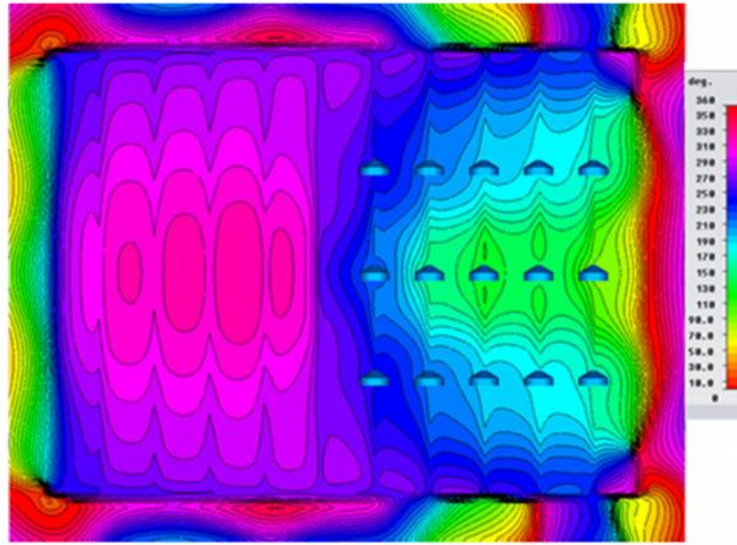
Fig. 64: Map of the electric field: (a) upper view; (b) front view.

The rotation of the phase fronts leads to a tilt of the direction of the maximum gain and, thus, to a steered main beam as shown in Fig. 65.
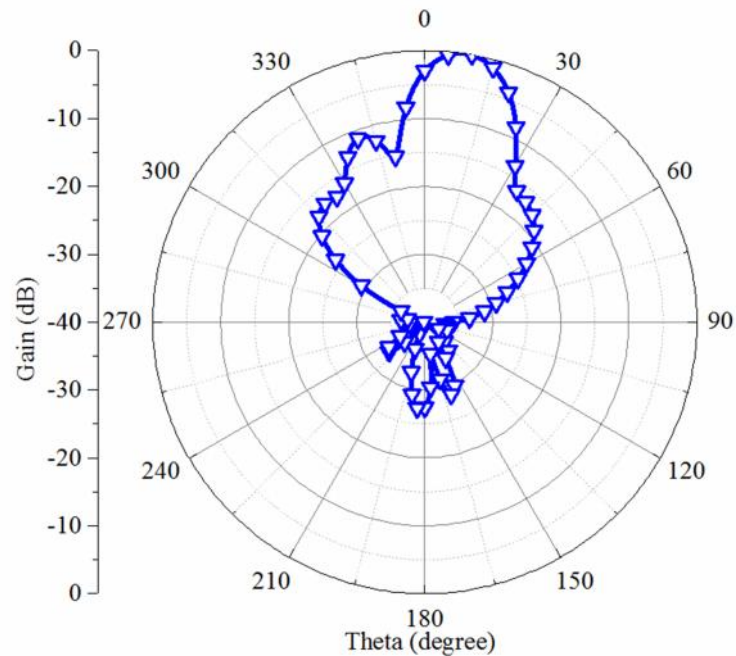
Fig. 65: H-plane radiation diagram at the design frequency (5.9 GHz).

3.4 References

[1] V. G. Veselago, "The electrodynamics of substances with simultaneously negative values of and μ", *Soviet Physics Uspekhi,* vol. 10, pp. 509–514, 1968.

[2] D. R. Smith, W. J. Padilla, D. C. Vier, S. C. Nemat–Nasser, and S. Schultz, "Composite medium with simultaneous negative permeability and permittivity", *Phys. Rev. Lett.,* vol. 84, 4184-4187, 2000.

[3] R. A. Shelby, D. R. Smith, and S. Schultz, "Experimental verification of a negative index of refraction", *Science*, vol. 292, no. 5514, pp. 77–79, 2001.

[4] D. R: Smith, J. B. Pendry, M. C. K. Wiltshire, "Metamaterials and negative refractive index", *Science,* vol. 305, no. 5685, pp.788–792, Aug. 2004.

[5] T. J. Cui, D. R. Smith, R. Liu, *Metamaterials: theory, design, and applications*, Ed. New York: Springer Science, 2010.

[6] A.Grbic A. and G. V. Eleftheriades, "Experimental verification of backward wave radiation from a negative refractive index metamaterial," *J. Appl. Phys.*, vol. 92, pp. 5930–5935, Nov. 2002.

[7] R. W. Ziolkowski, and E. Heyman, "Wave propagation in media having negative permittivity and permeability," Phys. Rev. E, vol. 64, p. 056625, Oct. 2001.

[8] A.Sihvola, Electromagnetic mixing formulas and applications, IEE Publishing, Electromagnetic Wave Series, London, 1999.

[9] S. Tretyakov, *Analytical modeling in applied electromagnetics*, Ed. Boston: Artech House, 2003.

[10] J. B. Pendry, A. J. Holden, W. J. Steward, and I. Yungs, "Extremely low frequency plasmons in metallic mesostructures" *Phys. Rev. Lett.*, vol. 76, no. 25, pp. 4773–4776, Jun. 1996.

[11] F. Bilotti, A. Toscano, L. Vegni, K.B. Alici, K. Aydin, and E. Ozbay, "Equivalent Circuit Models for the Design of Metamaterials based on Artificial Magnetic Inclusions," *IEEE Trans. Microw. Theory Tech.*, vol. MTT-55, no. 12, pp. 2865–2873, Dec. 2007.

[12] S. Tricarico, F. Bilotti, and L. Vegni, "Multi-functional dipole antennas based on artificial magnetic metamaterials," *IET Microw., Ant. Propag.*, vol. 4, pp. 1026-1038, 2010.

[13] K. Aydin, A. O. Cakmak, L. Sahin, Z. Li, F. Bilotti, L. Vegni, and E. Ozbay, "Split ring resonator-coupled enhanced transmission through a single subwavelength aperture," *Phys. Rev. Lett.*, vol. 102, no. 013904, Jan. 2009.

[14] F. Bilotti, A. Alù, and L. Vegni, "Design of Miniaturized Metamaterial Patch Antennas with µ-Negative Loading", *IEEE Trans. Antennas Propag.*, vol. AP-56, no. 6, pp. 1640–1647, 2008.

[15] A.Alù, F. Bilotti, N. Engheta, L. Vegni, "Sub-Wavelength Planar Leaky-Wave Components with Metamaterial Bilayers", *IEEE Trans. Antennas Propag.*, vol. 55, no. 3, pp. 882–891, Mar. 2007.

[16] F. Bilotti, L. Nucci, and L. Vegni, "An SRR Based Microwave absorber," *Microw. Opt. Tech. Lett.*, vol. 48, no. 11, pp. 2171–2175, Nov. 2006.

[17] M. Gil, J. Bonache, J. Garcìa-Garcìa, J. Martel, and F. Martin, "Composite right/left-handed metamaterial transmission line based on complementary split-rings resonators and threir applications to very compact filter design", *IEEE Trans. Microw. Theory Tech.*, vol. 55, no. 6, pp. 1296–1304, 2007.

[18] C. Caloz and T. Itoh, "Novel microwave devices and structures based on the transmission line approach of metamaterials", in *IEEE-MTT Int. Microw. Symp. Dig.*, Philadelphia, PA, Jun. 2003, vol. 1, pp. 195–198.

[19] J. Perruisseau-Carrier and A. K. Skrivervik, "Composite right/left-handed transmission line metamaterial phase shifters (MPS) in MMIC technology", *IEEE Trans. Microw. Theory Tech.*, vol. 54, no. 4, pp. 1582–1589, Jun. 2006.

[20] R.W. Ziolkowski, "Propagation and scattering from a matched metamaterial having a zero index of refraction," Phys. Rev. E, vol. 70, p. 046608, 2004

[21] A.Alù, M. Silveirinha, A. Salandrino, and N. Engheta, "Epsilon-near-zero metamaterials and electromagnetic sources: tailoring the phase pattern," Phys. Rev. B, vol. 75, no. 15, p. 155410, Apr. 2007.

[22] A.Monti, F. Bilotti, A. Toscano, and L. Vegni, "Possible implementation of epsilon-near-zero metamaterials working at optical frequencies," *Opt. Comm.*, "doi:10.1016/j.optcom.2011.12.037", Dec. 2011.

[23] Alù, F. Bilotti, N. Engheta, and L. Vegni, "Metamaterial covers over a small aperture," *IEEE Trans. Antennas Propag*., vol. AP-54, no. 6, pp. 1632–1643, Jun. 2006.

[24] Edwards, A. Alù, M. Silveirinha, and N. Engheta, "Reflectionless sharp bend and corners in waveguides using epsilon-near-zero effects," *Jour. Appl. Phys*., vol. 105, no. 4, p. 044905, Feb. 2009.

[25] Alù, and N-. Engheta, "Coaxial-to waveguide matching with -near-zero ultranarrow channels and bends", *IEEE Trans. Antennas Propag.*, vol. 52, no. 2, pp- 328–339, Feb. 2010.

[26] S. Kyriazidou, R. E. Diaz, and N. G. Alexòpoulos, "Radiation properties of microstrip elements in a dispersive substrate of permittivity less than unity," in *IEEE AP-S. Int. Symp*., Atlanta, GA, Jun. 21–26, 1998, vol. 2, pp. 660–663.

[27] S. Enoch, G. Tayeb, P. Sabouroux, N. Guèrin, and P. Vincent, "A metamaterial for directive emission," *Phys. Rev. Lett*., vol. 89, no. 21, p. 213902, Nov. 18, 2002.

[28] A.Alù, F. Bilotti, N. Engheta, and L. Vegni, "Sub-wavelength planar leaky-wave components with metamaterial bilayers," *IEEE Trans. Antennas Propag*., vol. 55, no. 3, pt. 2, pp. 882–891, Mar. 2007.

[29] Alù, F. Bilotti, N. Engheta, and L. Vegni, "Theory and simulations of a conformal omnidirectional sub-wavelength metamaterial leakywave antenna," *IEEE Trans. Antennas Propag*., vol. 55, no. 6, pt. 2, pp. 1698–1708, June 2007.

[30] S.J. Orfanidis, *Electromagnetic Waves and Antennas,*2008. Online book available at: http://www.ece.rutgers.edu/~orfanidi/ewa.

[31] A. Balanis, *Antenna Theory: analysis and design, 3rd Ed.*, Ed.New York: Wiley, 2005.

[32] J. L. Volakis, *Antenna engineering handbook, 4th Ed*., Ed. McGraw-Hill, 2007

[33] A.D. Olver, P. J. B. Clarricoats, A. A. Kishk, and L. Safai, *Microwave Horn and Feeds*, IEE Press, 1994.

[34] R. J. mailoux, *Phase Array Antenna Handbook*, Artech House, Norwood, MA, 1994.

[35] Q. Wu, P. Pan, F. Meng, L. Li, and J. Wu, "A novel flat lens horn antenna designed based on zero refraction principle of metamaterials," *Appl. Phys. A,* vol. 87, pp. 151–156, Jan. 2007.

[36] S. Hrabar, D. Bonefacic, and D. Muha, "Numerical and experimental investigation of horn antenna with embedded ENZ metamaterial lens," in *ICECom Int Conf.,* Dubrovnik, CR, Sep. 24–26, 2007, pp.1–4.

[37] S. Hrabar, D. Bonefacic, and D. Muha, "ENZ–based shortened horn antenna: an experimental study," in *IEEE AP-S Int. Symp.,* SanDiego, CA, Jul. 5–11, 2008, pp.1–4.

[38] S. Hrabar, D. Bonefacic, and D. Muha, "Application of wire-based metamaterials for antenna miniaturization", in *EuCAP2009*, Berlin, D, Mar. 23–27 ,2009, pp. 620–623.

[39] S. Hrabar, M. Damir, and Z. Sipus, "Optimization of wire–medium–based shortened horn antenna," in *EuCAP2010*, Barcelona, SP, Apr. 12–16, 2010, pp. 1–4.

[40] J. D. Jackson, *Classical Electrodynamics*, Ed. New York: Wiley, 1999.

[41] Y. Tan and K. T. Selvan, "A performance comparison of a Ku-band conical horn with an inserted cone-sphere with horns with an integrated dielectric lens and metamaterial loading," *IEEE Antennas Propagat. Mag*., vol. 53, no. 5, pp. 115–122, 2011.

[42] CST Studio Suite 2012. www.cst.com.

[43] R. Smith, S. Schultz, P Markos, and C.M. Soukoulis, "Determination of effective permittivity and permeability of metamaterials from reflection and transmission coefficients" *Phys. Rev. B*, vol. 65, p. 195104, Apr. 2002.

[44] X. Chen, T. M. Grzegorczyk, B. Wu, J. Pacheco, and J.A. Kong, "Roboust method to retrieve the constitutive effective parameters of metamaterials", *Phys. Rev. E*, vol. 70, p. 016608, Jul. 2004.

[45] A.Alù, "First-principles homogenization theory for periodic metamaterials," *Phys. Rev. B*, vol. 84, p. 075153, 2011.

[46] P. King, "The radiation characteristics of conical horn antennas" in *IRE* , vol. 38, no. 3, pp. 249–251, 1950.

[47] Empire XCcel v.6.00, www.empire.de.

[48] H. Chen, B. Wu, L. Ran, T. Grzegorczyk, and J.A. Kong, "Controllable left-handed metamaterial and its application to a steerable antenna", *Appl. Phys. Lett.*, Vol. 89, p. 053509, 2006.

4 Guiding and radiating components at IR and optical frequencies

In this chapter, the design and the performances of an optical waveguide and horn antenna working at near-infrared frequencies are discussed. First, I focus the attention on the nano-waveguide, which should satisfy some important requirements to be a good nano-waveguide: on one hand side, it should effectively guide the light and, on the other hand, it should present a topology that is similar to its counterpart at microwave frequencies. I start the design considering a symmetric nano-transmission line constituted by a non-plasmonic material slab sandwiched between two plasmonic layers that may represent a suitable candidate for this purpose. Such a structure supports a fundamental forward mode confined between the two metallic layers having a strong electric field component orthogonal to them.

Then, I consider the problem to effectively radiate the guided electromagnetic field because recently the antenna concept has been brought to the attention of physics and optics communities, due the possible applications in energy harvesting, smart lighting, and optical wireless communication links. In addition, the recent advancements in nano-technology make the actual fabrication of such devices ever more attractive. Here, I present an horn nano-antenna obtained shaping at one of the ends of the nano-waveguide in such a way to increase the physical aperture and progressively match the wave-impedance of the waveguide to the one of free-space.

4.1 Introduction

In the last decades, plasmonic waveguides have been extensively investigated as alternative to conventional dielectric-based waveguide [1]-[8]. The propagation along a plasmonic waveguide is given by the surface plasmons (SPs), which are a transverse magnetic (TM) waves propagating along metal-dielectric interfaces with fields exponentially decaying in both media. The propagating optical mode is extremely confined to subwavelength scale and minimizing the optical mode size. Typically the metals used for plasmonic waveguide are silver, gold and, sometimes, also copper because at near-infrared and visible frequencies they do not behave as conductors, but as dielectrics with negative values of the real part of the effective permittivity [9]. The surface plasmon-polariton propagates at the interface between the metal (negative permittivity) and the conventional dielectric (insulator, positive permittivity), under an external electromagnetic excitation.

Two complementary layouts can be used to create a plasmonic waveguide: the first is typically referred to as insulator-metal-insulator (IMI) waveguide that supports long-range SP because most part of the energy propagates in the lossless dielectric part of the waveguide [1],[2]; the second, on the contrary, is called metal-insulator-metal (MIM) SP waveguide that offers higher confinement factors and closer spacing to adjacent waveguides or structures[3],[4] and have been proposed for this and other potential applications [5]-[8]. In fact, the MIM structure has been highly investigated because it is very similar to the conventional parallel-plate wave working at microwave frequencies and shows comparable propagation characteristics. So, finite-length MIM structures has been used to create optical nano-cavities [10],[11], and also waveguide bends and splitters based on MIM subwavelength plasmonic waveguides have low loss over a wide frequency range [12]. Although in the previous studies the attention has been focused ti MIM structure because it guarantees more confinement of the energy, no investigation about the lateral confinement of the guided modes has been never reported in MIM structure. In fact, MIM structure has been always studied as infinitely extended in both directions orthogonal to stratified direction, just as a parallel plate waveguide at microwave frequencies.

Here, I report the design and guiding performances of an optical waveguide based on MIM structure, made of two thin silver parallel plate very close to each other separated by a gap of air, and combined with an array of silver pillar that ensures the requested lateral confinement. Such a structure support present a cutoff frequency and a guided mode very similar to the one in the conventional metallic waveguide working at microwave frequencies.

The possibility to have an optical waveguide that acts as a microwave waveguide is an important achievement in this field because it gives the possibility to design optical guiding and radiating components simply reproducing the geometries already known at the microwaves. In this framework, I investigate about the possibility to effectively radiate and capture the electromagnetic energy at such a frequency range by using a novel kind of nano-antenna: the horn nano-antenna.

Although the nano-antenna concept has been widely investigated exploiting many different geometries for the nano-antennas [13]-[17], the horn configuration represent a great achievement because one of the main advantages of such aperture antennas is that the transmission line and the radiating element are inherently matched one to the other, reducing, thus, the presence of undesired discontinuities and scattering losses. In addition, when the antenna works in the receiving mode – which is the case, for instance, of solar energy harvesting systems – the captured electromagnetic energy would be automatically guided and made available to the detector, without the necessity of implementing complex and non-linear electronics to extract the power stored around the nano-antenna.

In the following, I first present the design and electrical performances in term of insertion loss of the nano-waveguide. Then, the electrical and radiation properties of the innovative horn nano-antenna are reported and discussed.

4.2 Silver MIM nano-waveguide with pillars

As previously anticipated in the introduction, among the different configurations proposed in the literature, I decided to consider a metal–insulator–metal structure as the one shown in Fig. 66, where the metallic parts are made of silver.

Fig. 66: Sketch of a symmetric nano-transmission line infinitely extended in x- and y- directions constituted by a non-plasmonic material slab sandwiched by two plasmonic layers.

This symmetric nano-transmission line has been extensively studied in the past [18],[19] where the propagation along the structure has been explained in terms a cascade of nano-inductors and nano-capacitor. In fact, the plasmonic behavior of silver at near-infrared frequencies allows obtaining the required series inductance behavior along the line, while the dielectric nature of air returns the shunt capacitance. Such a structure supports a fundamental forward mode confined between the two metallic layers.

For what concerns the constitutive properties of the materials, silver has been described through the complex permittivity function $\varepsilon_{Ag} = \varepsilon_0(\varepsilon' + j\varepsilon'')$. Although the permittivity function can be approximated by a Drude-like model with plasma and damping frequencies set to 2175 THz and 4.35 THz, respectively, I preferred to use the experimental values are reported in [9]. In [9], Johnson and Christy report the real and imaginary part of the index of refraction of several different noble metals under the excitation of photons with different energy. Then, I relate the index of refraction to the complex permittivity and the photon energy to the frequency for the band of interest, i.e. near-infrared regime. In Fig. 67, I report the dielectric permittivity function of silver in the frequency band [150; 250] THz.
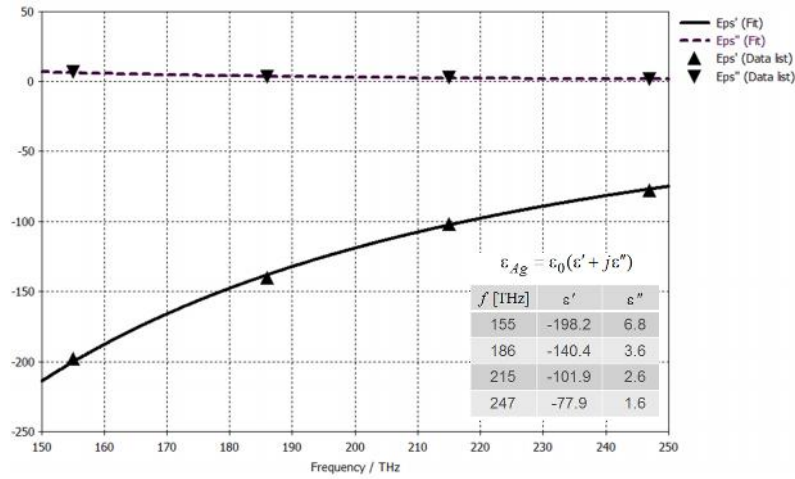
Fig. 67: Real and imaginary part of silver according to the experimental data in [9].

Although such a structure supports a fundamental forward mode, it does not acts as a regular waveguide ads the counterparts at the microwave frequencies because it is still infinitely extended in x- and y- directions (Fig. 66). Thus, in order to obtain a lateral confinement of the field inside the waveguide, cylindrical silver pillars arranged in a triangular lattice have been used, as reported in Fig. 68.

(a)   *(b)*
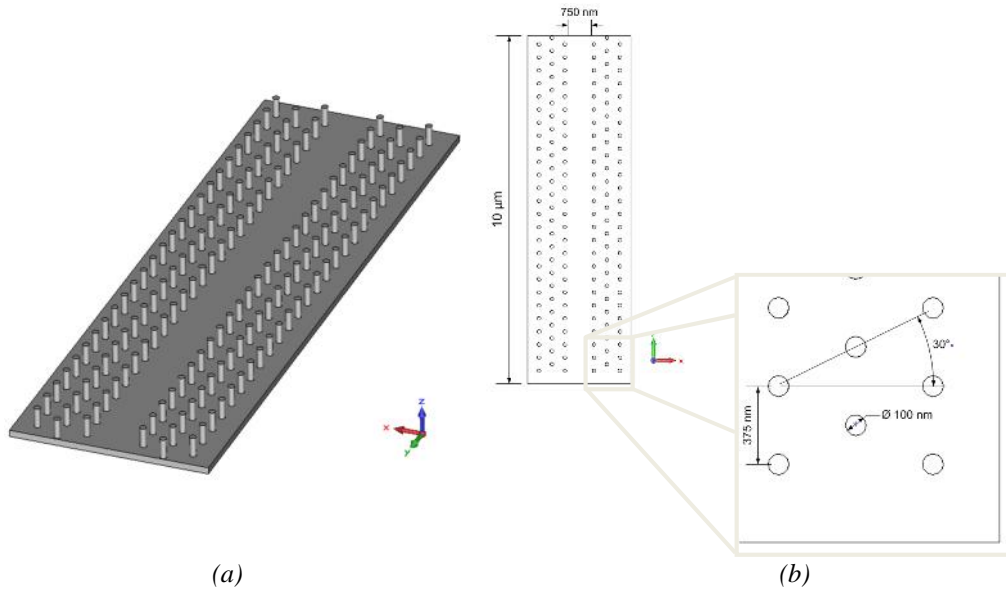
Fig. 68: Nano-waveguide working at near-infrared: (a) prospective and (b) dimensioned top view

The array of pillars acts as a photonic crystal and ensures that the electromagnetic wave propagate inside the waveguide. The perfect behavior of such a structure as a

regular waveguide can be derived looking at the transmission coefficient from one the other end of the waveguide as a function of the frequency (Fig. 69).
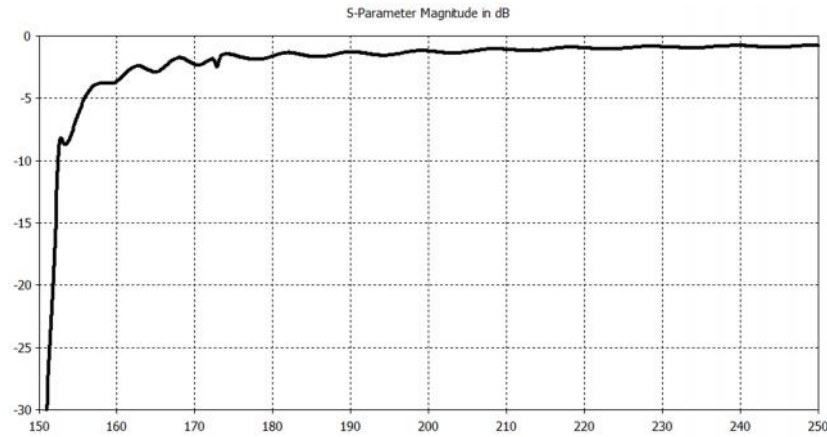
Fig. 69: Transmission coefficient of the nano-waveguide versus frequency.

As it is very well known from the waveguide theory, a regular waveguide at microwave frequencies lets the energy to propagate only if the frequency of the propagating wave is above a particular frequency, called cut-off frequency. It is worth noticing that the proposed nano-waveguide of Fig. 68 presents a cut-off frequency at about 155 THz. In Fig. 70, the map of the electrc field propagating along the waveguide is shown. The electromagnetic field is effectively confined inside the two silver parallel plates and the array of pillars.
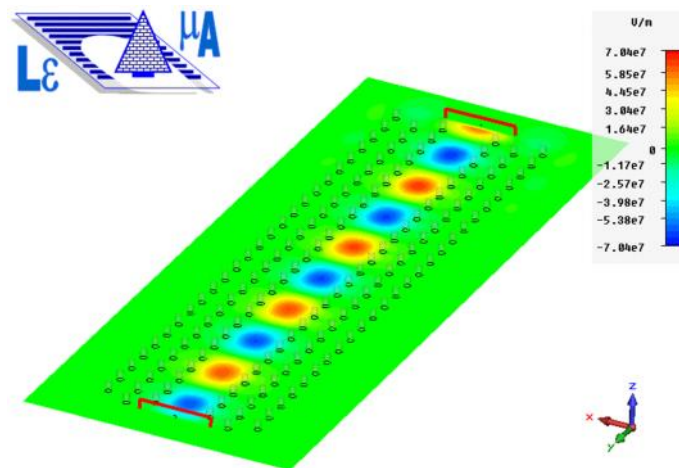
Fig. 70: Map of the electric field at 200 THz.

4.3 Horn nano-antenna: design and performaces

Once the Silver MIM waveguide works as the one working at microwave frequencies, the horn nano-antenna can be easily obtained divaricating the silver layers at one end of the waveguide. In fact, as it is well known in microwave engineering, an horn antenna is made of a metallic waveguide shaped at one of its ends in such a way to increase the physical aperture and progressively match the wave-impedance of the waveguide to the one of free-space. The radius of curvature used to taper the transmission line into the horn is defined using the smoothness parameter of the loft function available in CST Studio Suite. This parameter is set to 0.18.
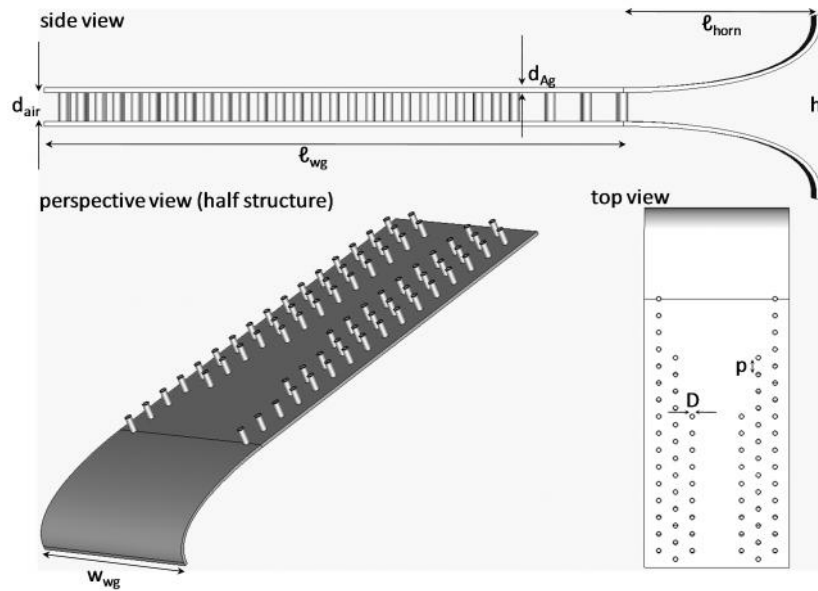
Fig. 71: Horn nano-antenna geometry. $\ell_{wg} = 6$ µm, $\ell_{horn} = 2$ µm, h = 1 µm, $w_{wg} = 1$ µm, $d_{air} = 300$ nm, $d_{Ag} = 50$ nm, D = 100 nm, p = 375 nm.

As previously anticipated, the nano-transmission line supports a fundamental forward mode at near-infrared frequencies, which is progressively transformed into a radiating mode by the horn shape. The electric field amplitude distribution at the reference wavelength of 1.5 µm reported in Fig. 3 clearly presents the described behavior and shows the similarities between a regular microwave horn and the proposed nano-antenna.

(a)

(b)
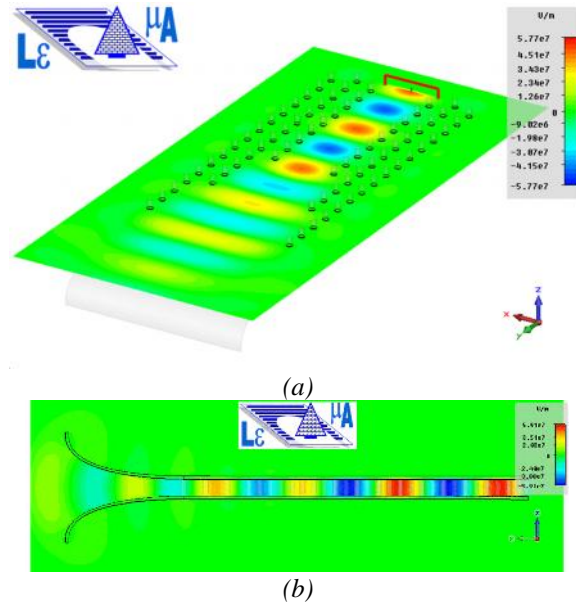
Fig. 72: Map of the electric field amplitude distribution at the design wavelength of 1.5 µm. (a) prospective view and (b) lateral view.

In microwave antenna engineering, the key parameter to describe the electrical properties of a radiator is given by the amplitude of the reflection coefficient at the input port. In Fig. 4 we report the variation of this parameter within the frequency band in which the fundamental mode is the only one excited in the waveguide. We note that the antenna is effectively matched with a reflection coefficient amplitude better than – 10 dB in a broad frequency band (more than 50%). In such a frequency band, thus, the optical signal is effectively leaving the source and propagating along the nano-transmission line.
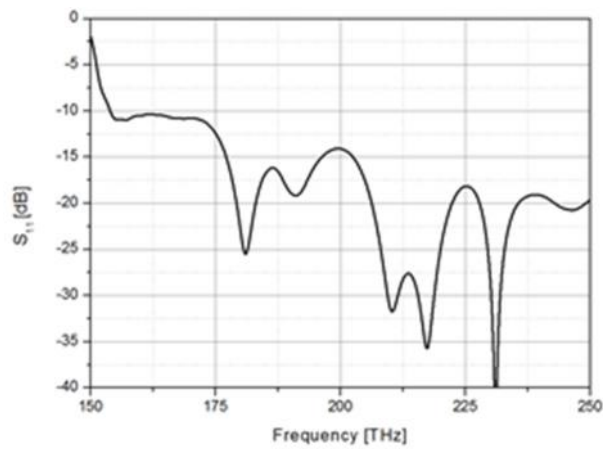
Fig. 73: Amplitude of the reflection coefficient (i.e. scattering parameter S11) at the input port of the horn nano-antenna reported in Fig. 71 as a function of frequency.

In order to test how effectively the propagating energy is radiated by the horn nano-antenna, we have calculated also the antenna 3D gain pattern at the reference wavelength of 1.5 µm (200 THz) and at other four sample points within the frequency band of mono-modal operation. The corresponding results are reported in Fig. 5 and confirm that the energy is not only transmitted through the nano-transmission line, but also efficiently radiated by the horn nano-antenna: antenna gain is greater than 10 dBi within the frequency range of interest.
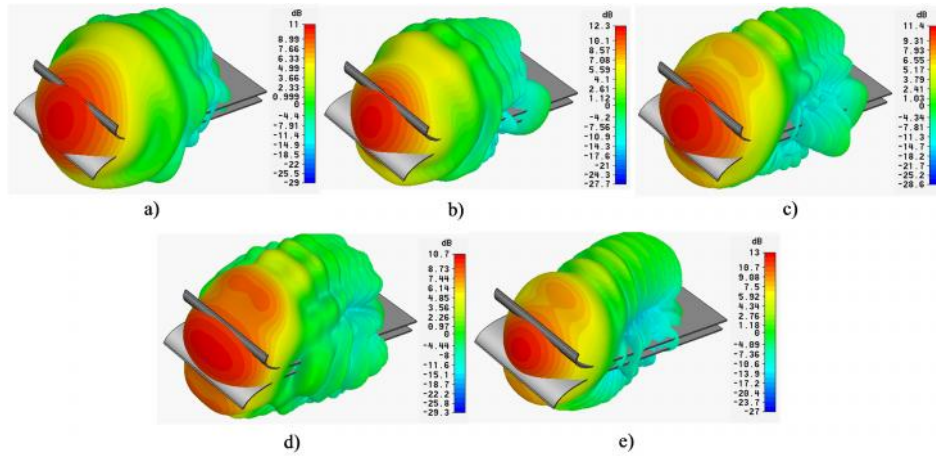
Fig. 74: 3D gain radiation pattern of the horn nano-antenna reported in Fig. 3 at a) 160 THz, b) 180 THz, c) 200 THz, d) 220 THz, and e) 240 THz.

To summarize, here I have presented the numerical design of an horn nano-antenna consisting of an Ag-air-Ag symmetric nano-transmission line divaricated at one of its ends in an horn shape. The nano-antenna has been designed to work in the near-infrared regime and the simulations performed have fully taken into account losses and dispersion of the involved materials. The results obtained (broad frequency range of operation and a realized gain greater than 10 dBi within the frequency band of operation) are rather promising and open the door to possible implementation of such nano-antennas in modern and future telecommunication systems and innovative energy harvesting devices. One intriguing possibility could be the use of such an antenna as the single element of a planar antenna array, whose beam is scanned in real-time through thermally or electrically tunable nano-circuits.

4.4 References

[1] T. Goto, Y. Katagiri, H. Fukuda, H. Shinojima, Y. Nakano, I. Kobayashi, and Y. Mitsuoka, "Propagation loss measurement for surface plasmon-polariton modes at metal waveguides on semiconductor substrates,"*Appl. Phys. Lett*. Vol. 84, pp. 852-854, 2004.

[2] R. Charbonneau, N. Lahoud, G. Mattiussi, and P. Berini, "Demonstration of integrated optics elements based on long-ranging surface plasmon polaritons," *Opt. Express*, Vol. 13, pp. 977-984, 2005.

[3] J. A. Dionne, L. A. Sweatlock, and H. A. Atwater, "Plasmon slot waveguides: Towards chip-scale propagation with subwavelength-scale localization," *Phys. Rev. B* , Vol. 73, p. 035407, 2006.

[4] R. Zia, M. D. Selker, P. B. Catrysse, and M. L. Brongersma, "Geometries and materials for subwavelength surface plasmon modes*," J. Opt. Soc. Am. A*, Vol. 21, pp. 2442-2446, 2004.

[5] P. Tournois and V. Laude, ''Negative group velocities in metal-film optical waveguides,'' *Opt. Commun*., Vol. 137, pp. 41-45, 1997.

[6] Y. Wang, ''Wavelength selection with coupled surface plasmon waves,'' *Appl. Phys. Lett*., Vol. 82, pp. 4385-4387, 2003.

[7] H. Shin, M. F. Yanik, S. Fan, R. Zia, and M. L. Brongersma, ''Omnidirectional resonance in a metal–dielectric–metal geometry,'' *Appl. Phys. Lett*., Vol. 84, pp. 4421-4423, 2004.

[8] J. S. Q. Liu and M. L. Brongersma, "Omnidirectional light emission via surface plasmon polaritons," *Appl. Phys. Lett.*, Vol. 90, p. 091116, 2007.

[9] P.B. Johnson, R.W. Christy, "Optical constants of the noble metals", *Phys. Rev. B*, Vol. 6, p. 4370, 1972.

[10] H. T. Miyazaki and Y. Kurokawa, "Squeezing visible light waves into a 3-nm-thick and 55-nm-long plasmon cavity," *Phys. Rev. Lett*., Vol. 96, p. 097401, 2006.

[11] Y. Kurokawa and H. T. Miyazaki, "Metal-insulator-metal plasmon nanocavities: Analysis of optical properties," *Phys. Rev. B*, Vol. 75, p. 035411, 2007.

[12] G. Veronis and S. Fan, "Bends and splitters in metal–dielectric–metal subwavelength plasmonic waveguides," *Appl. Phys. Lett*., Vol. 87, p. 131102, 2005.

[13] A. Alù, N. Engheta, "Tuning the Scattering Response of Optical Nanoantennas with Nanocircuit Loads", *Nat. Photon*., Vol. 2, p. 307, 2008.

[14] A. Alù, N. Engheta, "Input Impedance, Nanocircuit Loading, and Radiation Tuning of Optical Nanoantennas", *Phys. Rev. Lett*., Vol. 101, p. 043901, 2008.

[15] A. Alù, N. Engheta, "Hertzian Plasmonic Nanodimer as an Efficient Optical Nanoantenna", *Phys. Rev. B*, Vol. 78, p. 195111, 2008.

[16] H. Guo, T.Meyrath, T. Zentgraf, N.Liu, L. Fu, H. Schweizer, H. Giessen, "Optical resonances of bowtie slot antennas and their geometry and material dependence", *Opt. Expr.,* Vol. 16, p. 7756, 2008.

[17] R. Singh, C. Rockstuhl, C. Menzel, T. Meyrath, M. He, H. Giessen, F. Lederer, W. Zhang, "Spiral-type terahertz antennas and the manifestation of the Mushiake principle" *Opt. Expr*., Vol. 17, p.9971, 2009.

[18] A. Alù, and N. Engheta, "Three-dimensional nanotransmission lines at optical frequencies: a recipe for broadband negative-refraction optical metamaterials," *Phys. Rev. B*, Vol. 75, p. 024304, 2007.

[19] A. Alù, and N. Engheta, "Optical nanotransmission lines:synthesys of planar left-handed metamaterials in the infrared and visible regimes," *J. Opt. Soc. America B*, Vol. 23, No. 3, pp. 571-583, 2006.

List of Figures and Tables

Publications and presentations

1. **D. Ramaccia**, A. Toscano, A. Colasante, G. Bellaveglia, and R. Lo Forti, "Inductive tri-band double element FSS for space applications", *Progress in Electromagnetic Research C* , vol. 18, pp. 87-101, 2010 – Scientific paper.

2. **D. Ramaccia**, F. Bilotti, A. Toscano, and A. Massaro, "Efficient and wideband horn nanoantenna", *Optics Letters*, Vol.36, No. 10, pp.1743-1745, 2011 – Scientific paper.

3. **D. Ramaccia**, F. Bilotti, and A. Toscano, "Analitycal model of a regular array of sub-wavelength holes in a metal sheet", *Progress in Electromagnetic Research M,* Vol. 18, page 209-219, 2011 – Scientific paper.

4. **D. Ramaccia**, A. Toscano, and F. Bilotti, "A new accurate model of high-impedance surfaces consisting of circular patches", *Progress in Electromagnetic Research M*, Vol. 21, page 1-17, 2011 – Scientific paper.

5. F. Bilotti, L. Di Palma, **D. Ramaccia** and A. Toscano, "Self-Filtering Low-Noise Horn Antenna for Satellite applications", *IEEE Antennas Wireless Propag. Lett.*, Vol. 11, pp. 354–357, 2012 – Scientific paper.

6. **D. Ramaccia**, F. Scattone, F. Bilotti, and A. Toscano, "Design Formulas for ENZ/EPS Metamaterial lens for Broadband Compact Horn Antennas " *IEEE Trans. Antennas Propag.*, IEEEXplore Preprint, 2013 – Scientific Paper.

7. **D. Ramaccia**, A. Toscano, and L. Vegni, "Design of frequency selective surfaces tunable with the incidence angle for circular polarization application", Proc. of *XIX RiNEm – Riunione Nazionale sull'Elettromagnetismo,* Benevento, IT, September 6-10, 2010 – Poster presentation.

8. **D. Ramaccia**, A. Toscano, and L. Vegni, "Efficient design of frequency selective surfaces for the design of dichroic sub-reflectors for space applications", Proc. of *Metamaterials' 2010: 4th International Congress on Advanced EM Materials in MW and Optics*, Karlsruhe, GE, September 13-16, 2010 – Regular oral presentation.

9. **D. Ramaccia**, A. Toscano, and L. Vegni - "Equivalent analytical model of high-impedance surfaces made by circular metallic patches", Proc. of *ICECom 2010: 20th International Conference on Applied Electromagnetics and Communications,* Dubrovnik, CZ, September 20-23, 2010 – Regular oral presentation.

10. Colasante, R. Lo Forti, G. Bellaveglia, **D. Ramaccia**, and A. Toscano, "Inductive Ku/Ka bands double-elements frequency selective surface", Proc. of *32nd ESA Antenna Workshop on Antennas for Space Applications,* Noordwijk, NL, October 05-08, 2010 – Regular oral presentation.

11. Colasante, G. Bellaveglia, R. Lo Forti, **D. Ramaccia**, and A. Toscano, "Inductive Ku/Ka bands double resonant elements frequency selective surface", Proc. of *16th Ka and Broadband Communications, Navigation and earth observation Conference*, Milan, IT, October 20-22, 2010 – Regular oral presentation.

12. **D. Ramaccia**, F. Bilotti, and A. Toscano, "Design formulas of high-impedance surfaces with circular patch arrays", Proc. of *META 2010: Fifth Italian Workshop on Metamaterials and Special Materials for Electromagnetic Applications and TLC*, Rome, IT, December 13-15, 2010 – Regular oral presentation.

13. **D. Ramaccia**, F. Bilotti, and A. Toscano - "Parametric bandwidth analysis of an artificial magnetic conductor surface", Proc. of *Fem 2010: IV Italian Workshop "The Finite Element Method Applied to Electrical and Information Engineering"*, Rome, IT, December 13-15, 2010 – Regular oral presentation.

14. **D. Ramaccia**, F. Bilotti, A. Toscano, A. Massaro, and R. Cingolani, "Electrical and radiation properties of a horn nano-antenna at near infrared frequencies", Proc. of *2011 IEEE Antennas Propag. Symposium,* Spokane , WA, USA, July 03-08, 2011 – Regular oral presentation.

15. **D. Ramaccia**, F. Bilotti, and A. Toscano, "Horn nano-antenna at near-infrared frequencies: design and potential applications", Proc. of *Metamaterials' 2011: 5th International Congress on Advanced EM Materials in MW and Optics,* Barcelona, ES, October 09-15, 2011 – Poster presentation (Winner IET price).

16. F. Bilotti, L. Di Palma, D. Ates, **D. Ramaccia**, A. Toscano, and E. Ozbay, "Enhanced microwave transmission at microwave frequencies: new setups and applications", Proc. of *MediNano4 – 4th Mediterranean Conference on Nano-Photonics,* Rome, IT, October 24-25, 2011 – Invited oral presentation.

17. **D. Ramaccia**, F. Bilotti, and A. Toscano, "Boosting PV cell performances by using horn nano–concentrators", Proc. of. *2012 IEEE Antennas Propag. Symposium*, Chicago, IL, USA, July 08-13, 2012 – Poster presentation.

18. F. Bilotti, L. Di Palma, **D. Ramaccia**, and A. Toscano, "Self-Filtering Low-Noise horn antenna", Proc. of. *2012 IEEE Antennas Propag. Symposium*, Chicago, IL, USA, July 08-13, 2012 – Regular oral presentation.

19. **D. Ramaccia**, S. Scanu, V. Piermattei, F. Bilotti, M. Marcelli and A.Toscano - "Aperture Plasmonic Nano-antennas in Solar Energy Harvesting", Proc. of *OWEMES 2012,* Rome, IT, September 05-07, 2012 – Regular oral presentation.

20. M. Barbuto, A. Monti, **D. Ramaccia**, F. Bilotti, A. Toscano, and L. Vegni, "Metamaterial activities at microwave and optical frequencies at "RomaTre", Proc. of *RiNEm 2012, XIX Riunione Nazionale del'Elettromagnetismo*, Roma, IT, September 10-14, 2012 – Poster presentation.

21. **D. Ramaccia**, F. Scattone, F. Bilotti, and A. Toscano, "Design of a Broadband Shortened Horn Loaded with a Flat Wire-Medium Annular Lens" Proc. of *Metamaterials' 2012: 6th International Congress on Advanced EM Materials in MW and Optics,* St. Petersburg, RU, September 16-21, 2012 – Regular oral presentation.

22. F. Bilotti, L. Di Palma, **D. Ramaccia**, and A. Toscano, "Efficient electrically small apertures and their applications in microwave components", Proc. of *Metamaterials' 2012: 6th International Congress on Advanced EM Materials in MW and Optics,* St. Petersburg, RU, September 16-21, 2012 – Regular oral presentation.

23. F. Bilotti, L. Di Palma, **D. Ramaccia**, A. Toscano, L. Vegni, D. Ates and E. Ozbay, "Extracting Power from Sub-Wavelength Apertures by Using Electrically Small Resonators: Phenomenology, Modeling, and Applications", Proc. of *2012LAPC – Loughborough Antennas & Propagation Conference,* Loughborough, UK, November 12-13, 2012 – Regular oral presentation.

Autor

April 23, 1985	Born, Rome, Italy
October 09, 2007	B.S. Electronic Engineering
October 15, 2009	M.S. Electronic Engineering
May, 2011	Engineering licence
January 2010 – December 2012	PhD Student in Applied Electomagnetics
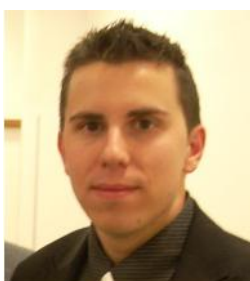
Davide Ramaccia (S'11) was born in Rome, Italy, on April 23, 1985. He received both his BS (summa cum laude) and MS (summa cum laude) in electronic and ICT engineering both from Roma Tre University, in 2007 and 2009 respectively. In 2009, during his Master Thesis, he collaborate with Space Engineering S.p.A. on the design and realization of a dichroic mirror for satellite antennas. He started his PhD research programme at the Department of Applied Electronics at "RomaTre" University under supervision of Prof. Alessandro Toscano. His PhD project aims at design and realization of novel components loaded with metamaterials, thereby developing new analytical models for metamaterials and metasurfaces and deriving effective design formulas. Since 2012, he is with the Department of Engineering, "Roma Tre" University. His main research interests are in the microwave and optical components loaded with complex media, metamaterials and metasurfaces. He has been member of the local committee of the Fifth Italian Workshop on Metamaterials and Special Materials, Meta 2010 (Rome, Italy, December 2010) and he served as secretary member of the fourth Italian Workshop on Finite Element Methods applied to Electrical and Information Engineering, FEM 2010 (Rome, Italy, December 2010).

Dr. Ramaccia is currently member of the Italian Society on Electromagnetics, SIEM, and of the National Inter-University Consortium for Telecommunications, CNIT. Dr. Ramaccia has been the recipient of the IET Award for the Best Poster on the Metamaterial Application in Antenna Field in 2011.